(Sub)Millimetre Observing Techniques

A Student Summer School
14 – 17 August 2006
Victoria,BC

Fourier Transform Spectroscopy

JCMT FTS-2

David A Naylor
University of Lethbridge
Naylor@uleth.ca
http://www.uleth.ca/phy/naylor
1-403-329-2426

Reading material:

Appendix A – Chapter 2 and bibliography from J.V. Lindner's M.Sc. thesis

Appendix B – Chapters 2 and 3 and bibliography from L.D. Spencer's M.Sc. thesis

Appendix C – Naylor, D.A., Gom, B.G., Zhang, B. Preliminary design of FTS-2: an imaging Fourier transform spectrometer for SCUBA-2. *Proc. SPIE, Astronomical Telescopes and Instrumentation* **6275**, Orlando, Florida, May 2006.

Appendix D – suggested readings

Appendix A

SHIFTS: SIMULATOR FOR THE HERSCHEL IMAGING FOURIER TRANSFORM SPECTROMETER

John Vyvyan Lindner

Bachelor of Science, Physics and Astronomy, University of Victoria (2003)

A thesis submitted to the School
of Graduate Studies of the University
of Lethbridge in partial fulfilment
of the requirements of the degree

MASTER OF SCIENCE

Department of Physics
University of Lethbridge
Lethbridge, Alberta, Canada

Chapter 2

Fourier Transform Spectroscopy

"A little over a year ago the scientific world was startled by the announcement that Professor Zeeman had discovered a new effect of magnetism on light. (...) It occurred to me at once to try this experiment by the interference method, which is particularly adapted to the examination of just such cases as this, in which the effect to be observed is beyond the range of the spectroscopic method. (...) The visibility curves that were thus obtained showed that, instead of a broadening, as was first announced by Zeeman, each of the sodium lines appeared to be double."

- Albert A. Michelson, *Light Waves and their Uses*, University of Chicago Press (1902).

This chapter outlines the theoretical background of Fourier transform spectroscopy (FTS). A thorough grounding in FTS is key to understanding the operation of the Spectral and Photometric Imaging Receiver (SPIRE; see Chapter 3) spectrometer onboard the Herschel Space Observatory (HSO) and the Simulator for the Herschel Imaging Fourier Transform Spectrometer (SHIFTS; see Chapter 4). The concepts introduced in this chapter reappear throughout this thesis.

Section 2.1 introduces the Fourier series and the Fourier transform; Section 2.2 outlines the basic properties of Fourier transforms. With the mathematical foundation in place, the Michelson interferometer and its contributions to spectroscopy are described in Section 2.3. From the ideal case, Sections 2.4 and 2.5 discuss the techniques used today in Fourier transform spectroscopy.

2.1 The Fourier series and transform

In 1807, J. B. Joseph Fourier submitted "Sur la propagation de la Chaleur dans les corps solides"* to L'Institut de France [48]. To describe heat flow, Fourier proposed that the initial temperature distribution, $f(x)$, of a one-dimensional solid is represented as a infinite sum of sine and cosine terms,

$$f(x) = \sum_{n=0}^{\infty} \left[a_n \cos(nkx) + b_n \sin(nkx) \right], \tag{2.1}$$

where a_n and b_n are the *Fourier coefficients*, x is the position (in units of length) and $k = \frac{2\pi}{\lambda}$ is the angular wavenumber (in radians per unit length) for a wavelength of $\lambda = 2L$ [48, 49]. As derived in Champeney [50], the Fourier coefficients for $f(x)$, periodic over the interval $[-L, L]$, are given by

$$a_n = \frac{1}{L} \int_{-L}^{L} f(x) \cos(nkx) dx, \tag{2.2}$$

$$b_n = \frac{1}{L} \int_{-L}^{L} f(x) \sin(nkx) dx. \tag{2.3}$$

By letting $L \to \infty$ and replacing k with $2\pi\sigma$ where σ is the spatial frequency or *wavenumber* (in waves per unit length), the discrete Fourier coefficients, a_n and b_n, are replaced with a continuum of coefficients denoted, respectively, by $a(\sigma)$ and $b(\sigma)$. This allows Equation 2.1 to be rewritten as two integrals,

$$f_c(x) = \int_{-\infty}^{\infty} a(\sigma) \cos(2\pi\sigma x) d\sigma, \tag{2.4}$$

$$f_s(x) = \int_{-\infty}^{\infty} b(\sigma) \sin(2\pi\sigma x) d\sigma, \tag{2.5}$$

where $f_c(x)$ is the *inverse Fourier cosine transform* of $a(\sigma)$, and $f_s(x)$ is the *inverse Fourier sine transform* of $b(\sigma)$ [51]. Note that $a(\sigma)$ contains only even terms and $b(\sigma)$ only odd terms. Employing Euler's formula, $a(\sigma)$ and $b(\sigma)$ are written as a complex function, $F(\sigma)$, composed of both even and odd terms and given by

$$F(\sigma) = a(\sigma) - ib(\sigma), \tag{2.6}$$

where $i = \sqrt{-1}$ [51, 52]. Therefore, Equations 2.4 and 2.5 are generalized as a single equation,

$$f(x) = \mathcal{F}^{-1}[F(\sigma)] = \int_{-\infty}^{\infty} F(\sigma) e^{i2\pi\sigma x} d\sigma, \tag{2.7}$$

*On the propagation of heat in solid bodies

where $\mathcal{F}^{-1}[F(\sigma)]$ is defined as the *inverse Fourier transform* (or reverse Fourier transform) of $F(\sigma)$ [50, 51, 53]. To determine $F(\sigma)$, we perform the (forward) *Fourier transform*,

$$F(\sigma) = \mathcal{F}[f(x)] = \int_{-\infty}^{\infty} f(x)e^{-i2\pi\sigma x}dx, \tag{2.8}$$

where x and σ are called conjugate variables. Equations 2.7 and 2.8 are one of three definitions of the forward and reverse Fourier transform seen in Bracewell [51] and Champeney [50]. While the above definition employs reciprocal units in the spatial and spectral domains, the other two definitions are instead defined in terms of position and angular wavenumber. To normalize the transform, these definitions include a constant before the integral sign; one multiplies the reverse transform by $\frac{1}{2\pi}$ while the other multiplies both the forward and reverse transforms by $\frac{1}{\sqrt{2\pi}}$. To avoid confusion, the definitions of the forward and reverse Fourier transforms given in Equations 2.7 and 2.8 are used exclusively in this thesis.

As can be seen, the Fourier integrals are reversible operations: given $F(\sigma)$, we can determine $f(x)$; and vice-versa [50]. The Fourier transform provides a simple relationship between a function and its frequency components. Waveforms can be manipulated or analyzed in either the spatial or spectral domains (i.e., as a function of x or σ, respectively).

2.2 Properties of Fourier transforms

This section outlines some important properties of Fourier transforms. The field of study devoted to the representation of an arbitrary function by a superposition of sinusoids and cosinusoids is called *Fourier analysis* [49]. Specific topics covered include symmetry and phase, the boxcar and triangle functions, the superposition and convolution theorems, and Parseval's theorem.

The previous section used position, x, and wavenumber, σ, as conjugate variables in the two domains [54]. For reasons which become clear in Section 2.3.2, the most frequently employed conjugate pair in Fourier transform spectroscopy is x in centimetres (cm) and σ in inverse centimetres (cm^{-1}) [49, 55–57]. Another conjugate pair employed in this thesis (see Sections 4.4 and 4.5, and Appendix B) is time (in seconds, or s) and frequency (in Hz), denoted respectively by t and f. However, for the remainder of this chapter, wavenumber and frequency are used interchangeably.

2.2.1 Symmetry

Consider an even function of unit amplitude defined over the range $x = [-\infty, \infty]$ of the form

$$f_e(x) = \cos(2\pi\sigma_o x), \tag{2.9}$$

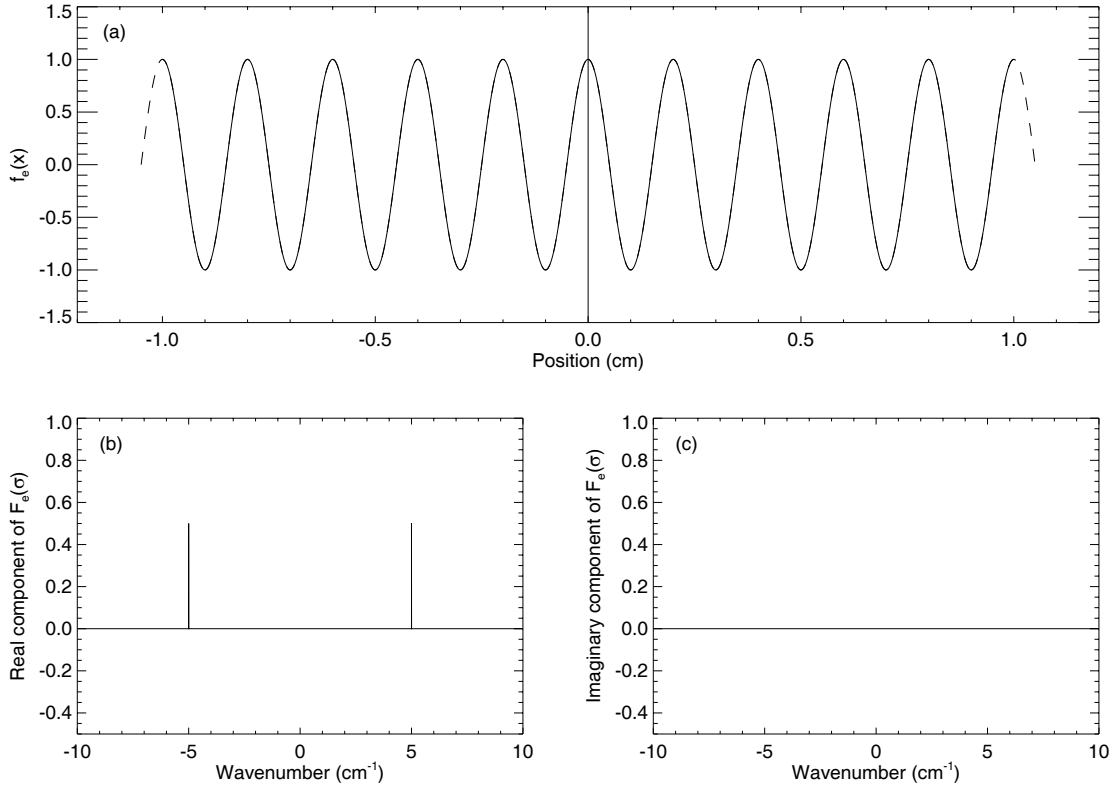

Figure 2.1: Fourier transform of a symmetric function. Panel (a) shows an infinite even function with a frequency of 5 cm^{-1}. Panels (b) and (c) show the real and imaginary components, respectively, of the Fourier transform of Panel (a).

where $\sigma_o = 5$ cm^{-1} is the spatial frequency, as shown in Figure 2.1(a). Following the derivation in Bracewell [51], the Fourier transform of $f_e(x)$ is

$$F_e(\sigma) = \mathcal{F}[f_e(x)] = \frac{1}{2}\delta(\sigma \mp \sigma_o), \tag{2.10}$$

where

$$\delta(\sigma - \sigma_o) = \begin{cases} 1 & \text{for } \sigma = \sigma_o \\ 0 & \text{for } \sigma \neq \sigma_o \end{cases}, \tag{2.11}$$

is the Dirac Delta function or simply the *delta function* [49, 51, 58]. As can be seen in Panels (b) and (c) of Figure 2.1, $F_e(\sigma)$ corresponds to two real symmetric delta functions at $\sigma = \pm 5$ cm^{-1}. In fact, the Fourier transform of any symmetric function is symmetric [51].

As shown in Equations 2.7 and 2.8, the limits of the Fourier integrals are symmetric about $x = 0$ cm. Therefore, the Fourier transform of any function produces information at both positive and negative frequencies. Due to the inherent symmetry of the Fourier transform, the unit amplitude of $f_e(x)$ in the spatial domain is split evenly between the

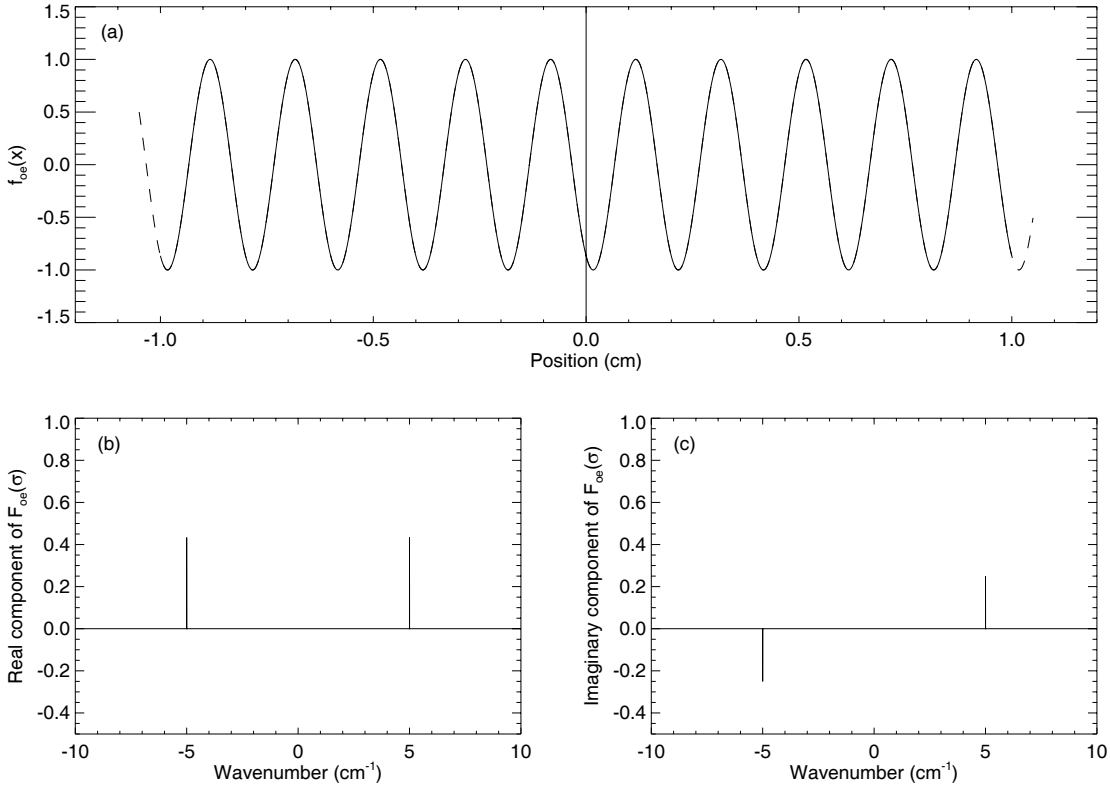

Figure 2.2: Fourier transform of an asymmetric function. Panel (a) shows an infinite function composed of even and odd terms. Panels (b) and (c) show the real and imaginary components, respectively, of the Fourier transform of Panel (a).

two delta functions in the spectral domain. However, in practice, negative frequencies are non-physical and are generally ignored [49].

Conversely, consider an odd function defined over the range $x = [-\infty, \infty]$ of the form

$$f_o(x) = \sin(2\pi\sigma_o x). \tag{2.12}$$

In this case, the Fourier transform of $f_o(x)$ is

$$F_o(\sigma) = \mathcal{F}[f_o(x)] = \pm\frac{1}{2}i\delta(\sigma \mp \sigma_o) = \begin{cases} \frac{1}{2}i & \text{for } \sigma = \sigma_o \\ -\frac{1}{2}i & \text{for } \sigma = -\sigma_o \\ 0 & \text{for } \sigma \neq \pm\sigma_o \end{cases}. \tag{2.13}$$

Contrary to $\mathcal{F}[f_e(x)]$, the Fourier transform of a real and anti-symmetric function is imaginary and anti-symmetric [51]. However, similar to $\mathcal{F}[f_e(x)]$, the unit amplitude of $f_o(x)$ is split evenly between the two delta functions at frequencies of $\sigma = \pm\sigma_o$ in $F_o(\sigma)$.

In the more general case, an arbitrary function is asymmetric. By Fourier decomposition, an asymmetric real function is represented as a sum of even and odd terms [49].

Therefore, its Fourier transform contains a real even component and an imaginary odd component [51]. For example, consider the following real function:

$$f_{oe}(x) = \cos\left(2\pi\sigma_o x + \frac{5\pi}{6}\right). \tag{2.14}$$

As can be seen in Panel (a) of Figure 2.2, this function is asymmetric about $x = 0$ cm. The resultant Fourier transform, shown in Panels (b) and (c), is a combination of the previous two cases: the even component of the waveform corresponds to symmetric delta functions in the real part of the spectrum, and the odd component corresponds to anti-symmetric delta functions in the imaginary part of the spectrum.

Given Figure 2.2, the real and imaginary components can be written in terms of the *magnitude* and *phase* (denoted respectively by $\mathcal{M}$ and ϕ) [52]. On the complex unit circle, this corresponds to converting from cartesian to polar coordinates. The relationship between the real, $\mathcal{R}_\sigma$, and imaginary, $\mathcal{I}_\sigma$, components of a spectrum is given by

$$\mathcal{M}_\sigma = \sqrt{\mathcal{R}_\sigma^2 + \mathcal{I}_\sigma^2}, \tag{2.15}$$

and

$$\phi_\sigma = \arctan\left(\frac{\mathcal{I}_\sigma}{\mathcal{R}_\sigma}\right). \qquad \text{[radians]} \tag{2.16}$$

As can be seen in Panels (b) and (c) of Figure 2.2, the amplitude of the real and imaginary components at $\sigma = 5$ cm^{-1} are $\frac{\sqrt{3}}{4}$ and $\frac{1}{4}$, respectively. Equation 2.16 yields $\phi = \frac{5\pi}{6}$, identical to the phase term in Equation 2.14 that introduced the asymmetry. Using a technique called *phase correction*, the phase is used to retrieve a real spectrum from an asymmetric waveform (see Section 2.5.3) [59].

The symmetry properties of Fourier transforms are summarized in Table 2.1 [51, 56]. These properties suggest operations on even and real functions are preferable since their Fourier transforms only require a cosine transform [51]. Fourier transform spectrometers such as the Michelson interferometer (see Section 2.3) exploit this fact because their measurements are inherently real and, for the ideal case, symmetric [55, 56].

2.2.2 Transform pairs

In addition to the sine and cosine, there are other functions whose Fourier transforms are frequently encountered in Fourier analysis [49, 51, 54]. This section lists two common functions seen throughout this chapter. The first is the boxcar function, defined by

$$\Pi(x) = \begin{cases} 1 & \text{for } |x| < L \\ 0 & \text{for } |x| > L \end{cases}, \tag{2.17}$$

Table 2.1: Symmetry properties of Fourier transform pairs, where $f(x)$ is any function, and $\mathcal{F}[f(x)]$ is the Fourier transform of $f(x)$.

$f(x)$		$\mathcal{F}[f(x)]$	
Real	Imaginary	Real	Imaginary
even	0	even	0
odd	0	0	odd
0	even	0	even
0	odd	odd	0
asymmetric	0	even	odd
0	asymmetric	odd	even
even	odd	asymmetric	0
odd	even	0	asymmetric
even	even	even	even
odd	odd	odd	odd

and shown in Panel (a) of Figure 2.3. As shown in Bracewell [51] and James [54], the Fourier transform of $\Pi(x)$ is

$$\mathcal{F}[\Pi(x)] = \int_{-\infty}^{\infty} \Pi(x) e^{-i2\pi\sigma x} dx = 2L \frac{\sin(2\pi\sigma L)}{2\pi\sigma L}, \tag{2.18}$$

where $\frac{\sin(2\pi\sigma L)}{2\pi\sigma L}$ is commonly referred to as the *sinc function*, $\mathrm{sinc}(2\pi\sigma L)$, shown in Panel (b). Since the sinc function is frequently encountered in Fourier analysis, its properties are well understood [51, 54]. The sinc function has a full-width at half-maximum (FWHM) of $\frac{1.207}{2L}$ and crosses zero where σ is an integer multiple of $\frac{1}{2L}$. Located at $\frac{1.43}{2L}$, the secondary minimum is -21.7 % of the central maximum [51, 56].

The second common function is the triangle function, defined by

$$\Lambda(x) = \begin{cases} 1 - \frac{|x|}{2L} & \text{for } |x| < 2L \\ 0 & \text{for } |x| > 2L \end{cases}, \tag{2.19}$$

and shown in Panel (c) of Figure 2.3. Shown in Panel (d), the Fourier transform of $\Lambda(x)$ is

$$\mathcal{F}[\Lambda(x)] = \int_{-\infty}^{\infty} \Lambda(x) e^{-i2\pi\sigma x} dx = 4L^2 \mathrm{sinc}^2(2\pi\sigma L). \tag{2.20}$$

The properties of $\mathrm{sinc}^2(2\pi\sigma L)$ are similar to the sinc function. However, since $\mathrm{sinc}^2(2\pi\sigma L)$ is positive-definite for all σ, it is the secondary maximum that occurs at $\frac{1.43}{2L}$. Moreover, the amplitudes of all the secondary lobes are reduced; the amplitude of the secondary maximum is only 4.7 % of the central maximum [51, 56].

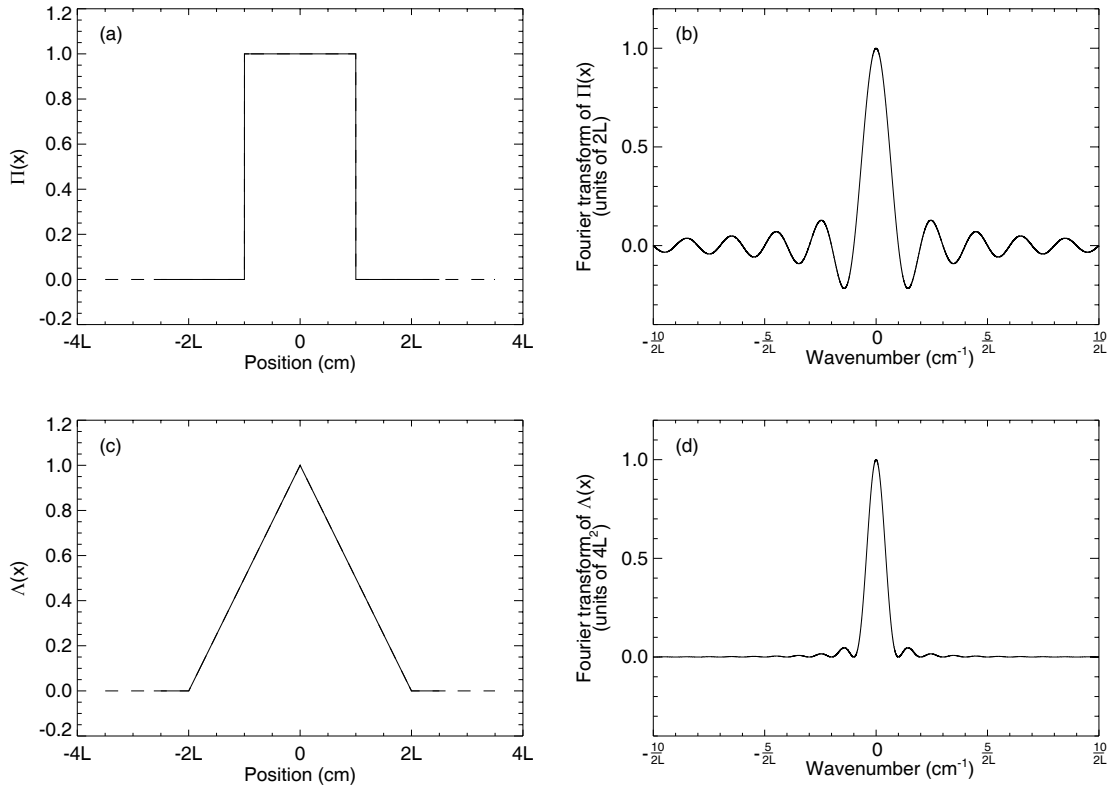

Figure 2.3: Fourier transforms of the boxcar and triangle functions. Panel (a) shows a boxcar function with its Fourier transform, a sinc function, shown in Panel (b). Panel (c) shows a triangle function with its Fourier transform, a sinc^2 function, shown in Panel (d).

2.2.3 Fourier theorems

There are a series of theorems fundamental to Fourier analysis that describe the effect that changes to a function have on its Fourier transform. This section outlines three important theorems employed in this thesis: *superposition*, *convolution* and *Parseval*. (For additional theorems, the reader is referred to Bracewell [51], Brigham [53], Champeney [50] and James [54].) For the remainder of this chapter, $F(\sigma)$ and $G(\sigma)$ are the Fourier transforms of $f(x)$ and $g(x)$, respectively, and only positive frequencies are shown in a spectrum.

Superposition theorem

Fourier transforms obey the superposition theorem [49, 51], which is expressed mathematically as

$$\mathcal{F}[f(x) + g(x)] = \mathcal{F}[f(x)] + \mathcal{F}[g(x)] = F(\sigma) + G(\sigma). \tag{2.21}$$

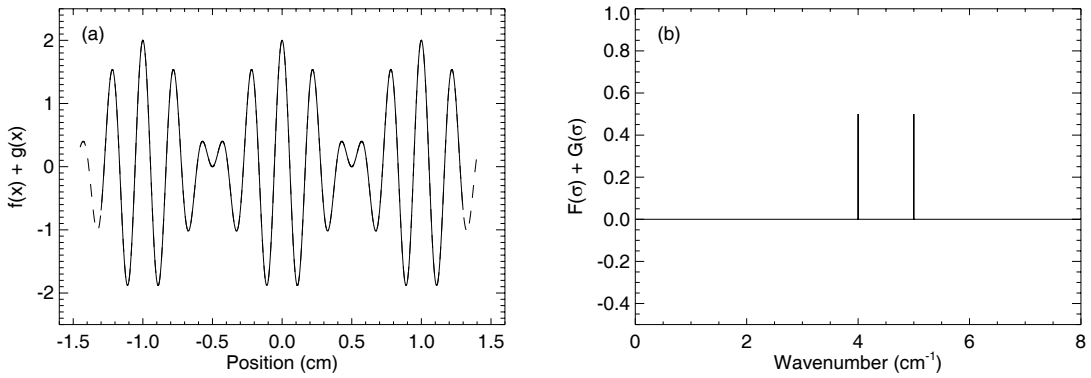

Figure 2.4: Example of the superposition theorem. Panel (a) is the sum of two infinite cosine functions oscillating at 4 and 5 cm^{-1}. Panel (b) is the Fourier transform of Panel (a).

Consider two cosine functions (see Equation 2.9) oscillating at spatial frequencies of σ_1 and σ_2. By employing trigonometric identities, the resultant function of the sum of these two waveforms produces a *beat pattern* given by

$$f_{\sigma_1}(x) + f_{\sigma_2}(x) = 2\cos(\pi x(\sigma_1 - \sigma_2))\cos(\pi x(\sigma_1 + \sigma_2)), \tag{2.22}$$

where the first cosine term is the envelope of the rapidly varying second cosine term. Panel (a) of Figure 2.4 shows the above equation with $\sigma_1 = 5$ cm^{-1} and $\sigma_2 = 4$ cm^{-1}. In agreement with the above equation, the waveform oscillates nine times in a 2 cm spatial period. Panel (b) shows the Fourier transform of Equation 2.22. As can be seen, the Fourier transform of the sum of the two functions is simply the Fourier transform of each of the individual functions.

Convolution theorem

The Fourier transform of the multiplication of two functions in one domain is equivalent to convolution in the other, as given by

$$\mathcal{F}^{-1}(G(\sigma) \cdot F(\sigma)) = f(x) * g(x) = \int_{-\infty}^{\infty} f(z)g(x - z)dz, \tag{2.23}$$

where z is a dummy variable and $f(x)*g(x)$ denotes the convolution of $f(x)$ and $g(x)$ [49,51]. In effect, convolution shifts the reverse of the second function across the first function; each point in x is the integral of the product of the overlapping regions of $f(z)$ and $g(x-z)$ [51].

Consider the convolution of two boxcar functions, where the reversed function is given by Equation 2.17 and the fixed boxcar funtion, $f(x)$, is twice as wide as $g(x - z)$. As shown in the upper portion of Figure 2.5, the initial overlap occurs at $x = -3L$. The integrated area increases linearly to a plateau that begins at $x = -L$. The overlap is constant until $x = L$ and then decreases linearly to zero [49, 56, 58].

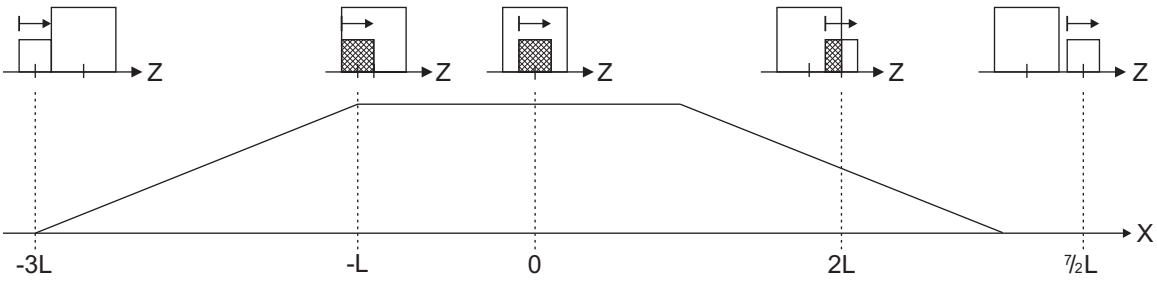

Figure 2.5: Example of the convolution theorem. The lower portion shows a trapezoid, the result of the convolution of two boxcar functions of different widths. The integration over z at each point in x (see Equation 2.23) is shown in the upper portion, where the hatched regions indicates the overlapping area of the two boxcars and the arrows indicate the direction of the shifting boxcar function.

As is clear from the lower portion of Figure 2.5, the convolution of two boxcar functions of different widths is a trapezoid. In the special case where the boxcar functions have the same width L, the convolution yields a triangle function. As indicated in the previous section, the Fourier transform of a boxcar function is a sinc function. The product of two sinc functions naturally yields a sinc^2 function, identical to the Fourier transform of a triangle function [51]. (Several excellent animations of convolution can be found at *http://mathworld.wolfram.com/Convolution.html*.)

Parseval's theorem

The final theorem of interest is Parseval's theorem, which states that the integral of the square of a function equals the integral of the square of its Fourier transform [51, 53]. It is expressed mathematically as

$$\int_{-\infty}^{\infty} |f(x)|^2 dx = \int_{-\infty}^{\infty} |F(\sigma)|^2 d\sigma. \tag{2.24}$$

Parseval's theorem is the embodiment of the conservation of energy; information is neither created nor destroyed during a transform. For a derivation of Parseval's theorem, the reader is referred to Champeney [50].

2.3 The Michelson interferometer

As Section 2.2 indicated, the Fourier transform is a powerful mathematical tool that relates any periodic waveform to its component frequencies. This section describes how Fourier transforms are employed to determine the spectral distribution of electromagnetic radiation.

2.3.1 Michelson and the interference of light

Light is composed of transverse waves of electric and magnetic potentials [60]. In 1801, Thomas Young conducted his famous double-slit experiment, proving that light waves interfere with one another [61]. Put simply, the theory of interference states that the superposition of two rays of light of equal amplitude, frequency and phase is simply another waveform of identical frequency and phase but with double the amplitude. This is called constructive interference. However, if those same two rays of light are out of phase by π radians, then when added together they cancel one another out. This is called destructive interference [62].

The concept of interference was firmly established when Albert A. Michelson began his studies of light in 1878 [63]. In 1881, Michelson invented his now famous interferometer to test for the existence of the luminiferous ether [63, 64]. Although the ether experiment returned a negative result (which had a major impact on relativity), the Michelson interferometer has since played a major role in the development of spectroscopy [57, 65].

The Michelson interferometer is one example of a *Fourier transform spectrometer*, a two-beam interferometer used to measure spectra [60,65]. The SPIRE imaging spectrometer is based on another two-beam interferometer, the *Mach-Zehnder* (MZ) interferometer (see Chapter 3) [5, 60]. However, the Michelson interferometer is the simplest design so our discussion focuses on it.

2.3.2 Theory of an ideal Michelson interferometer

Figure 2.6 depicts a schematic of a Michelson interferometer. Light emitted from the source is collimated and then strikes the *beamsplitter*, a reflective substrate angled 45 degrees with respect to the direction of travel of the light [64, 65]. Half of the beam is reflected off the beamsplitter and half is transmitted. The reflected beam is reflected again off a fixed plane mirror back to the beamsplitter. The transmitted beam is reflected off a second plane mirror, which moves in a direction perpendicular to its plane, back to the beamsplitter.

The two beams recombine at the beamsplitter and the reflected light is directed down to an eyepiece, where Michelson observed the resultant intensity. By changing the position of the movable mirror with turns of a millimetre screw, Michelson changed the optical distance the second beam travelled [65]. Note than only half of the radiation entering a Michelson interferometer can be measured since 50 % is transmitted back through the beamsplitter to the source [55, 66].

To understand the effect of moving the second mirror, let us examine the optical path of the two beams of light within the interferometer. From the solution to Maxwell's

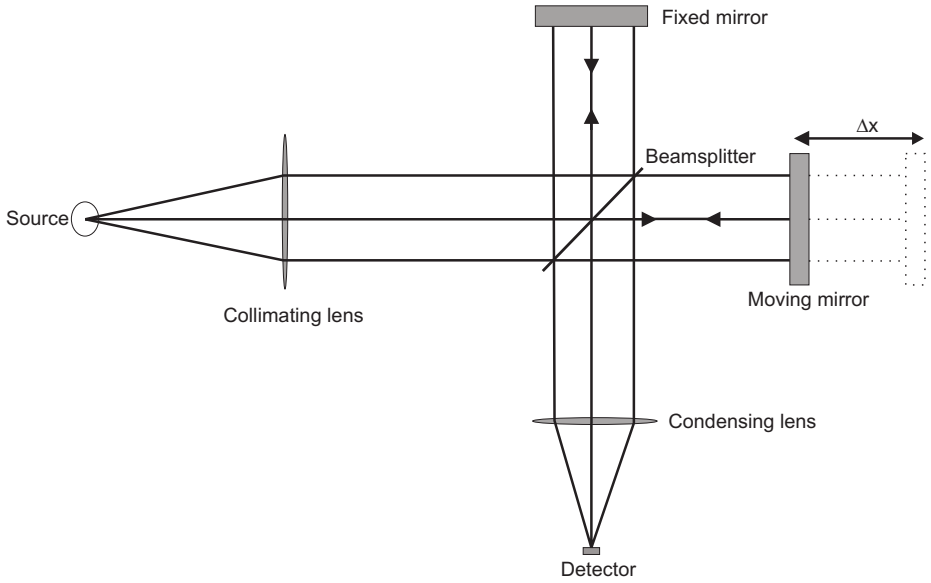

Figure 2.6: Schematic of a Michelson interferometer. Arrows indicate the direction of motion of light rays. The dotted section of the moving mirror corresponds to a movement of Δx in the position of the mirror.

equations for one-dimensional free space, the wave equation of the electric field is given by

$$E(x,\sigma) = E_o(\sigma)e^{i2\pi(\sigma x - \nu t)}, \qquad [\mathrm{V\,m^{-1}}] \tag{2.25}$$

where x is the position (in cm), σ is the wavenumber (in $\mathrm{cm^{-1}}$), t is the time (in s), ν is the frequency (in Hz) and $E_o(\sigma)$ is the maximum amplitude of the electric field (in volts per metre, or $\mathrm{V\,m^{-1}}$) [60].

Following a reflection from and a transmission through the beamsplitter, the two beams are observed at the eyepiece, having travelled optical paths x_1 and x_2. The resultant electric field at the detector is

$$E_d(x,\sigma) = rtE_o(\sigma)\left[e^{-i2\pi(\sigma x_1 - \nu t)} + e^{-i2\pi(\sigma x_2 - \nu t)}\right], \qquad [\mathrm{V\,m^{-1}}] \tag{2.26}$$

where r and t are the *amplitude coefficients* of reflection and transmission, respectively, of the beamsplitter [67]. The intensity, $I_d(x,\sigma)$, measured at the eyepiece is proportional to the time average of the square of the measured electric field,

$$I_d(x,\sigma) = \frac{c\epsilon_o}{2}E_d(x,\sigma)E_d^*(x,\sigma), \qquad [\mathrm{W}] \tag{2.27}$$

where c is the speed of light and ϵ_o is the permittivity of free space (see Table A-1) [67]. For the remainder of this chapter, the constant factor $\frac{c\epsilon_o}{2}$ is ignored and the intensity measured at the eyepiece is simply given by

$$I_d(x,\sigma) \propto E_d(x,\sigma)E_d^*(x,\sigma) = 2RTE_o^2(\sigma)\left[1+\cos(2\pi x\sigma)\right], \qquad [\mathrm{W}] \tag{2.28}$$

where $R = r^2$ is the *reflectance*, $T = 1 - r^2$ is the *transmittance* and $x = x_1 - x_2$ is the *optical path difference* (OPD) between the two beams (in cm), which depends solely on the position of the movable mirror [49, 60]. Since x is an observable quantity, it is natural to use wavenumber (in cm^{-1}) as the conjugate variable in the spectral domain.

The unique position corresponding to $x = 0$ cm is called *zero path difference* (ZPD) because both mirrors are equidistant from the beamsplitter [55]. At ZPD, both beams of light travel the same distance so all frequencies are in phase and yield the maximum intensity [49].

As the second mirror moves away from ZPD, the optical path distance for the second beam of light increases. Since the light travels between the movable mirror and the beamsplitter twice, a change of Δx in the moving mirror's position results in a change of $2\Delta x$ in the optical path (see Figure 2.6) [49, 55, 56]. The power, $I(x)$, at the eyepiece is the integral of all the component intensities:

$$\begin{aligned} I(x) &= \int_0^\infty I_d(x,\sigma)d\sigma, \\ &\propto 2RT\left[\int_0^\infty E_o^2(\sigma)d\sigma + \int_0^\infty E_o^2(\sigma)\cos(2\pi\sigma x)d\sigma\right], \\ &= \frac{1}{2}I(0) + 2RT\int_0^\infty B(\sigma)\cos(2\pi\sigma x)d\sigma, \qquad [\text{W}] \end{aligned} \tag{2.29}$$

where $E_o^2(\sigma)$ is proportional to our measure of interest, the spectrum $B(\sigma)$ [60]. For an ideal interferometer, $R = T = 0.5$. Therefore, it can be seen by inspection that half the maximum power is contained in the constant term above [49]. It is customary to ignore the offset since it contains no spectral information. Instead, we focus on the modulating term, rewritting Equation 2.29 as

$$I(x) = \int_0^\infty B(\sigma)\cos(2\pi\sigma x)d\sigma. \qquad [\text{W}] \tag{2.30}$$

Changes in the optical path difference introduce phase shifts of $\cos(2\pi\sigma x)$ into the second beam. At a given OPD, higher frequency components experience greater phase shifts [56]. Mirroring the spectrum to include negative frequencies, using the definition $B(\sigma) = B(-\sigma)$, yields

$$I(x) = \frac{1}{2}\int_{-\infty}^\infty B(\sigma)\cos(2\pi\sigma x)d\sigma, \qquad [\text{W}] \tag{2.31}$$

which is the inverse Fourier cosine transform of $B(\sigma)$ (see Equation 2.4) [55].

The function $I(x)$ is a measure of the interference of all the frequency components of $B(\sigma)$ as the OPD is varied. Therefore, $I(x)$ is termed an *interferogram* [49]. By the symmetry requirements of Fourier transforms (see Section 2.2.1), the measured interferogram is *double-sided*; i.e., it is evenly sampled at both positive and negative optical path differences [49, 56]. The spectrum, $B(\sigma)$, is recovered by performing the Fourier cosine transform

on the interferogram,

$$B(\sigma) = \int_{-\infty}^{\infty} I(x)\cos(2\pi\sigma x)dx. \qquad [\mathrm{W}] \tag{2.32}$$

2.4 Sampling an interferogram

Since Michelson observed with an eyepiece, he never measured an interferogram, only its visibility curve [57, 65]. Heinrick Rubens and Robert W. Wood measured the first true interferogram in 1911 [68]. However, they were still unable to compute the Fourier transform of their interferogram directly [49,57,68]. Another forty years passed before Peter B. Fellgett published results of the first numerical Fourier transform of an interferogram [57]. The first successful use of a Fourier transform spectrometer in astronomy came in 1966 when Janine and Pierre Connes used one to measure the near-infrared (NIR) spectrum of the atmosphere of Venus [69].

This section focuses on the basic features of an interferogram and how interferograms are measured. The topics discussed include discrete sampling, the Nyquist theorem, aliasing, natural apodization, instrumental line shape and broadband spectra. The recovery of a spectrum from an interferogram is covered in Section 2.5.

2.4.1 Discrete sampling

In practice, it is not possible to sample a continuous interferogram. Instead, interferograms are usually sampled at equal intervals of optical path difference [56]. Mathematically, this is equivalent to multiplying the interferogram by the Shah function given by

$$\mathrm{III}(x) = \sum_{n=-\infty}^{\infty} \delta(x - n\Delta x), \tag{2.33}$$

where Δx is the sampling interval (in cm).

As a consequence of discrete sampling, there is no guarantee that the position of zero path difference is measured [49]. Figure 2.7 illustrates this problem for an infinite cosine wave with a frequency of $\sigma_o = 3$ cm^{-1} sampled at $\Delta x = 0.1$ cm (as denoted by the red circles). As can be seen, the sampled interferogram is asymmetric, such that its Fourier transform cannot be computed using the Fourier cosine transform (see Section 2.5.1).

2.4.2 Nyquist sampling theorem

Discrete sampling also sets limits on the spectral information recoverable from an interferogram [49, 70]. To sample a spectrum without any loss of information, the *Nyquist*

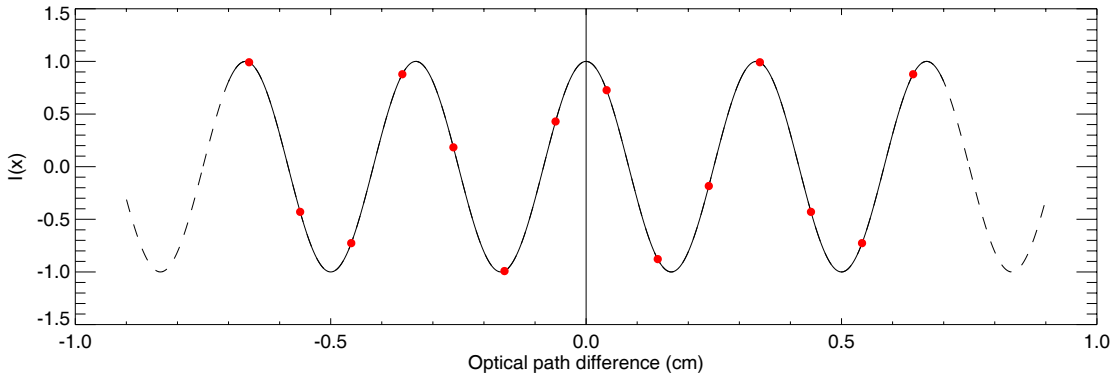

Figure 2.7: Example of a discretely sampled cosine wave. The solid line denotes a infinite cosine wave with a frequency of $\sigma_o = 3$ cm^{-1} sampled every 0.1 cm, where the red circles represent the samples.

criteria states the sampling interval, Δx, must be less than or equal to the inverse of twice the bandwidth of the spectrum:

$$\Delta x \leq \frac{1}{2(\sigma_N - \sigma_L)}, \qquad [\text{cm}] \tag{2.34}$$

where σ_N is the maximum wavenumber and σ_L is the minimum wavenumber of the spectrum (both in cm^{-1}) [49, 56, 70]. The maximum wavenumber, σ_N, is called the *Nyquist frequency* [55]. In practice, the lower bound, σ_L, is taken as a null term and the above equation is simply written as

$$\Delta x \leq \frac{1}{2\sigma_N}. \qquad [\text{cm}] \tag{2.35}$$

2.4.3 Aliasing

If the maximum frequency in the spectrum is not sampled twice per oscillation period (i.e., the Nyquist criteria is not satisfied), the interferogram is aliased. Information beyond the Nyquist frequency is folded into the interferogram at a lower frequency location [55, 56]. Consider a spectrum with a frequency component located at σ_o. The corresponding interferogram is sampled such that $\sigma_o < \sigma_N$. If the spectrum also contains information beyond the Nyquist frequency, spectral features located at $\sigma = 2N\sigma_N \pm \sigma_o$, where N is an integer, are shifted to a frequency of σ_o [56].

Figure 2.8 is a graphical demonstration of this phenomenon. For an interferogram sampled every 0.1 cm (as denoted by the red circles), the corresponding Nyquist frequency is 5 cm^{-1} (see Equation 2.35). The spectrum has two frequency components at 2 and 12 cm^{-1}, represented by the dashed and solid lines, respectively. As can be seen, the amplitudes of the cosine functions are indistinguishable when sampled every 0.1 cm [55].

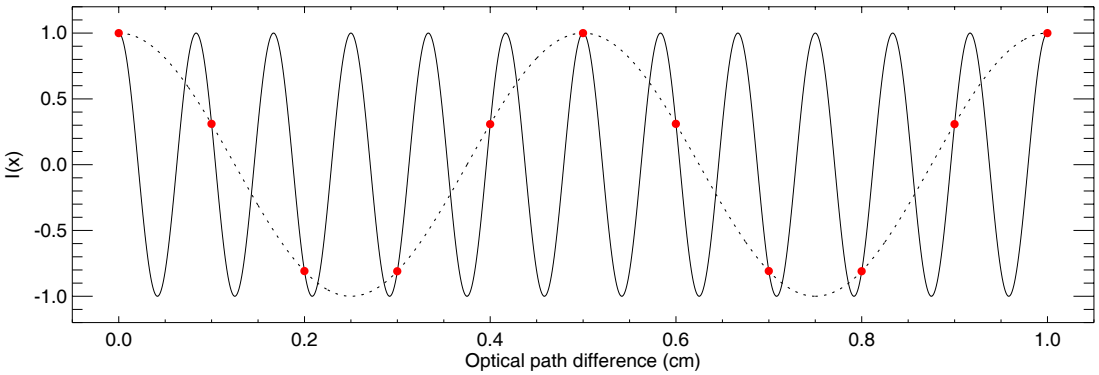

Figure 2.8: Example of aliasing. The solid line corresponds to a cosine function with a frequency of 12 cm^{-1}; the dotted line corresponds to a cosine function with a frequency of 2 cm^{-1}; the red circles represent the 0.1 cm sampling of the waveforms.

2.4.4 Natural apodization

The *finite entrance aperture* of a Fourier transform spectrometer produces an effect termed natural apodization [49]. In an ideal interferometer, an infinitesimal entrance aperture ensures the resultant interference is produced by two plane waves moving in the same direction. However, to increase the light-collecting power, the entrance aperture of a Fourier transform spectrometer has a finite size [49]. From geometric optics, radiation exiting the aperture at different angles travels different optical paths prior to detection [67, 71]. It can be shown that the optical path difference of an off-axis beam is $x\cos(\alpha')$, where α' is the half-cone angle between the off- and on-axis beams (in radians) [66]. To determine the interference fringe intensity at a given OPD, we integrate over the beam size,

$$I(x) = \int_0^{\Omega} \cos[2\pi\sigma x\cos(\alpha')]d\Omega', \qquad [\mathrm{W}] \tag{2.36}$$

where $d\Omega'$ is an element of solid angle (in steradians, or sr) and Ω is the solid angle of the beam, defined as

$$\Omega = \pi\alpha^2, \qquad [\mathrm{sr}] \tag{2.37}$$

where α is the maximum value of α'. Using the small angle identity ($\cos(\alpha) \sim 1 - \frac{\alpha^2}{2}$ for small α) and the above equation, Equation 2.36 yields

$$I(x) = \Omega\mathrm{sinc}\left(\frac{\sigma x\Omega}{2\pi}\right)\cos\left(2\pi\sigma x\left[1 - \frac{\Omega}{4\pi}\right]\right), \qquad [\mathrm{W}] \tag{2.38}$$

as shown in Davis, Abrams & Brault [49].

Two consequences are evident from the above equation. First, the optical path difference grid is shorter for off-axis beams [55]. However, the scale change is generally small and can be ignored (see Section 3.6.2) [49]. The second effect is the modulation of

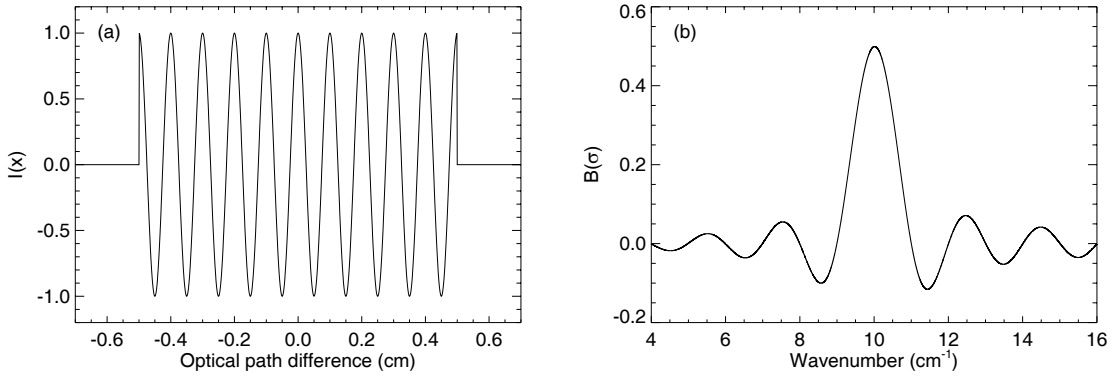

Figure 2.9: Example of finite path difference. Panel (a) shows a cosine waveform with a frequency of 10 cm^{-1} measured over a finite optical path difference from -0.5 to 0.5 cm. Panel (b) is the Fourier transform of the waveform, a sinc function centered at 10 cm^{-1}.

the interferogram by a sinc function. From Sections 2.2.2 and 2.2.3, this is equivalent to the convolution of spectral features by a boxcar function of width $\frac{\Omega\sigma}{2\pi}$. If the aperture of the interferometer is increased such that the width of the boxcar function is larger than the spectral resolution, $\Delta\sigma$, then the linear independence of the spectral features is lost [49,72]. This fixes an upper limit on the resolving power, R, of the instrument, known as the *Jaquinot criteria* and given by

$$R \leq \frac{2\pi}{\Omega}, \tag{2.39}$$

where $R = \frac{\sigma}{\Delta\sigma}$ (see Section 1.2) [49,57]. The Jaquinot criteria is evaluated for the SPIRE spectrometer in Section 3.6.2.

2.4.5 Instrumental line shape

Another instrumental effect to consider is the *finite path difference*, which introduces the instrumental line shape (ILS) of a Fourier transform spectrometer. The ILS of any spectrometer defines the shape of a spectral line given a monochromatic input. An ideal interferometer has an infinite optical path difference. In such a case, a single emission line of unit strength oscillating at a frequency of σ_o has a corresponding interferogram of $I(x) = \cos(2\pi\sigma_o x)$ defined over $x = [-\infty, \infty]$ (see Sections 2.2.1 and 2.3.2) [49].

However, practical limitations dictate that interferograms are only measured out to a finite optical path difference [49,55,56]. Mathematically, this is equivalent to multiplying $I(x)$ by a boxcar function (see Equation 2.17), where L is the maximum OPD. As per Section 2.2.3, the spectrum is then convolved by a sinc function [51].

Panel (a) of Figure 2.9 shows a truncated interferogram where $L = 0.5$ cm and $\sigma_o = 10$ cm^{-1}. In Panel (b), the corresponding spectrum clearly shows a sinc function centered at $\sigma = \sigma_o$. This sinc profile determines the spectral resolution (see Section 2.5.1)

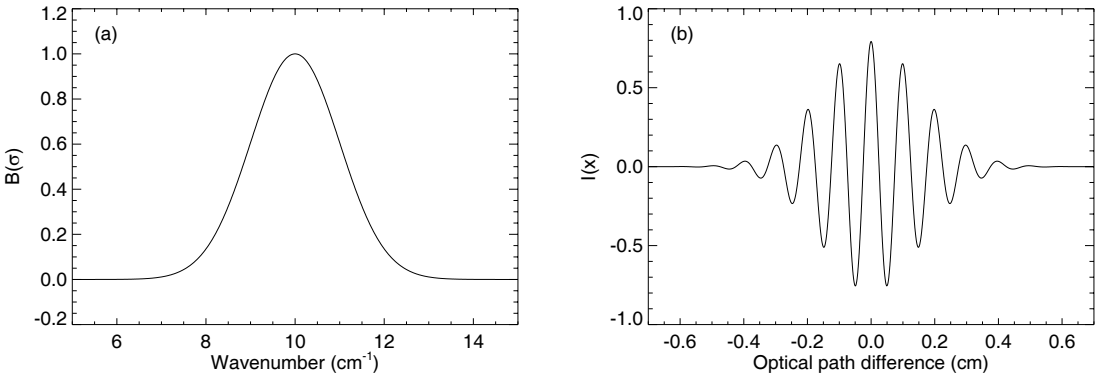

Figure 2.10: Example of a broadened line profile. Panel (a) shows a broadband spectrum given by Equation 2.40 and Panel (b) is its Fourier transform.

and introduces troublesome secondary lobes (see Section 2.5.2), sometimes referred to as *ringing* [49, 56].

2.4.6 Broadband spectrum

While the finite path difference defines the instrumental line shape for a monochromatic input, spectra are rarely composed of infinitely narrow emission (or absorption) features. In reality, light is emitted over a continuum of frequencies [15]. An interferogram composed of broadband radiation is noticeably different from one due only to a monochromatic source.

Consider the gaussian emission feature shown in Panel (a) of Figure 2.10 and given by

$$B(\sigma) = e^{-(\sigma-\sigma_o)^2/2\mu^2}, \qquad [\mathrm{W}] \tag{2.40}$$

where $\sigma_o = 10$ cm^{-1} is the center of the line and $\mu = 1$ cm^{-1} is the standard deviation. The FWHM of a gaussian function is 2.35μ. The corresponding interferogram is shown in Panel (b). Similar to Panel (a) of Figure 2.9, the peaks of the oscillations are spaced 0.1 cm apart. But unlike the interferogram of the narrow line, the envelope of the broadband spectrum decays with OPD [49]. Furthermore, the secondary lobes seen in Panel (b) of Figure 2.9 are not present in broadband spectral features; ringing is only evident when the width of a spectral feature is on the order of a resolution element [49].

2.5 Recovering a spectrum

By definition, a spectrum is real [49]. Section 2.4 unfortunately demonstrated that while a measured interferogram is real, it is also discretely sampled, finite and asymmetric.

This section describes the basic techniques employed to recover a spectrum and account for the instrumental effects introduced by the interferometer.

2.5.1 The discrete Fourier transform

Given a discretely sampled asymmetric interferogram, the spectrum cannot be computed using the continuous Fourier cosine transform (as was suggested in Section 2.3.2). Instead, the spectrum is computed using the complex form of the discrete Fourier transform (DFT) [49, 55, 56]. Using the DFT, the discretely sampled spectrum is given by

$$B(\sigma_j) = \sum_{j=0}^{N-1} I(x_j) e^{-2\pi i \sigma_j x_j / N}, \qquad [\mathrm{W}] \tag{2.41}$$

where N is the number of elements in the interferogram (and the spectrum), and $I(x_j)$ is the interferogram (in watts, or W) sampled at discrete optical path differences, x_j, separated by a sampling interval of Δx (in cm). Each element in $B(\sigma_j)$ is linearly independent of every other element [56]. To determine the corresponding σ_j values, we define the spectal resolution as

$$\Delta\sigma = \frac{\sigma_N}{N}, \qquad [\mathrm{cm}^{-1}] \tag{2.42}$$

where σ_N is the Nyquist frequency introduced in Section 2.4.2 (in cm^{-1}). Combining the above equation with a complementary definition of the sampling interval, $\Delta x = \frac{L}{N}$, and Equation 2.35, the spectral resolution is written as

$$\Delta\sigma = \frac{1}{2L}, \qquad [\mathrm{cm}^{-1}] \tag{2.43}$$

where L is the maximum OPD (in cm) [55, 56].

The instrumental line shape further modifies the spectral resolution [56]. Consider once again a single emission line of unit strength oscillating at a frequency of σ_o. Given the above equation, its full-width at half-maximum is one spectral resolution element, $\Delta\sigma$ [55]. Because of the finite path difference and finite entrance aperture of a Fourier transform spectrometer, the emission line is convolved by a boxcar function of width $\frac{\Omega\sigma_o}{2\pi}$ (see Section 2.4.4) and a sinc function of FWHM $\sim \frac{1.207}{2L}$ (see Section 2.4.5) [49]. In a well-designed Fourier transform spectrometer, the sinc profile dominates and the minimum resolvable element is therefore

$$\Delta\sigma = \frac{1.207}{2L}. \qquad [\mathrm{cm}^{-1}] \tag{2.44}$$

It is important to note that Fourier transforms are rarely calculated by the DFT today [49, 53]. Using the DFT, the computation of a N-point Fourier transform requires on the order of N^2 operations [53, 73]. This computational limitation led to the 1965 development of the fast Fourier transform (FFT) by James W. Cooley and John W. Tukey [73].

Using factorization to eliminate repetitive multiplications, the FFT algorithm reduces the number of operations to, in the best case, $N\log_2 N$ [53, 73]. In this thesis, all Fourier transforms were computed using the fast Fourier transform. For a complete treatment of the FFT algorithm, the reader is referred to Brigham [53].

2.5.2 Apodization

Another problem introduced by the ILS is ringing in the spectrum [49]. As can be seen in Panel (b) of Figure 2.9, the broadened emission line has symmetric side lobes due to the cutoff of the interferogram at $x = \pm 0.5$ cm, as shown in Panel (a). These side lobes may be mistaken as spectral lines, or may mask real spectral features [49, 55].

Apodization is a mathematical filtering technique used to reduce the amplitude of these secondary lobes [55]. An interferogram is apodized by multiplying it by an apodizing function, which is equivalent to convolving the spectrum by the Fourier transform of the apodization function [55]. A correctly chosen apodizing function smooths the edge discontinuities in the interferogram, which in turn minimizes the side lobes in the spectrum [49]. The cost associated with apodization is a reduction in the spectral resolution, as was seen with the ILS (see Section 2.5.1) [55].

Various apodizing functions are currently employed in FTS, such as the triangle, Norton-Beer and Blackman-Harris functions [56, 74–76]. Margaret Tahic recently determined ten optimal apodizing functions that reduce secondary lobes with a minimum loss in spectral resolution [74, 77].

2.5.3 Phase correction

As indicated at the beginning of Section 2.5, a spectrum is an observable quantity and therefore real. Measured interferograms are generally asymmetric such that their Fourier transforms are complex (see Section 2.4.1). Phase correction modifies an asymmetric interferogram to produce a real spectrum [56, 59].

Consider a moving stage with a scan length of $2L$. Given a double-sided interferogram measured from $-L$ to L, the magnitude of the complex spectrum is computed by Equation 2.15. The magnitude contains the same information as the real component of the spectrum if the interferogram were symmetric [56]. However, scanning from $-L$ to L limits the spectral resolution to $\frac{1.207}{2L}$ (see Equation 2.44). By employing phase correction, the maximum OPD is greater, thereby increasing the spectral resolution [56]. The Forman method, explained below, utilizes a *single-sided* interferogram (i.e., an interferogram not sampled to equal OPDs on either side of ZPD) to correct for phase errors [56, 59].

Figure 2.11 is a graphical representation of the Forman method for a linear phase

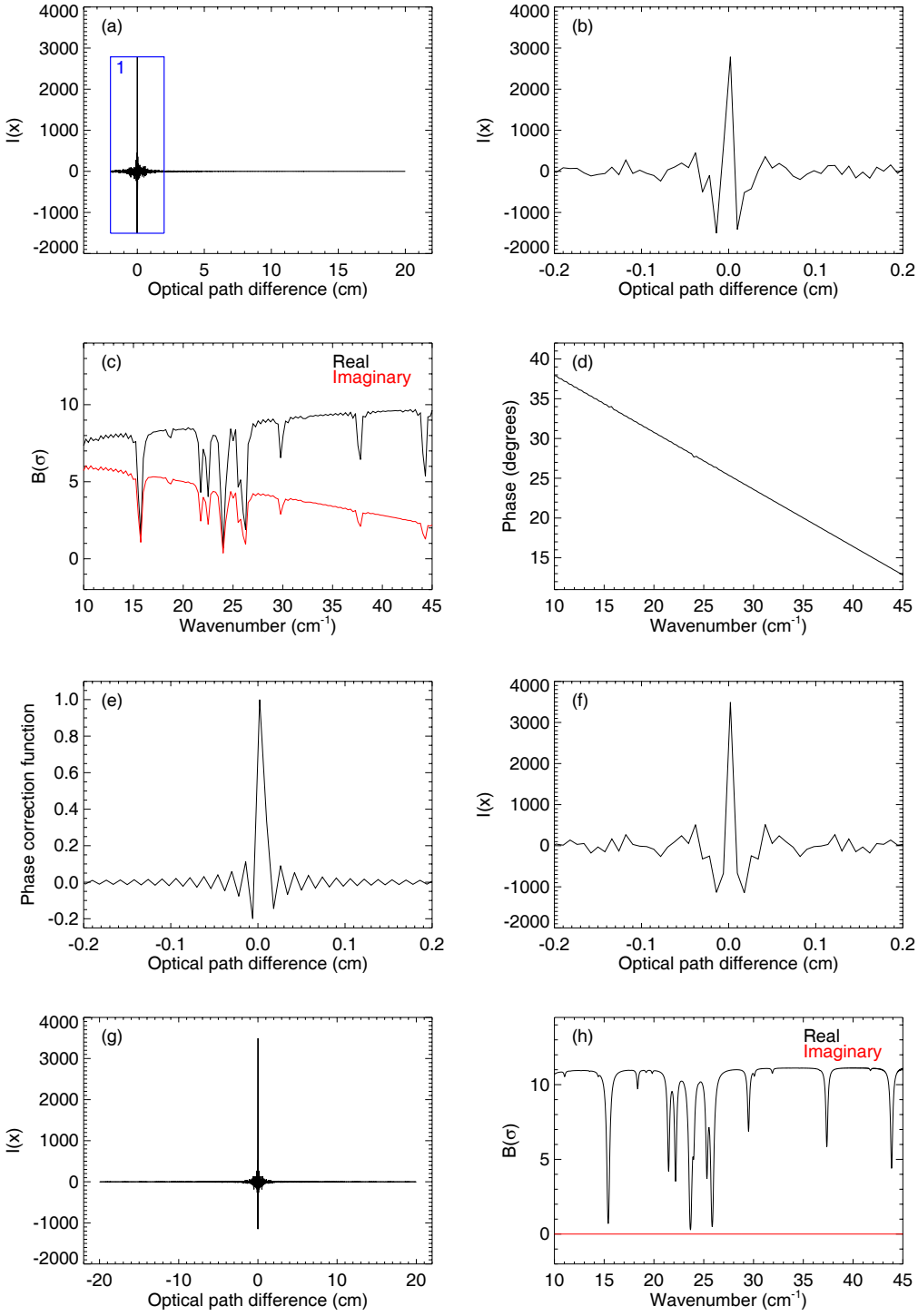

Figure 2.11: Phase correction by the Forman method. Panel (a) shows an asymmetric single-sided interferogram of a model spectrum of atmospheric transmission [78]. The blue box marked "1" denotes the double-sided component. Panel (b) shows the interferogram around ZPD. Panel (c) shows the Fourier transform of the double-sided interferogram. From the phase in Panel (d), the phase correction function is calculated in Panel (e). Panels (f) and (g) show the phase corrected interferogram. The spectrum of the phase-corrected interferogram is shown in Panel (h).

error. Panel (a) shows a single-sided interferogram of a model spectrum of atmospheric transmission [78]. As indicated by the blue box marked "1", a double-sided interferogram of $L = 2$ cm is extracted; Panel (b) shows the double-sided interferogram around ZPD where the asymmetry is clearly visible. The double-sided interferogram is Fourier transformed to yield the real and imaginary components, as shown in black and red, respectively, in Panel (c). The phase, shown in Panel (d), is determined using Equation 2.16. From the phase, ϕ, the phase correction function (PCF) is given by

$$PCF = \mathcal{F}^{-1}[e^{-i\phi}] = \int_{-\infty}^{\infty} e^{-i\phi} e^{i2\pi\sigma x} d\sigma. \tag{2.45}$$

The PCF, shown in Panel (e), is convolved with the single-sided interferogram. This convolution shifts information from the imaginary domain to the real, leaving only noise in the imaginary. As can be seen in Panel (f), the asymmetric interferogram from Panel (b) is now symmetric. Finally, the double-sided component is dropped and the interferogram is mirrored at negative positions, as shown in Panel (g). The spectrum of the phase-corrected interferogram contains only real elements, as shown in Panel (h) [59].

Using phase correction, only a short double-sided component is required in an interferogram. The remainder of the mechanical scan length is used for high resolution spectroscopy, thereby increasing the resolving power of the instrument (see Equation 2.44). Note that the phase correction shown in Figure 2.11 is for a linear phase error due to a sampling error (see Section 2.4.1). Other sources of phase error (such as electronics and optics) introduce higher-order phase errors (see Sections 3.7, 4.9, 5.7, 6.3 and 6.4). For an in-depth discussion of phase correction, the reader is directed to Spencer [79].

2.5.4 Zero filling

The last processing technique of note is zero filling [49, 56, 80]. As indicated in Section 2.5.1, each independent element in a discrete spectrum is $\frac{1.207}{2L}\,\mathrm{cm}^{-1}$ away from its nearest neighbours [49]. However, there are situations where a narrower wavenumber spacing is advantageous or even necessary. (see Sections 4.4 and 4.5) [49, 56]. Zero filling is a computationally efficient technique of interpolating a spectrum onto a finer spectral resolution. [56, 80].

To zero fill an interferogram, new elements of value zero are added to the end of an interferogram. Without adding any new information, zero filling increases the maximum path length of the interferogram. By Equation 2.43, a longer path length corresponds to a finer wavenumber grid [55]. Note that the Nyquist frequency of the spectrum remains the same because zero filling does not change the sampling interval, Δx, of the interferogram [49]. Zero filling is the preferred interpolation technique in FTS because it preserves the sinc function instrumental line shape of the Fourier transform spectrometer [49, 72].

2.6 Summary

Chapter 2 provided a basic overview of Fourier transform spectroscopy. The mathematics underlying Fourier transforms (see Sections 2.1 and 2.2) were introduced to understand the instrumental effects present in an interferogram (see Section 2.4) measured by an ideal Michelson interferometer (see Section 2.3). Section 2.5 outlined the significant post-processing needed to recover a spectrum from a measured interferogram.

Supplemental topics in FTS are introduced in later chapters as needed. For a more in-depth discussion of Fourier transforms, the reader is directed to Bracewell [51]; Brigham [53]; Champeney [50]; James [54]; and Walker [58]. For texts specifically covering FTS, the reader is directed to Bell [55]; Davis, Abrams & Brault [49]; and Griffiths & de Haseth [56].

With this background in place, Chapter 3 examines the Fourier transform spectrometer used in the SPIRE imaging spectrometer.

References

[1] T. Bulfinch. *Bulfinch's Mythology: the Age of Fable, the Age of Chivalry, the Legends of Charlemagne*. Random House: New York, NY (1934).

[2] G. B. Grinnell. *Blackfoot Lodge Tales: The Story of a Prairie People*. University of Nebraska Press: Lincoln, NE (1962).

[3] G. Galilei. *The Sidereal Messenger*. University of Chicago Press: Chicago, IL (1989). Translated by A. van Helden (originally published as "Sidereus Nuncius" in 1610).

[4] G. L. Pilbratt. "Herschel Mission: Status and Observing Opportunities." In *Optical, Infrared, and Millimeter Space Telescopes* (edited by J. C. Mather), **5487**:401–412. Proceedings of the International Society for Optical Engineering (2004).

[5] M. Griffin, B. Swinyard, and L. Vigroux. "The Herschel-SPIRE Instrument." In *Optical, Infrared and Millimeter Space Telescopes* (edited by J. C. Mather), **5487**:413–424. Proceedings of the International Society for Optical Engineering (2004).

[6] A. Poglitsch, *et al.* "The Photodetector Array Camera & Spectrometer (PACS) for the Herschel Space Observatory." In *Optical, Infrared, and Millimeter Space Telescopes* (edited by J. C. Mather), **5487**:425–435. Proceedings of the International Society for Optical Engineering (2004).

[7] T. de Graauw and F. P. Helmich. "Herschel-HIFI: The Heterodyne Instrument for the Far-Infrared." In *The Promise of the Herschel Space Observatory* (edited by G. L. Pilbratt, *et al.*), **SP-460**:45–51. Proceedings of the European Space Agency Symposium in Toledo, Spain (2001).

[8] J. V. Lindner, D. A. Naylor, and B. M. Swinyard. "Simulation of the Performance of ESA's Herschel/SPIRE Imaging Fourier transform spectrometer." In *Optical, Infrared, and Millimeter Space Telescopes* (edited by J. C. Mather), **5487**:469–480. Proceedings of the International Society for Optical Engineering (2004).

[9] E. F. van Dishoeck and F. P. Helmich. "Scientific Drivers for future high-resolution far-infrared spectroscopy in space." In *Submillimetre and Far-infrared Space Instrumentation*, **ESA SP-388**:3–12. Proceedings of the 30th ESLAB symposium (1996).

[10] W. Herschel. "Catalogue of One Thousand new Nebulae and Clusters of Stars." *Philosophical Transactions of the Royal Society of London*, **76**:457–499 (1786).

[11] J. Bally, *et al.* "Externally illuminated young stellar environments in the Orion nebula: *Hubble Space Telescope* planetary camera and ultraviolet observations." *The Astronomical Journal*, **116**(1):293–321 (1998).

[12] J. E. Dyson and D. A. Williams. *The Physics of the Interstellar Medium.* The Graduate Series in Astronomy, 2nd edition. Institute of Physics Publishing: Bristol, England (1997).

[13] W. Herschel. "On Nebulous Stars, properly so called." *Philosophical Transactions of the Royal Society of London*, **81**:71–88 (1791).

[14] W. Herschel. "Experiments on the Refrangibility of the Invisible Rays of the Sun." *Philosophical Transactions of the Royal Society of London*, **90**:284–292 (1800).

[15] B. W. Carroll and D. A. Ostlie. *An Introduction to Modern Astrophysics.* Addison-Wesley: Reading, MA (1996).

[16] F. H. Shu, F. C. Adams, and S. Lizano. "Star Formation in Molecular Clouds: Observation and Theory." *Annual Review of Astronomy and Astrophysics*, **25**:23–81 (1987).

[17] P. André and F. Motte. "FIRST and the earliest stages of star formation." In *Star Formation from the small to the large scale*, **ESA SP-445**:219–226. Proceedings of the 33th ESLAB symposium (2000).

[18] R. Bowers and T. Deeming. *Astrophysics II: Interstellar Matter and Galaxies.* Jones and Bartlett Publishers: Boston, MA (1984).

[19] D. Leverington. *A History of Astronomy from 1890 to present.* Springer: London, England (1995).

[20] R. J. Trumpler. "Absorption of light in the galactic system." *Publications of the Astronomical Society of the Pacific*, **42**(248):214–227 (1930).

[21] H. Karttunen, *et al. Fundamental Astronomy.* 4th edition. Springer-Verlag: Berlin, Germany (2003).

[22] C. A. Beichman. "The IRAS view of the galaxy and the solar system." *Annual Review of Astronomy and Astrophysics*, **25**:521–563 (1987).

[23] S. Chandrasekhar. *Radiative Transfer.* Dover Publications: New York, NY (1960).

[24] W. L. Wolfe. *Handbook of Military Infrared Technology.* US Government Printing Office: Washington, DC (1965).

[25] E. Churchwell, M. G. Wolfire, and D. O. S. Wood. "The infrared emission from dust surrounding newly formed O stars." *The Astrophysical Journal*, **354**:247–261 (1990).

[26] B. Nisini, *et al.* "High-J CO Line Emission from Young Stellar Objects: From ISO to First." In *The Far Infrared and Submillimeter Universe* (edited by G. Pilbratt, S. Volonte, and A. Wilson), **SP-401**:321–324. Proceedings of an ESA Symposium devoted to ESA's "FIRST" mission (1997).

[27] J. W. V. Storey, D. M. Watson, and C. H. Townes. "Far-infrared observations of shocked CO in Orion." *The Astrophysical Journal*, **247**:136–143 (1981).

[28] D. A. Allen. "Infrared Astronomy: an Assessement." *Quarterley Journal of the Royal Astronomical Society*, **18**:188–198 (1977).

[29] H. J. Walker. "A brief history of infrared astronomy." *Astronomy and Geophysics*, **41**(5):5.10–5.13 (2000).

[30] W. S. Holland, *et al.* "SCUBA: a common-user submillimetre camera operating on the James Clerk Maxwell Telescope." *Monthly Notices of the Royal Astronomical Society*, **303**(4):659–672 (1999).

[31] M. Griffin, B. Swinyard, and L. Vigroux. "The SPIRE Instrument for FIRST." In *UV, Optical and IR Space Telescopes and Instruments* (edited by J. B. Breckinridge and P. Jakobsen), **4013**:142–151. Proceedings of the International Society for Optical Engineering (2000).

[32] D. Johnstone, *et al.* "Large-area mapping at 850 microns. II. Analysis of the clump distribution in the ρ Ophiuchi molecular cloud." *The Astrophysical Journal Supplement Series*, **545**(2):327–339 (2000).

[33] D. Johnstone, J. D. Francesco, and H. Kirk. "An Extinction Threshold for Protostellare Cores in Ophiuchus." *The Astrophysical Journal*, **611**(1):L45–L48 (2004).

[34] A. E. Visser and J. S. Richer. "Completion of a SCUBA survey of Lynds dark clouds and implications for low-mass star formation." *The Astrophysical Journal*, **124**(5):2756–2789 (2002).

[35] D. B. Gallagher, W. R. Irace, and M. W. Werner. "The Development and Mission of the Space Infrared Telescope Facility (SIRTF)." In *Optical, Infrared, and Millimeter Space Telescopes* (edited by J. C. Mather), **5487**:13–25. Proceedings of the International Society for Optical Engineering (2004).

[36] H. Murakami. "ASTRO-F Infrared Sky Survey Mission." In *Optical, Infrared, and Millimeter Space Telescopes* (edited by J. C. Mather), **5487**:330–337. Proceedings of the International Society for Optical Engineering (2004).

[37] H. Shibai. "ASTRO-F mission." *Advances in Space Research*, **34**(3):589–593 (2004).

[38] G. L. Pilbratt. "The Herschel mission, scientific objectives, and this meeting." In *The Promise of the Herschel Space Observatory* (edited by G. L. Pilbratt, *et al.*), **SP-460**:11–20. Proceedings of the European Space Agency Symposium in Toledo, Spain (2001).

[39] G. R. Fowles and G. L. Cassiday. *Analytical Mechanics*. Thomson Learning: Toronto, ON (1999).

[40] "Herschel-SPIRE Memorandum of Understanding: Canadian Contribution to the Herschel-SPIRE Instrument Project." Technical Report SPIRE-UCF-PRJ-001614, University of Lethbridge, Lethbridge, AB (2003).

[41] L. D. Spencer, *et al.* "A Fourier transform spectrometer for ground testing of the Herschel/SPIRE instrument." In *Optical, Infrared, and Millimeter Space Telescopes* (edited by J. C. Mather), **5487**:501–512. Proceedings of the International Society for Optical Engineering (2004).

[42] The answer to the ultimate question of life, the universe and everything.

[43] T. Lim, *et al.* "First Results from Herschel-SPIRE Performance Tests." In *Optical, Infrared and Millimeter Space Telescopes* (edited by J. C. Mather), **5487**:460–468. Proceedings of the International Society for Optical Engineering (2004).

[44] B. Sibthorpe, A. Woodcraft, and M. Griffin. "A software simulator for the Herschel-SPIRE imaging photometer." In *Optical, Infrared, and Millimeter Space Telescopes* (edited by J. C. Mather), **5487**:491–500. Proceedings of the International Society for Optical Engineering (2004).

[45] B. M. Swinyard, *et al.* "The Imaging FTS for Herschel SPIRE." In *IR Space Telescopes and Instruments* (edited by J. C. Mather), **4850**:698–709. Proceedings of the International Society for Optical Engineering (2003).

[46] B. M. Swinyard, *et al.* "The FIRST-SPIRE Spectrometer: A Novel Imaging FTS for the Sub-Millimetre." In *UV, Optical and IR Space Telescopes and Instruments* (edited by J. B. Breckinridge and P. Jakobsen), **4013**:196–207. Proceedings of the International Society for Optical Engineering (2000).

[47] B. Swinyard. "Simulations of the FTS Performance." Technical Report SPIRE-RAL-NOT-000413, Rutherford Appleton Laboratory, Oxfordshire, England (2000).

[48] I. Grattan-Guiness. *Joseph Fourier, 1768-1830.* The MIT Press: Cambridge, MA (1972).

[49] S. P. Davis, M. C. Abrams, and J. W. Brault. *Fourier Transform Spectroscopy.* Academic Press: St. Louis, MO (2001).

[50] D. C. Champeney. *Fourier Transforms and their Physical Applications.* Academic Press: St. Louis, MO (1973).

[51] R. M. Bracewell. *Fourier Transforms and Its Applications.* McGraw-Hill Book Co: New York, NY (1965).

[52] J. W. Brown and R. V. Churchill. *Complex Variables and Applications.* 6th edition. McGraw-Hill: New York, NY (1996).

[53] E. O. Brigham. *The Fast Fourier Transform.* Prentice-Hall: Englewood Cliffs, NJ (1973).

[54] J. F. James. *A Student's Guide to Fourier Transforms.* 2nd edition. Cambridge University Press: Cambridge, England (2002).

[55] R. J. Bell. *Infrared Fourier Transform Spectroscopy.* Academic Press: New York, NY (1972).

[56] P. R. Griffiths and J. A. de Haseth. *Fourier Transform Infrared Spectroscopy*. John Wiley and Sons: New York, NY (1986).

[57] E. V. Loewenstein. "The History and Current Status of Fourier Transform Spectroscopy." *Applied Optics*, **5**(5):845–853 (1966).

[58] J. S. Walker. *Fourier Analysis*. Oxford University Press: Oxford, England (1988).

[59] M. L. Forman, W. Steel, and G. A. Vanasse. "Correction of Asymmetric Interferograms Obtained in Fourier Spectroscopy." *Journal of the Optical Society of America*, **56**(1):59–64 (1966).

[60] M. Born and E. Wolf. *Principles of Optics: Electromagnetic Theory of Propagation, Interference and Diffraction of Light*. 6th edition. Cambridge University Press: Cambridge, England (1980).

[61] T. Young. "The Bakerian Lecture: On the Theory of Light and Colours." *Philosophical Transactions of the Royal Society of London*, **92**:12–48 (1802).

[62] R. A. Serway. *Physics for Scientists and Engineers, with Modern Physics*. 4th edition. Saunders College Publishing: Philadelphia, PA (1996).

[63] B. Jaffe. *Michelson and the Speed of Light*. Anchor Books: Garden City, NY (1960).

[64] A. A. Michelson and E. W. Morley. "On the Relative Motion of the Earth and the Luminiferous Ether." *The American Journal of Science*, **34**(203):333–345 (1887).

[65] A. A. Michelson. "Radiation in a Magnetic Field." *The Astrophysical Journal*, **6**(6):131–138 (1897).

[66] K. Dohlen, *et al.* "Optical Design of the SPIRE Instrument for FIRST." In *UV, Optical and IR Space Telescopes and Instruments* (edited by J. B. Breckinridge and P. Jakobsen), **4013**:119–128. Proceedings of the International Society for Optical Engineering (2000).

[67] E. Hecht. *Optics*. 4th edition. Addison-Wesley: San Fransisco, CA (2002).

[68] H. Rubens and R. W. Wood. "Focal Isolation of Long Heat-Waves." *Philosophical Magazine*, **21**(6):249–261 (1911).

[69] J. Connes and P. Connes. "Near-Infrared Planetary Spectra by Fourier Spectroscopy. I. Instruments and Results." *Journal of the Optical Society of America*, **56**(7):896–910 (1966).

[70] H. Nyquist. "Certain topics in telegraph transmission theory." *Transactions of the American Institute of Electrical Engineers*, **47**:617–644 (1928).

[71] R. S. Longhurst. *Geometrical and Physical Optics*. 2nd edition. John Wiley & Sons: New York, NY (1967).

[72] D. A. Naylor. Astronomy Instrument Group, University of Lethbridge, Lethbridge, AB. *Personal Communication* (2005).

[73] J. W. Cooley and J. W. Tukey. "An Algorithm for the Machine Calculation of Complex Fourier Series." *Mathematical Computation*, **19**:297–301 (1965).

[74] M. K. Tahic and D. A. Naylor. "Apodization Functions for Fourier Transform Spectroscopy." In *Fourier Transform Spectroscopy*. Optical Society of America (2005).

[75] R. H. Norton and R. Beer. "New apodizing functions for Fourier spectrometry." *Journal of the Optical Society of America*, **66**(3):259–264 (1976).

[76] F. J. Harris. "On the Use of Windows for Harmonic Analysis with the Discrete Fourier Transform." *Proceedings of the IEEE*, **66**(1):51–83 (1978).

[77] M. K. Tahic. *Fourier transform spectroscopy of the Orion Molecular Cloud*. MSc thesis, University of Lethbridge, Lethbridge, AB (2004).

[78] I. M. Chapman and D. A. Naylor. "Development of a Freely-Distributed, Customizable Atmospheric Radiative Transfer Model." In *Fourier Transform Spectroscopy topical meeting*. Optical Society of America: Alexandria, VA (2004).

[79] L. D. Spencer. *Spectral characterization of the Herschel SPIRE Photometer*. MSc thesis, University of Lethbridge, Lethbridge, AB (2005).

[80] M. L. Forman. "Spectral interpolation: zero fill or convolution." *Applied Optics*, **16**(11):2801 (1977).

[81] D. Griffin, M. Griffin, and B. Swinyard. "SPIRE Design Description." Technical Report SPIRE-RAL-PRJ-000620, Rutherford Appleton Laboratory, Oxfordshire, England (2003).

[82] P. Hargrave and I. Walker. "End Item Data Package: SPIRE Instrument Beam dividers." Technical Report SPIRE-UCF-DOC-002126, Cardiff University, Cardiff, Wales (2004).

[83] M. E. Caldwell, *et al.* "Beam pattern (diffraction) aspects in design of the SPIRE instrument." In *UV, Optical and IR Space Telescopes and Instruments* (edited by J. B. Breckinridge and P. Jakobsen), **4013**:210–220. Proceedings of the International Society for Optical Engineering (2000).

[84] D. H. Martin and J. W. Bowen. "Long-Wave Optics." *IEEE Transactions on Microwave Theory and Techniques*, **41**(10):1676–1690 (1993).

[85] M. Griffin. "SPIRE Sensitivity Models." Technical Report SPIRE-QMW-NOT-000642, Cardiff University, Cardiff, Wales (2004).

[86] K. Dohlen, A. Origné, and M. Ferlet. "Optical alignment verification of the Herschel-SPIRE instrument." In *Optical, Infrared and Millimeter Space Telescopes* (edited by J. C. Mather), **5487**:448–459. Proceedings of the International Society for Optical Engineering (2004).

[87] P. Hargrave. "Filters - Interface Control Document." Technical Report SPIRE-UCF-PRJ-001151, Cardiff University, Cardiff, Wales (2003).

[88] B. Stobie and D. Ferrand. "SPIRE BSM Hardware and software integration process." In *Optical, Infrared and Millimeter Space Telescopes* (edited by J. C. Mather), **5487**:513–522. Proceedings of the International Society for Optical Engineering (2004).

[89] I. Pain, *et al.* "The SPIRE Beam Steering Mirror: a cryogenic 2 axis mechanism for the Herschel Space Observatory." In *IR Space Telescopes and Instruments* (edited by J. C. Mather), **4850**. Proceedings of the International Society for Optical Engineering (2003).

[90] P. A. R. Ade, P. Hamilton, and D. A. Naylor. "An Absolute Dual Beam Emission Spectrometer." In *Fourier Transform Spectroscopy: New Methods and Applications*, pp. 90–92. Optical Society of America: Santa Barbara, CA (1999).

[91] D. A. Naylor, *et al.* "Mach-Zehnder Fourier Transform Spectrometer for astronomical spectroscopy at submillimter wavelengths." In *Millimeter and Submillimeter Detectors for Astronomy* (edited by T. G. Phillips and J. Zmuidzinas), **4855**:540–51. Proceedings of the International Society for Optical Engineering (2003).

[92] D. K. Lambert and P. L. Richards. "Martin-Puplett interferometer: an analysis." *Applied Optics*, **17**(10):1595–1602 (1978).

[93] D. H. Martin and E. Puplett. "Polarised interferometric spectrometry for the millimetre and submillimetre spectrum." *Infrared Physics*, **10**:105–109 (1970).

[94] J. Bock, G. Lilienthal, and B. Swinyard. "Herschel SPIRE Detector Subsystem Specification Document." Technical Report SPIRE-JPL-PRJ-000456, Jet Propulsion Laboratory, Pasadena, CA (2003).

[95] A. Eflving and I. Rasmussen. "Herschel pointing accuracy and calibration procedures." Technical Report SCI-PT-19552, European Space and Technology Centre, Noordwijk, the Netherlands (2003).

[96] J. Fischer, *et al.* "Cryogenic far-infrared laser absorptivity measurements of the Herschel Space Observatory telescope mirror coatings." *Applied Optics*, **43**(19):3765–3771 (2004).

[97] E. Sein, *et al.* "A Φ 3.5 M SiC telescope for HERSHEL Mission." In *IR Space Telescopes and Instruments* (edited by J. C. Mather), **4850**:606–618. Proceedings of the International Society for Optical Engineering (2003).

[98] P. C. Hargrave. Astronomy Instrumentation Group, Cardiff University, Cardiff, Wales. *Personal Communication* (2005).

[99] P. C. Hargrave, *et al.* "In-Flight Calibration Sources for Herschel-SPIRE." In *IR Space Telescopes and Instruments* (edited by J. C. Mather), **4850**:638–649. Proceedings of the International Society for Optical Engineering (2003).

[100] P. Hargrave and M. Griffin. "Spectrometer Calibrator Subsystem Design Description." Technical Report SPIRE-QMW-PRJ-001104, Cardiff University, Cardiff, Wales (2001).

[101] J. E. Chamberlain. *The Principles of Interferometric Spectroscopy*. John Wiley and Sons: Chichester, England (1979). Edited by G. W. Chantry and N. W. B. Stone.

[102] "Cernox RTD thermistors." Product information from Lakeshore Corporation, Westerville, OH. Web address: *http://www.lakeshore.com/temp/sen/crtd.html*.

[103] K. J. Åström and T. Hägglund. "The future of PID control." *Control Engineering Practice*, **9**(11):1163–1175 (2001).

[104] C. Lee, P. A. R. Ade, and C. V. Haynes. "Self supporting filters for compact focal plane designs." In *Submillimetre and Far-Infrared Space Instrumentation*, **SP-388**:81–83. Proceedings of the 30th ESLAB Symposium: Noordwijk, The Netherlands (1996).

[105] R. Ulrich, K. F. Renk, and L. Genzel. "Tunable Sumillimeter interferometers of the Fabry-Perot type." *IEEE Transactions on Microwave Theory and Techniques*, **11**(5):363–371 (1963).

[106] T. Fulton. "SPIRE Detector Response and Glitch Characterization." Technical Report SPIRE-UOL-REP-002207, University of Lethbridge, Lethbridge, AB (2005).

[107] D. Pouliquen. "Herschel-SPIRE Spectrometer mirror mechanism design description." Technical Report LAM-PJT-SPI-NOT-200008, Laboratoire d'Astrophysique de Marseille, Marseille, France (2001).

[108] "Exposed linear encoders." Product information from Heidenhain Corporation, Schaumburg, IL. Web address: *http://www.heidenhain.com/Products/ExposedLinear /lip.htm*.

[109] D. A. Naylor, *et al.* "Data processing pipeline for a time-sampled imaging Fourier transform spectrometer." In *Imaging Spectrometry X* (edited by S. S. Shen and P. E. Lewis), **5546**:61–72. Proceedings of the International Society for Optical Engineering (2004).

[110] P. Hargrave and C. Tucker. "End Item Data Package: SPIRE 300mK Spectrometer filters - PFM." Technical Report HSO-CDF-EIDP-055, Cardiff University, Cardiff, Wales (2004).

[111] M. J. Griffin, J. J. Bock, and W. K. Gear. "Relative performance of filled and feedhorn-coupled focal-plane architecture." *Applied Optics*, **41**(31):6543–6554 (2002).

[112] T. Lim. Space Science and Technology Division, Rutherford Appleton Laboratory, Oxfordshire, England. *Personal Communication* (2004).

[113] G. Chattopadhyay, *et al.* "Feedhorn Coupled Bolometer Arrays for SPIRE: Design, Simulation, and Measurements." *IEEE Transactions on Microwave Theory and Techniques*, **51**(10):2139–2146 (2003).

[114] B. Rownd, *et al.* "Design and performance of feedhorn-coupled bolometer arrays for SPIRE." In *Millimeter and Submillimeter Detectors for Astronomy* (edited by T. G. Phillips and J. Zmuidzinas), **4855**:510–519. Proceedings of the International Society for Optical Engineering (2003).

[115] D. A. Harper, *et al.* "Heat trap: an optimized far infrared field optics system." *Applied Optics*, **15**(1):53–60 (1976).

[116] J. A. Murphy. "Aperture Efficiencies of Large Axisymmetric Reflector Antennas Fed by Conical Horns." *IEEE Transactions on Antennas and Propagation*, **36**(4):570–575 (1988).

[117] J. A. Murphy and R. Padwan. "Radiation patterns of few-moded horns and condensing lightpipes." *Infrared Physics*, **31**(5):291–299 (1991).

[118] K. Rohlfs. *Tools of Radio Astronomy*. Astronomy & Astrophysics Library. Springer-Verlag: Berlin, Germany (1986).

[119] J. Glenn. Center for Astrophysics and Space Astronomy, University of Colorado, Boulder, CO. *Personal Communication* (2005).

[120] R. A. Waldron. *The Theory of Waveguides and Cavities*. Maclaren & Sons Ltd: London, England (1967).

[121] J. C. G. Lesurf. *Millimetre-wave Optics, Devices and Systems*. IOP Publishing Ltd: Bristol, England (1990).

[122] N. Marcuvitz. *Waveguide Handbook*. IEE Electromagnetic Waves Series 21. Peter Peregrins Ltd: London, England (1986).

[123] J. L. Doane. "Propagation and mode coupling in corrugated and smooth-walled circular waveguides." In *Infrared and Millimeter Waves, Volume 13: Millimeter Components and Techniques, Part IV* (edited by K. J. Button), pp. 123–170. Academic Press: Orlando, FL (1985).

[124] F. R. Arams. *Infrared-to-millimeter wavelength detectors*. Artech House: Norwood, MA (1973).

[125] P. Davis, T. Fulton, and D. Naylor. "Band edges of the SPIRE PFM1 spectrometer." Technical Report SPIRE-UOL-REP-002420, University of Lethbridge, Lethbridge, AB (2005).

[126] J. Glenn, *et al.* "Numerical optimization of integrating cavities for diffraction-limited millimeter-wave bolometer arrays." *Applied Optics*, **41**(1):136–142 (2002).

[127] A. D. Turner, *et al.* "Silicon nitride micromesh bolometer array for submillimeter astrophysics." *Applied Optics*, **40**(28):4921–31 (2001).

[128] M. Griffin, *et al.* "SPIRE - a bolometer instrument for FIRST." In *Advanced Technology MMW, Radio, and Terahertz Telescopes* (edited by T. G. Phillips), **3357**:404–415. Proceedings of the International Society for Optical Engineering (1998).

[129] P. L. Richards. "Bolometers for infrared and millimeter waves." *Journal of Applied Physics*, **76**(1):1–24 (1994).

[130] W. Holland, W. Duncan, and M. Griffin. "Bolometers for Submillimeter and Millimeter Astronomy." In *Single-Dish Radio Astronomy: Techniques and Applications* (edited by S. Stanimirović, *et al.*), **278**:463–491. ASP Conference Series (2002).

[131] R. V. Sudiwala, M. J. Griffin, and A. L. Woodcraft. "Thermal modelling and characterisation of semiconductor bolometers." *International Journal of Infrared and Millimeter Waves*, **23**(4):545–573 (2002).

[132] H. T. Nguyen, *et al.* "A Report on Laboratory Performance of the Spectroscopic Detector Arrays for SPIRE/HSO." In *Millimeter and Submillimeter Detectors for Astronomy II* (edited by J. Zmuidzinas, W. S. Holland, and S. Withington), **5498**:196–207. Proceedings of the International Society for Optical Engineering (2004).

[133] D. Naylor, T. Fulton, and P. Davis. "Phase study of SPIRE PFM1 Spectrometer Data." Technical Report SPIRE-UOL-REP-002421, University of Lethbridge, Lethbridge, AB (2005).

[134] E. L. Dereniak and D. G. Crowe. *Optical Radiation Detectors*. John Wiley and Sons: New York, NY (1984).

[135] F. Pinsard. "Herschel/SPIRE Detector Control Unit Design document." Technical Report SPIRE-SAP-PRJ-001243, Commissariat à l'Energie Atomique Service d'Astrophysique, Saclay, France (2005).

[136] "Interactive Data Language." Product information from Research Systems Inc., Boulder, CO. Web address: *http://www.rsinc.com/idl*.

[137] N. Dale, C. Weens, and M. Headington. *Programming and Problem Solving with C++*. 2nd edition. Jones and Bartlett Publishers: Sudbury, MA (2000).

[138] P. Léna. *Observational Astrophysics*. Springer-Verlag: Berlin, Germany (1988). Translated by A. R. King (originally published as "Astrophysique: Méthodes physique de l'observation" in 1986).

[139] B. Swinyard and M. Griffin. "Operating Modes for the SPIRE Instrument." Technical Report SPIRE-RAL-PRJ-000320, Rutherford Appleton Laboratory, Oxfordshire, England (2003).

[140] B. Swinyard. "Implications of reduced SMEC scan speed range." Technical Report SPIRE-RAL-NOT-001543, Rutherford Appleton Laboratory, Oxfordshire, England (2003).

[141] "CDR Herschel Micro-Vibration Analysis Report." Technical Report H-P-2-ASP-AN-0773, Systems Mechanical Analyses team, Alcatel Space (2004).

[142] J.-P. Baluteau. Laboratoire d'Astrophysique de Marseille, Marseille, France. *Personal Communication* (2005).

[143] W. H. Press, *et al. Numerical Recipes: The Art of Scientific Computing*. Cambridge University Press: Cambridge, England (1986).

[144] S. K. Park and K. W. Miller. "Random number generators: Good ones are hard to find." *Communications of the Association for Computing Machinery*, **31**(10):1192–1201 (1988).

[145] G. E. P. Box and M. E. Muller. "A Note on the Generation of Random Normal Deviates." *Annals of Mathematical Statistics*, **29**(2):610–611 (1958).

[146] P. Hargrave. "Spectrometer Calibrator Flight Model & Flight Space Interface Control Document." Technical Report SPIRE-UCF-PRJ-001149, Cardiff University, Cardiff, Wales (2004).

[147] M. J. Eccles, M. E. Sim, and K. P. Tritton. *Low light level detectors in astronomy.* Cambridge University Press: Cambridge, England (1983).

[148] J. C. G. Lesurf. *Information and Measurement.* 2nd edition. CRC Press: Boca Baton, FL (2001).

[149] R. N. Bracewell. "The Fourier Transform." *Scientific American*, **260**(6):86–95 (1989).

[150] R. J. Hanisch, *et al.* "Definition of the Flexible Image Transport System (FITS)." *Astronomy and Astrophysics*, **376**(1):359–380 (2001).

[151] P. A. Collins, *et al.* "A Ground Calibration Facility for HERSCHEL-SPIRE." In *IR Space Telescopes and Instruments* (edited by J. C. Mather), **4850**:628–637. Proceedings of the International Society for Optical Engineering (2003).

[152] P. Hargrave. "SPIRE AIV Cryogenic Black Body Source and Filter Stack." Technical Report HSO-CDF-EIDP-069, Cardiff University, Cardiff, Wales (2003).

[153] A. Rebolledo, P. Davis, and T. Fulton. "SPIRE Fourier Transform - User Guide." Technical Report SPIRE-UOL-DOC-002495, University of Lethbridge, Lethbridge, AB (2005).

[154] "Java Technology." Product information from Sun Microsystems, Santa Clara, CA. Web address: *http://java.sun.com/*.

[155] "FIR series Optically Pumped Far Infrared Lasers." Product information from Edinburgh Instruments, Livingston, Scotland. Web address: *http://www.edinst.com/fir.htm*.

[156] M. Inguscio, *et al.* "A review of frequency measurements of optically pumped lasers from 0.1 to 8 THz." *Journal of Applied Physics*, **60**(12):R161–R192 (1986).

[157] A. Li and B. T. Draine. "Infrared emission from interstellar dust. II. The diffuse interstellar medium." *The Astrophysical Journal*, **554**(2):778–802 (2001).

[158] J. Lindner. "Dusty galaxies: modelling spectral energy distributions." *Canadian Undergraduate Physics Journal*, **2**(2):7–12 (2003).

[159] P. F. Goldsmith, E. A. Bergin, and D. C. Lis. "Carbon monoxide and dust column densities: the dust-to-gas ratio and structure of three giant molecular cloud cores." *The Astrophysical Journal*, **491**:615–637 (1997).

[160] F. Motte, P. André, and R. Neri. "The initial conditions of star formation in the ρ Ophiuchi main cloud: wide-field millimeter continuum mapping." *Astronomy and Astrophysics*, **336**:150–172 (1998).

[161] M. A. Gordon. "Dust emission as a quantitative probe of star-forming regions." *Astronomy and Astrophysics*, **301**:853–864 (1995).

[162] J. Glenn and T. R. Hunter. "A comparison of tracers of cool gas in galaxies and the $^{12}CO/^{13}CO$ luminosity ratio in luminous infrared galaxies." *The Astrophysical Journal Supplement Series*, **135**(2):177–182 (2001).

[163] R. H. Hildebrand. "The Determination of Cloud Masses and Dust Characteristics from Submillimetre Thermal Emission." *Quarterley Journal of the Royal Astronomical Society*, **24**:267–282 (1983).

[164] J. P. Bernard, *et al.* "PRONAOS observations of MCLD 123.5+24.9: cold dust in the Polaris cirrus cloud." *Astronomy and Astrophysics*, **347**:640–649 (1999).

[165] E. Serabyn and E. W. Weisstein. "Fourier transform spectroscopy of the Orion Molecular Cloud Core." *The Astrophysical Journal*, **451**:238–251 (1995).

[166] R. Chini, *et al.* "Dust filaments and star formation in OMC-2 and OMC-3." *The Astrophysical Journal*, **474**:L135–L138 (1997).

[167] D. Johnstone, A. M. S. Boonman, and E. F. van Dishoeck. "Astrochemistry of submillimeter sources in Orion." *Astronomy and Astrophysics*, **412**:157–174 (2003).

[168] T. D. Varberg and K. M. Evenson. "Accurate far-infrared rotational frequencies of carbon monoxide." *The Astrophysical Journal*, **385**:763–765 (1992).

[169] P. F. Bernath. *Spectra of Atoms and Molecules*. 2nd edition. Oxford University Press: Oxford, England (2005).

[170] D. M. Watson, *et al.* "Detection of CO $J = 21 \rightarrow 20$ (124.2 μm) and $J = 22 \rightarrow 21$ (118.6 μm) emission from the Orion Nebula." *The Astrophysical Journal*, **239**:L129–L132 (1980).

[171] S. E. Cummins, R. A. Linke, and P. Thaddeus. "A Survey of the Millimeter-Wave Spectrum of Sagittarius B2." *The Astrophysical Journal Supplement Series*, **60**:819–878 (1986).

[172] R. P. Feynman, R. B. Leighton, and M. Sands. *The Feynman Lectures on Physics*. Addison-Wesley: Reading, MA (1963).

[173] R. Phillips. *Radiative Transfer Modelling of Star Formation Regions*. PhD thesis, University of Kent at Canterbury, Canterbury, England (1999).

[174] G. A. Blake, *et al.* "Molecular abundances in OMC-1 - The chemical composition of interstellar molecular clouds and the influence of massive star formation." *The Astrophysical Journal*, **315**:621–645 (1987).

[175] B. E. Turner. "A molecular line survey of Sagittarius B2 and Orion-KL from 70 to 115 GHz. II - Analysis of the data." *The Astrophysical Journal Supplement Series*, **76**:617–686 (1991).

[176] L. S. Rothman, *et al.* "The HITRAN 2004 Molecular Spectroscopic Database." *Journal of Quantitative Spectroscopy and Radiative Transfer*, **96**(2):139–204 (2005).

[177] H. M. Pickett, *et al.* "Submillimeter, millimeter, and microwave spectral line catalog." *Journal of Quantitative Spectroscopy and Radiative Transfer*, **60**(5):883–890 (1998).

[178] N. Jacquinet-Husson, *et al.* "The 2003 edition of the GEISA/IASI spectroscopic database." *Journal of Quantitative Spectroscopy and Radiative Transfer*, **95**(4):429–467 (2005).

[179] M. Harwit. *Astrophysical Concepts*. 2nd edition. Springer-Verlag: New York, NY (1988).

[180] R. C. Hilborn. "Einstein coefficients, cross sections, f values, dipole moments, and all that." *American Journal of Physics*, **50**(11):982–986 (1982).

[181] M. Šimečková, *et al.* "Einstein A-coefficients and statistical weights for molecular absorption transitions in the HITRAN database." *Journal of Quantitative Spectroscopy and Radiative Transfer*, **98**(1):130–155 (2006).

[182] T. Onaka and T. Nakagawa. "SPICA: A 3.5 m space infrared telescope for mid- and far-infrared astronomy." *Advances in Space Research*, **36**(6):1123–1127 (2005).

[183] P. J. Mohr and B. N. Taylor. "CODATA recommended values of the fundamental physical constants: 2002." *Reviews of Modern Physics*, **77**(1):1–107 (2005).

[184] "Le Système international d'unités (SI)." 7th edition, Bureau International des Poids et Mesures, Sèvres Cedex, France (1998). Web address: *http://www.bipm.org/utils/en/pdf/si-brochure.pdf*.

[185] B. N. Taylor. "Guide for the Use of the International System of Units (SI)." NIST Special Publication 811, National Institute of Standards and Technology, Gaithersburg, MD (1995). Web address: *http://physics.nist.gov/cuu/pdf/sp811.pdf*.

[186] D. S. Liepman. "Mathematical constants." In *Handbook of Mathematical Functions with Formulas, Graphs, and Mathematical Tables* (edited by M. Abramowitz and I. A. Stegun), pp. 1–4. Dover Publications: New York, NY (1965).

[187] I. S. Glass. *Handbook of Infrared Astronomy*. Cambridge Observing Handbooks for Research Astronomers. Cambridge University Press: Cambridge, England (1999).

[188] C. H. Edwards and D. E. Penney. *Calculus with analytic geometry and early transcendentals*. 5th edition. Prentice Hall: Upper Saddle River, NJ (1997).

[189] D. Freedman, *et al. Statistics*. 2nd edition. W. W. Norton and Company: New York, NY (1991).

[190] L. S. Rothman, *et al.* "The HITRAN Molecular Spectroscopic Database and HAWKS (HITRAN Atmospheric Workstation): 1996 Edition." *Journal of Quantitative Spectroscopy and Radiative Transfer*, **60**(5):665–710 (1998).

[191] J. B. Tatum. "The interpretation of intensities in diatomic molecular spectra." *The Astrophysical Journal Supplement Series*, **14**:21–56 (1967).

[192] L. S. Rothman. Atomic and Molecular Physics Division, Harvard-Smithsonian Center for Astrophysics, Cambridge, MA. *Personal Communication* (2005).

[193] M. D. Harmony. *Introduction of Molecular Energies and Spectra*. Holt, Rinehart & Winston: New York, NY (1972).

[194] R. R. Gamache and L. S. Rothman. "Extension of the HITRAN database to non-LTE applications." *Journal of Quantitative Spectroscopy and Radiative Transfer*, **48**(5-6):519–525 (1992).

[195] J. J. Sakurai. *Modern Quantum Mechanics*. 2nd edition. Pearson Education: Delhi, India (1994).

[196] E. U. Condon and G. H. Shortley. *The Theory of Atomic Spectra*. 2nd edition. Cambridge University Press: Cambridge, England (1963).

[197] W. Gordy and R. L. Cook. *Microwave Molecular Spectroscopy*. 3rd edition. John Wiley & Sons: New York, NY (1984).

[198] G. Herzberg. *Molecular Spectra and Molecular Structure: I. Spectra of Diatomic Molecules*. 2nd edition. D. Van Nostrand Company: Princeton, NJ (1950).

[199] H. W. Kroto. *Molecular Rotation Spectra*. 2nd edition. Dover Publications: New York, NY (1992).

[200] C. H. Townes and A. L. Schawlow. *Microwave Spectroscopy*. McGraw-Hill Book Company: New York, NY (1955).

[201] L. S. Rothman, *et al.* "The HITRAN molecular spectroscopic database: edition of 2000 including updates through 2001." *Journal of Quantitative Spectroscopy and Radiative Transfer*, **82**(1-4):5–44 (2003).

[202] S. S. Penner. *Quantitative Molecular Spectroscopy and Gas Emissivities*. Addison-Wesley: Reading, MA (1959).

Appendix B

Spectral Characterization of the Herschel SPIRE Photometer

Locke Dean Spencer

B.Sc. Engineering Physics, University of Alberta, 2003

A Thesis
Submitted to the School of Graduate Studies
of the University of Lethbridge
in Partial Fulfilment of the
Requirements of the Degree

Master of Science

Department of Physics
University of Lethbridge
Lethbridge, Alberta, Canada

Chapter 2

Fourier Transform Spectroscopy and FTS Data Processing

2.1 Overview

Fourier transform spectroscopy (FTS) has gained an appreciable following in astronomy as a spectroscopic technique to maximize input flux utilization with broad spectral coverage and variable spectral resolution[27]. This chapter gives an overview of Fourier transform spectroscopy and its underlying mathematical principles. Fourier series and integrals are introduced. A description of a classical Michelson interferometer is included. The chief advantages of FTS are reviewed including the Jacquinot and Fellgett advantages. FTS limitations such as noise, sampling, and natural apodization are also discussed.

2.2 Brief history

A technique for analyzing periodic functions was developed by Jean Baptiste Joseph, Baron de Fourier[28, 29] (1768-1830), which is now known as *Fourier's Theorem* [30]. Fourier's theorem was well ahead of its time and it was not until much later that it became appreciated as a powerful analytical tool. In fact, Fourier had difficulty getting his results published [31, p. 187].

Fourier transform interferometry was initiated in 1880 when Dr. Albert A. Michelson invented the interferometer[32, 33, 34] and realized the basic concepts of Fourier transform spectroscopy[35, 36], although it was not exploited due to the lack of computational power as well as extremely poor detector sensitivity at the time[37, 38, 39]. Michelson invented a mechanical analog computer (called a harmonic analyzer[40]) capable of performing Fourier transforms of about 80 data points, but this was not extensively used for Fourier transform spectroscopy. Michelson measured 'visibility curves'[41] with his eye and made crude estimates of the spectrum. The Michelson interferometer is described later in section 2.6 of this chapter.

The first interferogram (see section 2.6) was recorded in 1911 by Rubens and Wood[42] where a microradiometer was used to record the signal. The Fourier transform of the interferogram was not calculated, but rather the spectrum was estimated and the interferogram of the estimated spectrum was compared to the measured interferogram. Fellgett was the first to apply the Fourier transform to interferograms numerically in 1958 and was also the first to recognize the multiplex advantage of FTS spectrometers (see section 2.9)[43]. In 1960, Jaquinot was the first to realize the throughput advantage of an FTS over

other spectrometers (see section 2.8)[44]. The first application of FTS to astronomy was published in 1969 by Janine & Pierre Connes[45]. An important development in analysis of FTS data was the fast Fourier transform (FFT) algorithm, developed by Cooley and Tukey in 1965[2], which was introduced to Fourier spectroscopy by Forman[46] in 1966.

2.3 Fourier series

Fourier's theorem states that a periodic function, $f(z)$, of period Z_o, can be expressed as a series of harmonic functions whose periods are integral submultiples of Z_o (i.e. Z_o, $Z_o/2$, $Z_o/3$, etc.). The mathematical form of the Fourier Series representation is given by:

$$f(z) = \frac{a_o}{2} + \sum_{n=1}^{\infty}(a_n \cos(n\omega_o z) + b_n \sin(n\omega_o z)), \tag{2.1}$$

where

$$\omega_o = \frac{2\pi}{Z_o}, \tag{2.2}$$

is the fundamental frequency and the functions $\cos(n\omega_o z)$, and $\sin(n\omega_o z)$ form a set of mutually orthogonal basis vectors. The constants a_o, a_n, and b_n are determined using the following relations (see appendix A for further details):

$$a_o = \frac{2}{Z_o}\int_{z_1}^{z_1+Z_o} f(z)dz, \tag{2.3}$$

$$a_n = \frac{2}{Z_o}\int_{z_1}^{z_1+Z_o} f(z)\cos(n\omega_o z)dz \qquad n = 1, 2, 3, \ldots , \tag{2.4}$$

and,

$$b_n = \frac{2}{Z_o}\int_{z_1}^{z_1+Z_o} f(z)\sin(n\omega_o z)dz \qquad n = 1, 2, 3, \ldots . \tag{2.5}$$

By introducing negative values of n into equation 2.1 and expressing it in exponential form (see appendix A for further detail), the expression becomes:

$$f(z) = \sum_{n=-\infty}^{\infty} d_n e^{in\omega_o z}, \tag{2.6}$$

where

$$d_n = \frac{1}{Z_o} \int_{z_1}^{z_1+Z_o} f(z) e^{-in\omega_o z} dz. \tag{2.7}$$

The amplitudes of the spectral components are split between positive frequencies (positive n), and negative frequencies (negative n).

2.3.1 Dirichlet conditions

Functions must adhere to certain conditions in order for the Fourier series to exist (weak Dirichlet condition) and be convergent (strong Dirichlet conditions). These conditions are called the Dirichlet conditions[47, 48]. The weak Dirichlet condition states that in order for a function, $f(z)$, to have a Fourier series:

- $f(z)$ must be absolutely integrable over one period,

$$\text{i.e. } \int_{Z_o} |f(z)| dz < \infty. \tag{2.8}$$

If a function $f(z)$ satisfies the weak Dirichlet condition, the existence of a Fourier series is guaranteed, but the series may not converge at every point. Similarly, if a function has an infinite number of maxima or minima in one period, then the function contains an appreciable number of components of frequencies approaching infinity. Thus, for a convergent Fourier series, in addition to the weak Dirichlet condition, the strong conditions

must be met. The strong Dirichlet conditions state that, in order for a function to have a convergent Fourier series:

- $f(z)$ must have a finite number of extrema in one period,
- $f(z)$ must have a finite number of finite discontinuities in one period.

Any periodic waveform that can be generated in the laboratory satisfies strong Dirichlet conditions, and hence possesses a convergent Fourier series.

2.4 Fourier integrals

As the limits of the Fourier series extend closer to infinity, and the spacing between harmonic frequencies decreases, the Fourier series representation (equation 2.6) can be replaced by the Fourier integral representation as follows:

$$f(z) = \int_{\sigma=-\infty}^{\infty} F(\sigma) e^{i2\pi\sigma z} d\sigma, \tag{2.9}$$

where the expression is known as the inverse complex Fourier transform[49, 50]. In this case, optical path difference (OPD), i.e. z (cm), and wavenumber, σ (cm^{-1}), are used as reciprocal Fourier transform variables. Another common Fourier transform pair of variables is time (t), measured in seconds, and frequency (ν), measured in Hz. The term $F(\sigma)$ is given by

$$F(\sigma) = \int_{-\infty}^{+\infty} f(z) e^{-i2\pi\sigma z} dz, \tag{2.10}$$

and is known as the forward complex Fourier transform. The complex Fourier transform can be expressed in terms of sine and cosine transforms as follows:

$$\begin{aligned} f(z) &= \int_{\sigma=-\infty}^{\infty} F(\sigma) e^{i2\pi\sigma z} d\sigma \\ &= \int_{-\infty}^{+\infty} \frac{a(\sigma)}{2} \cos(2\pi\sigma z) d\sigma + \int_{-\infty}^{+\infty} \frac{-i^2 b(\sigma)}{2} \sin(2\pi\sigma z) d\sigma \qquad (2.11) \\ &= \int_{-\infty}^{+\infty} \frac{a(\sigma)}{2} \cos(2\pi\sigma z) d\sigma + \int_{-\infty}^{+\infty} \frac{b(\sigma)}{2} \sin(2\pi\sigma z) d\sigma, \end{aligned}$$

where

$$F(\sigma) = \frac{a(\sigma) - ib(\sigma)}{2}, \qquad (2.12)$$

and the Fourier coefficients, $a(\sigma)$ and $b(\sigma)$, are given by:

$$a(\sigma) = 2 \int_{-\infty}^{+\infty} f(z) \cos(2\pi\sigma z) dz, \qquad (2.13)$$

and

$$b(\sigma) = 2 \int_{-\infty}^{+\infty} f(z) \sin(2\pi\sigma z) dz. \qquad (2.14)$$

Inspection of equations 2.13 and 2.14 shows that under certain symmetry conditions these coefficients are trivial. For example when the function $f(z)$ is even, $b(\sigma) = 0$ for all σ and its Fourier transform will contain only cosine terms, which are themselves even functions. In the same way, when the function $f(z)$ is odd, $a(\sigma) = 0$ for all σ, and its Fourier transform will contain only sine functions, which are odd functions. Equations 2.9 and 2.10 are referred to as Fourier transform pairs [50].

2.5 Parseval's theorem

Parseval's theorem[28, 51], as applied to Fourier series, states that the energy in a finite signal (or energy per period for a periodic signal, or power for an infinite signal) is

the same when calculated in either reciprocal Fourier domain (e.g. time and frequency, or OPD and wavenumber). The signal energy, E_f, for a signal $f(z)$ (finite) is defined as:

$$E_f = \int_{-\infty}^{+\infty} |f(z)|^2 dz = \int_{-\infty}^{+\infty} |F(\sigma)|^2 d\sigma. \tag{2.15}$$

The energy of the signal $f(z)$ results from energies contributed by all of the spectral components of the signal, $F(\sigma)$. The total signal energy is the area under $|F(\sigma)|^2$ or $|f(z)|^2$ from $-\infty$ to $+\infty$. Consider a small band $\Delta\sigma(\sigma_o)$ (where $\Delta\sigma \to 0$), centred at frequency σ_o. The energy ΔE_f of the spectral component in this band is the area of $|F(\sigma)|^2$ under the band $\Delta\sigma$:

$$\Delta E_f(\sigma_o) = |F(\sigma_o)|^2 \Delta\sigma. \tag{2.16}$$

The total signal energy is the sum of all such energy bands in the spectrum. Therefore, $|F(\sigma)|^2$ is the energy spectral density, that is energy per unit bandwidth; consequently, $F(\sigma)$ is the signal spectral density, that is signal per root unit bandwidth.

2.6 The Michelson interferometer

The simplest form of FTS is a Michelson interferometer[30, 38, 52], as is shown in figure 2.1. The Michelson interferometer operates on the principle of amplitude division and interference of light. The path that light travels through a Michelson interferometer is summarized as follows (see figure 2.1):

1. Light from a source enters the interferometer (and is collimated by a lens or mirror if required) resulting in a plane wave.

2. The resulting plane wave is then split (ideally into two equal amplitude waves) by the beamsplitter.

3. These waves travel and reflect off of the FTS mirrors (one fixed (3a) and one movable (3b)) and are directed back on themselves towards the beamsplitter.

4. The reflected beams are recombined at the beamsplitter, where two resultant beams are formed, one traveling back to the source and the other one to the detector.

5. The optical detector records the interference of the combined beams of light, resulting in an intensity variation that depends on the phase difference between the recombined beams.

Interference is accomplished by the light in each path of the interferometer traveling a different number of cycles due to the OPD between the two paths. Different amounts of optical path traveled correspond to different phases upon recombination, and therefore different levels of interference as the OPD changes. When the OPD is zero, all frequency components exhibit zero phase difference and constructive interference occurs simultaneously for all wavelengths; this position of the FTS moving mirror is referred to as the position of zero path difference (ZPD).

The variation of optical path difference by the motion of the moving mirror from one limit, through the point of ZPD, to the other limit constitutes a scan (e.g. $-L \rightarrow ZPD \rightarrow +L$). The optical signal recorded by the detector for the duration of a scan is called an interferogram.

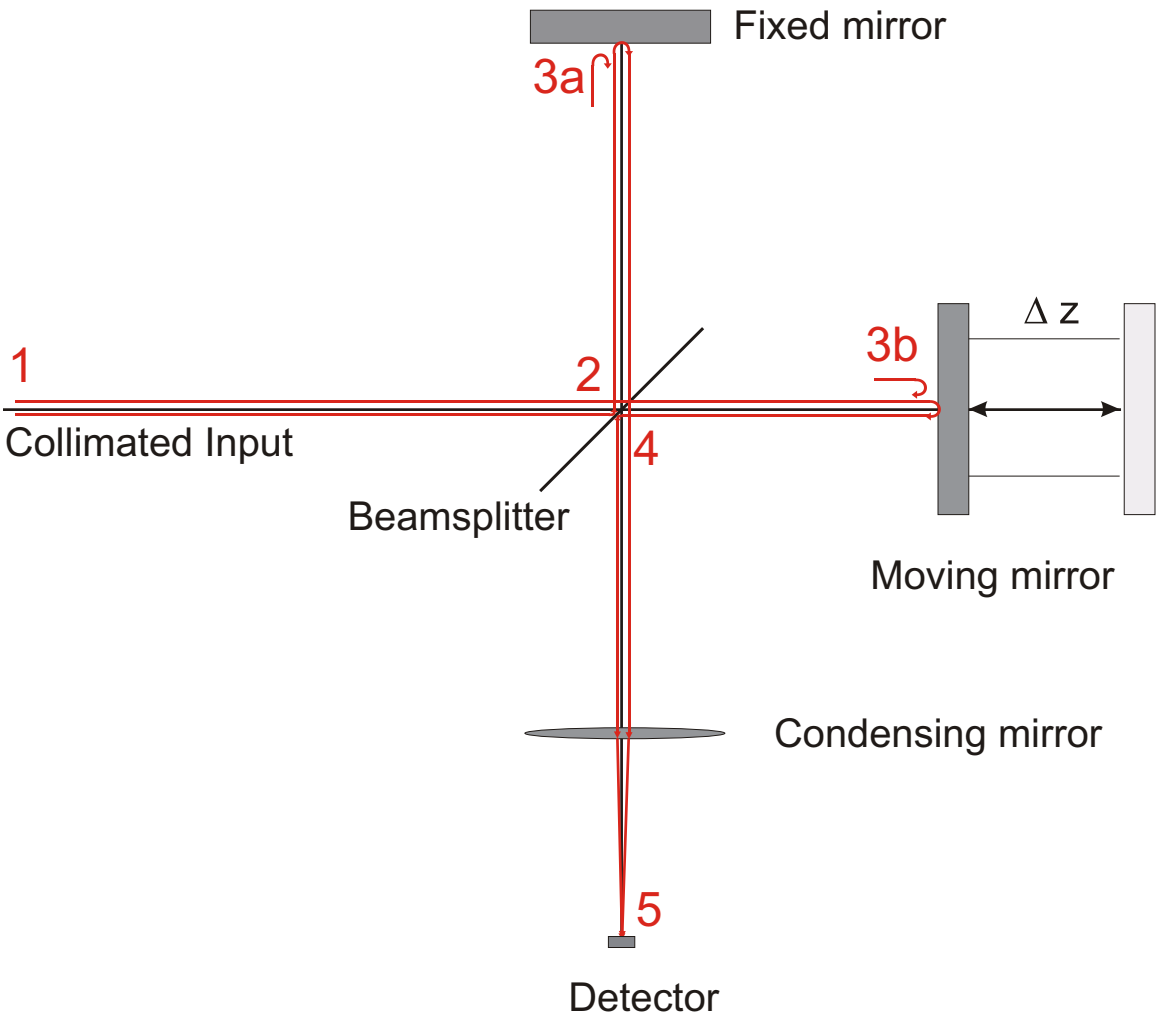

Figure 2.1: Diagram of a classical Michelson FTS[30].

All FTS interferometers have two input ports and two output ports. Each of the two ports on the Michelson interferometer is doubly occupied by both an input and an output port.

The relationship between the interferogram and spectrum is most easily explained using a monochromatic source; the extension to general spectral sources is straightforward.

2.6.1 Monochromatic sources

Consider a monochromatic beam of frequency σ_o entering the interferometer. The input beam is divided in two by the beamsplitter. The electric fields describing these two beams, starting in phase at the point just prior to the beamsplitter, can be written as:

$$\begin{aligned} E_1(z_1) &= E_0 e^{i\phi} r_m r_b t' e^{-i2\pi\sigma_o z_1} \\ E_2(z_2) &= E_0 e^{i\phi} r_m r_b t' e^{-i2\pi\sigma_o z_2}, \end{aligned} \tag{2.17}$$

where E_0 is the amplitude of the incident electromagnetic wave of angular frequency $\omega = 2\pi\sigma_o$, ϕ is the phase of the monochromatic wave at the beamsplitter, r_m is the amplitude reflection coefficient of each mirror, r_b is the amplitude reflection coefficient of the beamsplitter, t' is the amplitude transmission coefficient of the beamsplitter, and z_1 and z_2 are the lengths of the optical paths traveled by the two beams, respectively. The total electric field at the detector is given by adding the two individual electric fields from equation 2.17

$$E_T = E_1 + E_2 = E_0 e^{i\phi} r_m r_b t' (e^{-i2\pi\sigma_o z_1} + e^{-i2\pi\sigma_o z_2}). \tag{2.18}$$

The interferometer detector measures optical intensity rather than electric field. The total intensity measured at the detector is defined as the square of the magnitude of the total

electric field[38] and is given as follows:

$$I(z_1 - z_2) = |E_T|^2 = 2E_0^2 R_m R_b T(1 + \cos(2\pi\sigma_o(z_1 - z_2))), \tag{2.19}$$

where $R_m = r_m^2$ is the reflectance of the mirrors, $R_b = r_b^2$ is the reflectance of the beamsplitter, and $T = t'^2$ is the transmittance of the beamsplitter. In the case of an ideal interferometer, the beamsplitter reflects and transmits 50 % of the incident light and the interferogram can be expressed as:

$$I_0(z) \propto B(\sigma)(1 + \cos(2\pi\sigma_o z)), \tag{2.20}$$

where z is the OPD which was expressed as $z_1 - z_2$ in equation 2.19, $B(\sigma)$ is the spectrum ($E_0^2(\sigma) \propto B(\sigma)$), and σ_o is the frequency in wavenumbers (cm^{-1}) of the monochromatic source. The interferogram is seen to be composed of a constant (DC) term and a modulation term, which is given by the cosine function. In the monocromatic example, the spectrum $B(\sigma)$ is only nonzero at frequencies $\pm\sigma_o$ and is zero elsewhere.

2.6.2 Polychromatic/broad sources

When the spectral source contains more than one frequency, the resultant interferogram is the superposition of the interferograms for each frequency, i.e.

$$\begin{aligned} I_0(z) &\propto \int_{-\infty}^{+\infty} B(\sigma)(1 + \cos(2\pi\sigma z))d\sigma \\ &\propto \int_{-\infty}^{+\infty} B(\sigma)d\sigma + \int_{-\infty}^{+\infty} B(\sigma)\cos(2\pi\sigma z)d\sigma. \end{aligned} \tag{2.21}$$

It is customary to neglect the constant ($\int_{-\infty}^{+\infty} B(\sigma)d\sigma$) component and express the interferogram as:

$$I(z) \propto \int_{-\infty}^{+\infty} B(\sigma)\cos(2\pi\sigma z)d\sigma. \tag{2.22}$$

This is the cosine Fourier transform of the source spectrum $B(\sigma)$. The spectrum can be recovered by the inverse cosine Fourier transform of the interferogram:

$$B(\sigma) \propto \int_{-\infty}^{+\infty} I(z)\cos(2\pi\sigma z)dz. \tag{2.23}$$

As discussed earlier, when the inverse cosine Fourier transform of an interferogram is taken, in addition to the positive frequency spectrum $B(\sigma)$, the negative frequency spectrum $B(-\sigma)$ is produced.

The interferogram, $I(z)$, and spectrum, $B(\sigma)$, are Fourier transform pairs. $B(\sigma)$ and $I(z)$ are ideally real valued, allowing the interferogram and spectrum to be related using the cosine Fourier transform:

$$I(z) = 2\int_{0}^{+\infty} B(\sigma)cos(2\pi\sigma z)d\sigma, \tag{2.24}$$

and

$$B(\sigma) = 2\int_{0}^{+\infty} I(z)cos(2\pi\sigma z)dz. \tag{2.25}$$

$B(\sigma)$ is the spectrum formulated as a function of wavenumber, and $I(z)$ is the interferogram as a function of OPD. The even symmetry of $I(z)$ and the extension of $B(\sigma)$ to include negative frequencies ($B(-\sigma) = B(\sigma)$), allows the $2\int_{0}^{+\infty}$ integration limit on the cosine Fourier transforms in equations 2.24 and 2.25 to be interchangeable with the integration limit of $\int_{-\infty}^{+\infty}$:

$$I(z) = \int_{-\infty}^{+\infty} B(\sigma)cos(2\pi\sigma z)d\sigma, \tag{2.26}$$

and

$$B(\sigma) = \int_{-\infty}^{+\infty} I(z)cos(2\pi\sigma z)dz. \tag{2.27}$$

More generally, the interferogram and spectrum may be expressed using complex Fourier transforms[37]. The inverse complex Fourier transform is expressed as:

$$I(z) = \int_{-\infty}^{+\infty} B(\sigma) e^{+i2\pi\sigma z} d\sigma, \tag{2.28}$$

and the forward complex Fourier transform is expressed as:

$$B(\sigma) = \int_{-\infty}^{+\infty} I(z) e^{-i2\pi\sigma z} dz. \tag{2.29}$$

The complex Fourier transforms shown in equations 2.28 and 2.29 can be separated into sine and cosine Fourier transforms. The inverse transform is separated as

$$\begin{aligned} I(z) &= \int_{-\infty}^{+\infty} B(\sigma) e^{+i2\pi\sigma z} d\sigma \\ &= \int_{-\infty}^{+\infty} B(\sigma) cos(2\pi\sigma z) d\sigma \quad + i \int_{-\infty}^{+\infty} B(\sigma) sin(2\pi\sigma z) d\sigma, \end{aligned} \tag{2.30}$$

and the forward transform is separated as

$$\begin{aligned} B(\sigma) &= \int_{-\infty}^{+\infty} I(z) e^{-i2\pi\sigma z} dz \\ &= \int_{-\infty}^{+\infty} I(z) cos(2\pi\sigma z) dz \quad - i \int_{-\infty}^{+\infty} I(z) sin(2\pi\sigma z) dz. \end{aligned} \tag{2.31}$$

The even symmetry of $B(\sigma)$ can be exploited to express the interferogram as a cosine Fourier transform:

$$\begin{aligned} I(z) &= \int_{-\infty}^{+\infty} B(\sigma) cos(2\pi\sigma z) d\sigma \qquad + 0 \\ &= 2 \int_{0}^{+\infty} B(\sigma) cos(2\pi\sigma z) d\sigma. \end{aligned} \tag{2.32}$$

In the non-ideal (asymmetric) case the cosine (equation 2.25) and complex (equation 2.29) Fourier transforms are not equivalent. If uncorrected, the interferogram asymmetries lead to the introduction of phase errors in the spectrum. Phase correction is needed to re-symmetrize the interferogram and recover the correct spectrum. Phase correction will be discussed in detail in chapter 3.

2.7 FTS observing modes

There are two modes to record interferograms using an interferometer: step and integrate, and rapid-scan. The step and integrate mode involves stepping precise amounts of OPD and waiting for a prescribed period of time for the optical detector to integrate signal. Step and integrate mode requires some form of signal modulation such as a chopper combined with a lock-in amplifier to separate the signal from the DC/low frequency noise. Improvements in signal-to-noise ratio (S/N) are obtained through increasing the integration time per step.

Alternatively, rapid-scan mode, developed by Mertz[53, 54], involves moving the FTS translation stage at constant velocity and sampling both the optical signal and stage position in uniform increments of OPD. The mirror velocity can be selected such that the interferogram fringes provide signal modulation[37]. The ac modulated signal can be processed for spectral filtering and electronic noise reduction before the spectrum is computed. S/N improvements are found through repeating scans and averaging either interferograms or spectra, rather than slowing down the mirror velocity which would reduce the fringe modulation.

For a Michelson interferometer in rapid-scan mode, the OPD, z, as a function of time, t, and optical speed, v, is given by:

$$z = vt. \tag{2.33}$$

Equation 2.20 reveals that the angular frequency relating to any particular spectral contribution to the interferogram, i.e. σ_o, is derived from the term $\cos(\omega z) = \cos(2\pi\sigma_o z)$. Since the mirror is moving in time, the electrical detector signal modulation is observed as a func-

tion of time rather than position. Thus, the observed interferogram electrical oscillation frequency will be related to both the moving mirror velocity and the maximum spectral frequency (see equation 2.43). In the rapid scan mode an external source of signal modulation (e.g. a chopper) is not required, therefore the entire signal is exposed to the detector at all times. Thus, for a given scan time, T, the detector is exposed to the interference signal for time T in rapid scan mode while the detector is only exposed to the interference signal for a time $\frac{T}{2}$ in step-and-integrate mode. Rapid-scanning measurements are more resilient to source fluctuations than step-and-integrate measurements as individual interferograms are recorded in a short time interval. Individual interferograms deemed unacceptable (e.g. a scan encountering a cosmic ray event) can be discarded without affecting the remainder of the measurement, whereas a corrupted integration step in step and integrate data collection affects the entire measured spectrum.

2.8 The Jacquinot advantage

The throughput of an FTS is defined as the product of the area of the input light beam A (m^2) and the solid angle Ω (sr) contained within the beam; this quantity is also known as the étendue or light-grasp. The controlling factor for the throughput is usually the most expensive component of the spectrometer; in the case of an FTS this is typically the beamsplitter. All interferometers possessing circular symmetry (eg. FTS or Fabry Perot interferometers) have significantly higher throughput or optical efficiency, compared with dispersive spectrometers such as grating spectrometers, where the real component of the throughput is determined by the narrow entrance and exit slits. The high throughput of

the FTS is known as the Jacquinot advantage[44]. As will be shown in section 2.10.4, while in principle one can increase the throughput by increasing the divergence angle within the FTS this results in a natural apodization of the interferogram, which limits the maximum attainable resolution. Hence, there is a trade-off between attainable resolution and signal intensity.

2.9 The Fellgett advantage

The multiplex advantage[43] of an FTS, also known as the Fellgett advantage, is due to the exposure of an interferometer to all spectral components of a signal at all times. To illustrate the Fellgett advantage an example comparing an FTS with a dispersive spectrometer is given. In a dispersive spectrometer[30] only a narrow range of wavelengths are measured at a given instant. By comparison, in an FTS all source wavelengths are incident on the detector at all times. This leads to a multiplex advantage also known as the Fellgett advantage.

Suppose a spectrum is measured between σ_1 and σ_2 with a resolution $\delta\sigma$ (cm^{-1}). The number of spectral elements, M, in the band is given by

$$M = (\sigma_2 - \sigma_1)/\delta\sigma. \tag{2.34}$$

If a grating spectrometer is used then each small band of width $\delta\sigma$ can be observed for a time $\frac{T}{M}$ where T is the total time required to scan the full spectrum. The integrated signal received in a small band $\delta\sigma$ is proportional to $\frac{T}{M}$. If the noise is random and does not depend on the signal, then the signal noise should be proportional to $\sqrt{\frac{T}{M}}$. Therefore, the

S/N for a grating spectrometer is [37]:

$$S/N_G \propto \sqrt{\frac{T}{M}}. \tag{2.35}$$

An FTS measures all wavelengths at all times. Therefore the integrated signal in a small band $\delta\sigma$ is proportional to T (rather than $\frac{T}{M}$) and the signal noise is proportional to $\sqrt{T}$. Thus, for an interferometer, the S/N is[37]:

$$S/N_I \propto \sqrt{T}. \tag{2.36}$$

If the grating and FTS spectrometers have identical (or at least comparable) throughput then the ratio of the S/N for the two instruments can be written as:

$$\frac{S/N_I}{S/N_G} = \sqrt{M}. \tag{2.37}$$

Since M is the number of spectral elements of width $\delta\sigma$, equation 2.37 indicates that the interferometer has a much higher S/N than a grating spectrometer. Moreover, it should be noted that due to the narrow entrance and exit slits of a grating spectrometre[30], the throughput of an FTS is typically two orders of magnitude larger than a grating spectrometer, which leads to an even greater increase in S/N.

Advances in detector array technology allow grating spectrometers to observe entire spectral ranges simultaneously; however, the FTS can use the same detector arrays to simultaneously observe many spatial components of the source (i.e. imaging FTS (iFTS)) so the gain is retained [37].

The Multiplex advantage is lost when the signal noise is proportional to the square root of the source intensity (i.e. photon noise) as the ratio of FTS and grating spectrometer S/N approaches unity. The Jacquinot advantage (section 2.8) is not lost during photon

noise limited measurements, however, so the FTS still holds an advantage over the grating spectrometer.

2.10 FTS design issues

The analysis presented in section 2.6 for determining the spectrum from the interferogram involve integrating the OPD from $-\infty$ to $+\infty$. In practice, interferograms cannot be measured out to infinity in either direction of OPD, but to a finite maximum OPD, L. As a result, the spectral resolution achieved is not infinite, but rather finite and is given by:

$$\Delta\sigma = \frac{1}{2L}, \tag{2.38}$$

where L is the maximum optical path difference and $\Delta\sigma$ is the spacing between elements in the spectrum. Thus the resolution of an FTS interferometer is variable depending on the OPD length L selected for an interferogram. A consequence of the finite truncation of the interferogram is a sinc function convolved across the spectrum in the reciprocal Fourier domain[37]. Thus, FTS interferometer spectra have an inherent sinc instrumental line shape (ILS).

2.10.1 Phase

Asymmetries in interferograms cause the calculated spectrum to be complex valued. Thus, interferogram asymmetries are observed in spectra as phase. The determination of the spectral phase, $\phi(\sigma)$, is as follows:

$$\phi(\sigma) = \arctan(\frac{B_i(\sigma)}{B_r(\sigma)}), \tag{2.39}$$

where B_r is the real component of the spectrum and B_i is the imaginary component of the spectrum. FTS instrument design and data processing must account for asymmetries in the interferogram and will be discussed in greater detail in chapter 3.

2.10.2 Noise

Optical noise consists of photon noise and source noise. Photon noise is due to statistical fluctuations in the rate of arrival of photons. If n photons are measured in a given time period, the photon noise level is proportional to $\sqrt{n}$. Source noise arises from periodic and random variations in source intensity over time. The random component of source noise typically varies as $1/f$ in the frequency domain[38].

Electrical noise sources can be categorized as Johnson noise, phonon noise, shot noise, and flicker noise[55]. Johnson noise, also known as white noise, has a flat spectral profile. Phonon noise is produced by vibrations and temperature fluctuations in the detectors (e.g. bolometers) and the thermal connection to the detector heat sinks[55, 56]. Shot noise results from time-dependent fluctuations in electrical current caused by the quantized electron charge, and is well known to occur in solid-state devices such as tunnel junctions, Schottky barrier diodes, and p-n junctions. Flicker noise has a $1/f$ frequency profile, similar to random optical source noise. The shot and flicker noise produced in the detector contacts is difficult to model, and is measured as excess noise in the detector signal.

Ideally, an FTS is designed such that all noise is reduced to the point where photon noise dominates through alignment and proper choice of detectors, optics, and readout electronics. Noise should affect the real and imaginary domains of the spectrum equally. Therefore, the noise found in the real portion of the spectrum is less than that in the entire

(i.e. complex) spectrum. Random noise levels are reduced through improving interferometer stage metrology and signal S/N. The random noise contribution to the interferogram can never be completely removed but can be minimized through FTS design and data processing techniques (see chapter 5).

2.10.3 Nyquist and Sampling

The Nyquist sampling theorem[57, 58] states that a signal may be perfectly reconstructed if the data sampling frequency is twice that of the highest spectral content of the signal being sampled. Other conditions on the Nyquist sampling theorem are similar to convergence requirements in a Fourier series and are given in section 2.3.1. For the sampling of an interferogram, the OPD sampling interval must satisfy the following criteria:

$$\Delta z \leq \frac{1}{2\sigma_{band}}, \tag{2.40}$$

where Δz is in cm and σ_{band} is the spectral bandwidth of the signal (in cm^{-1}). For spectra including zero frequency as the lowest portion of the band, σ_{band} is equivalent to σ_{max}, the highest spectral frequency component (cm^{-1}). Inversely, the maximum observable or Nyquist frequency, σ_{nq}[1] in cm^{-1}, is given in terms of interferogram OPD sampling interval by the relation:

$$\sigma_{nq} = \frac{1}{2\Delta z} \qquad cm^{-1}, \tag{2.41}$$

where Δz is the optical sampling interval in cm.

In essence, an interferometer is simply an effective method of bringing the unobservable high frequencies of light down to observable acoustic frequencies by exploiting the

[1]The distinction between σ_{nq} and σ_{max} is this: σ_{nq} is the highest frequency that the spectrometer is capable of observing while σ_{max} is the highest frequency (or band if zero frequency is not required) that is actually present in the spectrum.

principle of interference. Assuming that the spectrum is not under-sampled (i.e. no aliasing) then, for a rapid scan FTS, the highest modulation frequency found in an interferogram, ν_{max} (Hz), is related to the highest spectral frequency, σ_{max}, as follows:

$$\nu_{max} = v_{OPD}\sigma_{max} \qquad Hz, \tag{2.42}$$

where v_{OPD} is the speed of the translation stage in optical path difference.

For example, an optical source of 0.1 cm wavelength ($\lambda = 0.1$ cm, $\sigma = 10\text{cm}^{-1}$) has a frequency of 300 GHz. A Michelson interferometer with a translation stage moving at 1 cm_{opd}/s will modulate the 300 GHz oscillation down to 10 Hz (equation 2.42). This is a frequency reduction on the order of 10^{11}.

It is common practice to measure the interferogram in equal increments of optical path difference, which allows use of the FFT algorithm. The FFT algorithm[2] computes the discrete Fourier transform of N data points on the order of $N \log_2 N$, as compared to a time scale on the order of N^2 for the discrete Fourier transform algorithm. The FFT algorithm requires at least one unique data point at ZPD(see figure 3.2). Failure to sample the exact position of ZPD correctly results in phase errors in the spectrum which will be discussed in chapter 3.

Stage Velocity

In rapid-scanning observation mode, interferometer mirror stage velocity is limited by the detector roll-off frequency[59]. For a Michelson interferometer, the relationship between the maximum spectral frequency (σ_{max}), the stage velocity, and the detector roll-

off frequency (ν_{max} in Hz) is given by

$$\sigma_{max} = \frac{\nu_{max}}{v} \qquad (cm)^{-1} \tag{2.43}$$

where v is the optical linear stage velocity in cm/s.

2.10.4 Natural apodization

In the case of a point source located at a focus of a lens which feeds an interferometer, the resulting collimated beam has no divergence and thus the overlap of the recombined beams from the interferometer is independent of OPD. In reality, however, all interferograms suffer from some degree of distortion due to the divergence of radiation within the interferometer. In a real interferometer the entrance aperture has a finite size which means that a beam entering the interferometer is divergent and the overlap between the recombined beams depends upon OPD; this leads to the phenomenon known as natural apodization.

Consider light entering an interferometer's entrance aperture at an angle α away from the optical axis (see figure 2.2). Where the on-axis OPD is simply z, the off-axis OPD is $z\cos(\alpha)$ instead. The resulting interferogram intensity is determined by integrating over the solid angle Ω. For a monochromatic source, the interferogram is determined as follows:

$$\begin{aligned} I(z) &\approx \int_0^{\Omega} \cos(2\pi\sigma_o z[1-\frac{\alpha^2}{2}])d\Omega' \\ &\approx \int_0^{\Omega} \cos(2\pi\sigma_o z[1-\frac{\Omega'}{2\pi}])d\Omega' \\ &\approx \Omega sinc(\frac{\sigma_o z\Omega}{2\pi})\cos(2\pi\sigma_o z(1-\frac{\Omega}{4\pi})). \end{aligned} \tag{2.44}$$

Two simplifications are incorporated into the above expression. Firstly, the small angle

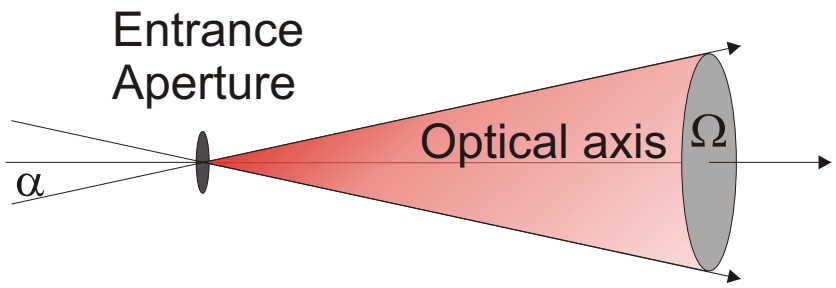

Figure 2.2: Diagram of off-axis light due to a finite sized entrance aperture on an FTS.

approximation (i.e. $\cos(\alpha) \approx 1 - \frac{\alpha^2}{2}$) and secondly, a circular aperture at the focus of a collimating mirror has solid angle $\Omega = \pi\alpha^2$. Equation 2.44 shows that the measured interferogram is different from the ideal interferogram (equation 2.26 change in the cosine term as well as a multiplication by a sinc function.

There are two effects on the interferogram/spectrum caused by the finite entrance aperture of a non-ideal interferometer:

- the interferogram envelope is multiplied by a sinc function, and
- there is both an OPD and wavenumber scale change.

The scale change in OPD and wavenumber can be expressed as $z' = z(1 - \frac{\Omega}{4\pi})$ and $\sigma' = \sigma(1 - \frac{\Omega}{4\pi})$.

The multiplication of the interferogram by a sinc function is equivalent to convolving the spectrum with a rectangular function. For a monochromatic source at frequency σ_o, the spectral line appears to be at σ_o for the on-axis signal, but for the most oblique rays with the shortest OPD ($z' = z\cos(\alpha)$) the spectral line will be shifted to $\sigma_o(1 - \frac{\Omega}{2\pi})$. Thus the observed line will be centred at $\sigma_o(1 - \frac{\Omega}{4\pi})$ and will have a width increase of $\frac{\Omega\sigma_o}{2\pi}$.

Therefore, spectral resolution greater than $\frac{\Omega\sigma_o}{2\pi}$ cannot be achieved as the rectangular convolution has broadened all spectral features. Resolving power of an interferometer is given as:

$$R = \frac{\sigma}{\Delta\sigma}. \tag{2.45}$$

The limit on spectral resolution can be related to resolving power as follows:

$$\begin{aligned} R &\leq \frac{\sigma}{\frac{\sigma\Omega}{2\pi}} \\ R &\leq \frac{2\pi}{\Omega}, \end{aligned} \tag{2.46}$$

where the inequality above is known as the Jacquinot criterion[38]. The Jacquinot criterion prescribes an upper limit on both the resolution of an interferometer and the size of the entrance aperture (and hence the maximum off-axis angle).

There is also a component of natural apodization due to the finite scan range of actual FTS interferometers. Essentially, an infinite interferogram is multiplied by a finite rectangular function of width $\pm L$. This is equivalent to convolving the spectrum with a sinc function (with full width at half maximum (FWHM) $\sim \frac{1.207}{L}$). Thus the natural ILS of an FTS with a collimated input is a sinc function. The natural ILS of an FTS without a collimated input is a sinc function convolved with a rectangular function.

2.11 Conclusions

This chapter has introduced the mathematics behind the operation of an FTS. The classical Michelson FTS design was introduced and the Jacquinot and Fellgett advantages

of the FTS have been explored. Limitations of the FTS have also been explored in areas such as natural apodization, sampling, noise, symmetry, resolution, finite travel, and finite aperture size. The FTS, with its simple optomechanical design, broad spectral coverage, high throughput and variable resolution make it a choice spectrometer for measurements of weak astronomical signals at submillimetre wavelengths.

Chapter 3

Phase Correction

3.1 Overview

In Fourier transform spectroscopy, measured interferograms are likely to contain phase errors. When operating an FTS in single-sided operation (section 3.2), as is the case for the Herschel SPIRE spectrometer, it is necessary to phase correct the interferograms to obtain accurate spectra. The Herschel SPIRE spectrometer contains two beam-splitters; both of which are expected to have a non-linear, perhaps unique, phase response. This chapter will discuss sources of phase errors and two phase correction methods introduced by Mertz[60] and Forman[61].

3.2 Terminology

There is considerable discrepancy in the literature regarding the terminology associated with FTS interferograms. The terminology used in this work is defined here for

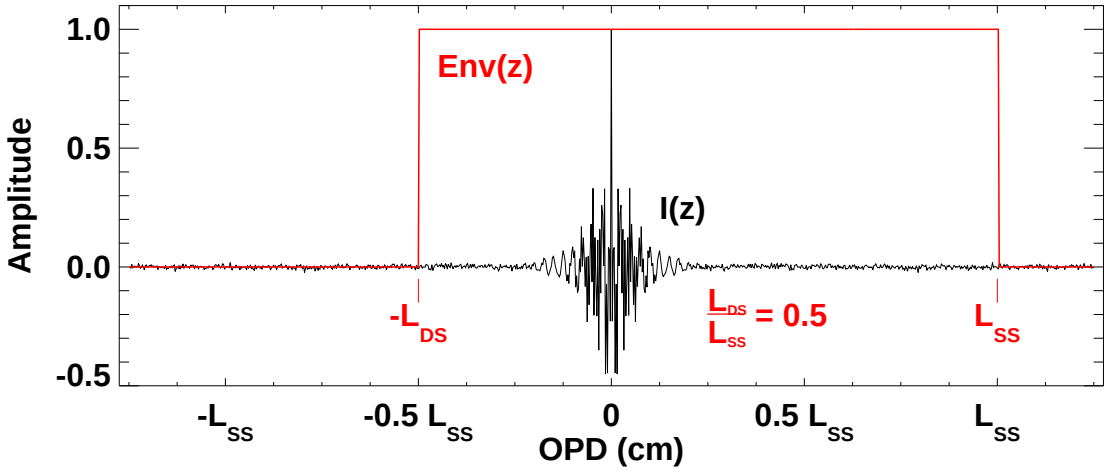

Figure 3.1: The interferogram of a spectrum containing a broad Gaussian emission line on which are superimposed several Gaussian absorption features and a random noise component. Also shown is the envelope function, $Env(z)$, in red. If $L_{DS} = 0$ then the resulting interferogram is one-sided, if $\frac{L_{DS}}{L_{SS}} = 1$ then the interferogram is double-sided, and if $\frac{L_{DS}}{L_{SS}} < 1$ then the interferogram is single-sided.

clarity, and will be used extensively throughout this and the remaining chapters. Unless explicitly stated, all values with units of distance are stated in terms of optical path difference. Figure 3.1 illustrates an interferogram of a spectrum containing a broad Gaussian emission line on which are superimposed several Gaussian absorption features. The figure is used to define the terms double-sided, single-sided, one-sided, and envelope function.

An interferogram, although theoretically of infinite length, is recorded over a finite range of optical path difference determined by the length of the translation stage of the FTS instrument (see figure 2.1). The term $I_\infty(z)$ is used to denote a theoretical interferogram with values over the optical path range $z \in (-\infty, +\infty)$. An actual interferogram can be considered to be the product of $I_\infty(z)$ and an envelope function, $Env(z)$:

$$I(z) = I_\infty(z) \times Env(z). \tag{3.1}$$

The value of the envelope function over the interval $z \in [-L_{DS}, L_{SS}]$ is as follows:

$$Env(z) = \begin{cases} 1 & z \in [-L_{DS}, L_{SS}] \\ 0 & \text{elsewhere.} \end{cases} \tag{3.2}$$

The interval $[-L_{DS}, L_{SS}]$, with $z = 0$ marking the location of ZPD, defines the finite interval over which the interferogram is actually measured in practice. To distinguish between the terms one-sided, single-sided, and double-sided the ratio of $\frac{L_{DS}}{L_{SS}}$ is used. The interferogram is one-sided for

$$\frac{L_{DS}}{L_{SS}} = 0, \tag{3.3}$$

single-sided for

$$0 < \frac{L_{DS}}{L_{SS}} < 1, \tag{3.4}$$

and double-sided for

$$\frac{L_{DS}}{L_{SS}} = 1. \tag{3.5}$$

The FFT algorithm[2] requires both positive and negative OPD interferogram data at the same resolution to calculate a complex Fourier transform. A one-sided interferogram known to be symmetric may, in principle, be *butterflied* in order to provide the FFT algorithm with the required negative OPD information. The process of butterflying an interferogram involves setting the interferogram values of negative OPD equal to the corresponding positive OPD values. This is only accurate if the interferogram is of even symmetry, as is ideally the case:

$$I(-z) = I(z). \tag{3.6}$$

The resulting spectrum of the butterflied, one-sided interferogram will have the same resolution as a double-sided interferogram of the same length (i.e. $\frac{L_{DS}}{L_{SS}} = 1$). This, of course,

neglects any phase errors propagated by the butterflying process which ignores any asymmetry in the original single-sided interferogram.

3.3 Introduction

The finite amount of stage travel in FTS instruments may be allocated towards two reciprocal applications. Stage travel may be used for higher spectral resolution (one-sided interferogram) or it may be used for providing phase information (double-sided interferogram). The idea of measuring a one-sided interferogram was first introduced by J. Connes in 1970[62]. In many cases, the phase information provided by a double-sided interferogram may be highly over-resolved as phase is typically slowly varying[54, 61, 63]. An ideal interferogram will contain identical information on both sides of the ZPD position. Theoretically, therefore, the spectrum can be uniquely recovered with an interferogram starting at ZPD (one-sided interferogram). However, in practice, a single-sided interferogram is measured in such a way that at least a small amount in the negative OPD region is recorded in order to characterize the phase. This phase information can then be used to correct the asymmetry in the high resolution one-sided interferogram. For a translation stage of fixed length, this leads to a trade-off between the length of the double-sided interferogram used to determine the phase information, and the one-sided interferogram used to achieve higher spectral resolution.

There are several causes of phase errors in Fourier transform spectrometers. The most common type of phase error arises from not precisely sampling the ZPD position of the interferogram, thereby producing a linear phase error in the spectral domain. Nonlinear

phase errors can arise from such things as: dispersion in the beam-splitter/compensator, electronic amplifier frequency response, detector time constants, and misalignment in mirrors. Random phase errors may be the result of: noise in the optical/electronic signal, and variations in the position and velocity of the translation stage. If left uncorrected, upon Fourier transformation the resulting phase errors will introduce artifacts into the final spectrum[39].

Phase contributions can be categorized as systematic, variable, and random. Systematic effects can in principle be calibrated and removed in post-processing. Variable and random phase require attention at the level of an individual interferogram. The following sections discuss phase correction as a technique used to correct for the asymmetry in single-sided interferograms.

3.4 Theory

The above contributions to phase, $\phi(\sigma)$, can be combined and expressed within the inverse complex Fourier transform, resulting in an asymmetric interferogram:

$$I_{asymmetric}(z) = \int_{-\infty}^{+\infty} B(\sigma) e^{i\phi(\sigma)} e^{+2\pi\sigma z} d\sigma. \tag{3.7}$$

The Fourier transform of a real, non-symmetric function results in a complex function with even and odd symmetry for the real and imaginary components, respectively[31]. An interferogram with spectral phase errors will be real but non-symmetric. The complex Fourier transform (equation 2.29) of an interferogram with asymmetry/phase errors will

result in a complex valued spectrum:

$$\begin{aligned}\int_{-\infty}^{+\infty} I_{asymmetric}(z)e^{-i2\pi\sigma z}dz &= B(\sigma)e^{i\phi(\sigma)} \\ &= B_r(\sigma) + iB_i(\sigma),\end{aligned} \tag{3.8}$$

where $B_r(\sigma)$ and $B_i(\sigma)$ represent the resultant real and imaginary components of the spectrum, respectively. The real and imaginary components are products of the actual spectrum, and a phase term, as shown below:

$$B_r(\sigma) = B(\sigma)cos(\phi(\sigma)) = \int_{-\infty}^{+\infty} I_{asymmetric}(z)cos(2\pi\sigma z)dz, \tag{3.9}$$

$$iB_i(\sigma) = iB(\sigma)sin(\phi(\sigma)) = -i\int_{-\infty}^{+\infty} I_{asymmetric}(z)sin(2\pi\sigma z)dz. \tag{3.10}$$

Due to the asymmetry of $I_{asymmetric}(z)$ (equation 3.7), the positive ($\int_0^{+\infty}$) and negative ($\int_{-\infty}^0$) frequency components of the sine Fourier transform do not cancel out as they do for the ideal, symmetric interferogram (equation 2.32). As a consequence of this, butterflying a one-sided interferogram without phase correction will result in spectral errors.

Ignoring any noise contributions, the original spectrum from an asymmetric interferogram may be recovered by taking the absolute value of the real and imaginary components (equations 3.9 & 3.10):

$$B(\sigma) = |B(\sigma)| = [B_r(\sigma)^2 + B_i(\sigma)^2]^{\frac{1}{2}}. \tag{3.11}$$

Two problems are associated with the absolute value method. Firstly, the interferogram needs to be double sided so that the complex Fourier transform may be taken (equation 2.29 rather than equation 2.25). Secondly, we have so far assumed that all of the detector output is modulated source radiation but there will also be noise included in the signal (see sections 2.10.2 & 3.5.4). Taking the absolute value of the real and imaginary components

of the spectrum brings all of the noise out of the imaginary domain into the real. This results in an undesirable increase in the spectral noise level by a factor of $\sqrt{2}$. Moreover, a positive valued noise floor is introduced due to the negative noise being inverted to become positive[64].

Any signal can be expressed as the sum of an even and an odd function[31]. Equation 3.12 shows the asymmetric interferogram separated into its constituent even and odd components:

$$I_{asymmetric}(z) = I_{even}(z) + I_{odd}(z). \tag{3.12}$$

Ideally, a single-sided interferogram is symmetric. This assumed symmetry allows both positive and negative OPD interferogram values to be known even though up to one half of the interferogram need not be measured. This is equivalent to performing the cosine Fourier transform (equation 2.25). However, in practice, when $I_{asymmetric}(z)$ is assumed to be symmetric and the cosine Fourier transform is performed, spectral errors in lineshape, line centre, amplitude, etc. are introduced. Equation 3.13 illustrates the output of the cosine Fourier transform (equation 2.25) when it is used on an asymmetric interferogram:

$$\begin{aligned} 2\int_0^{+\infty} I_{asymmetric}(z)cos(2\pi\sigma z)dz &= 2\int_0^{\infty}[I_{even}(z) + I_{odd}(z)]cos(2\pi\sigma z)dz \\ &= 2\int_0^{\infty} I_{even}(z)cos(2\pi\sigma z)dz \\ &\quad +2\int_0^{\infty} I_{odd}(z)cos(2\pi\sigma z)dz \\ &= B(\sigma)cos(\phi(\sigma)) + 2\int_0^{\infty} I_{odd}(z)cos(2\pi\sigma z)dz \\ &\neq B(\sigma) \end{aligned} \tag{3.13}$$

The correct spectrum ($B(\sigma)$) is not only multiplied by a phase dependent component ($cos(\phi(\sigma))$), but there is another term ($2\int_0^{\infty} I_{odd}(z)cos(2\pi\sigma z)dz$) added to the spectrum.

The added term is related to the odd-symmetry component of the interferogram, $I_{odd}(z)$. Thus, the degree of spectral degradation caused by the non-zero phase depends strongly on the nature of the asymmetry of the interferogram itself. The difference between $B(\sigma)$ and the output of equation 3.13 is as follows:

$$\begin{aligned} B(\sigma) - 2\int_0^{+\infty} I_{asymmetric}(z)\cos(2\pi\sigma z)dz \quad &= \quad B(\sigma)[1-\cos(\phi(\sigma))] \\ &\quad -2\int_0^{+\infty} I_{odd}(z)\cos(2\pi\sigma z)dz \\ \text{and, using the approximation described below,} \quad &\approx \quad -2\int_0^{+\infty} I_{odd}(z)\cos(2\pi\sigma z)dz. \end{aligned} \tag{3.14}$$

The approximation used in equation 3.14 is based on the small angle approximation and is as follows:

$$\cos(\phi(\sigma)) \approx \sqrt{1-\phi(\sigma)^2} \approx 1. \tag{3.15}$$

It is important to note that, although $\int_{-\infty}^{+\infty} I_{odd}(z)cos(2\pi\sigma z)dz = 0$ due to orthogonality, the last term in equation 3.14, $2\int_0^{\infty} I_{odd}(z)cos(2\pi\sigma z)dz \neq \int_{-\infty}^{+\infty} I_{odd}(z)cos(2\pi\sigma z)dz$ and is thus non-zero. If the phase is small, allowing the small angle approximation, then the difference between $B(\sigma)$ and the spectrum produced by equation 3.13 is limited to that related to $I_{odd}(z)$. Small phase implies that $I_{odd}(z)$ will also be small, and thus the resulting spectral errors may be negligible. If this is not the case, however, then phase correction is essential to recover accurate spectra.

3.5 Phase Errors

In practice, the total phase error can be considered to be the summation of several components:

$$\phi(\sigma) = \phi_{DC} + \phi_{Lin}(\sigma) + \phi_{NL}(\sigma) + \phi_R(\sigma). \tag{3.16}$$

There can exist a DC phase offset, ϕ_{DC}, due to sources such as inverting amplifiers and high pass filters in the detector readout electronics. A linear phase error, $\phi_{Lin}(\sigma)$, arises from not precisely sampling the location of ZPD. A nonlinear phase component, $\phi_{NL}(\sigma)$, may arise from electronic signal processing or any nonlinear optics such as a dispersive beamsplitter or optical filter. When there is a quadratic or higher order σ term in the phase then the interferogram can be described as *chirped* and a point of stationary phase (equation 3.19) will not exist[39]. In general there will also be a random component, $\phi_R(\sigma)$ attributable to noise. These phase components will be discussed in detail.

The extension of phase into the negative frequencies utilizes the odd-symmetry relation:

$$\phi(-\sigma) = -\phi(\sigma), \tag{3.17}$$

unlike the extension of the spectrum into negative frequencies which utilizes the even-symmetry relation (equation 3.6). Sheahen[65] discusses numerical errors resulting from a phase discontinuity at $\sigma = 0$ cm^{-1} if $\phi(0) \neq 0$. This discontinuity involves the limits:

$$\begin{aligned} \lim \phi(\sigma)_{\sigma \to 0^-} &= -\phi(0), \qquad \text{and} \\ \lim \phi(\sigma)_{\sigma \to 0^+} &= \phi(0). \end{aligned} \tag{3.18}$$

Discontinuities in one domain have effects in the reciprocal domain and will be discussed in greater detail in section 4.4.

3.5.1 Phase offset - ϕ_{DC}

There is typically electronic amplification in the data collection system of FTS detectors. In addition to the 180^o phase shift of an inverting amplifier, electronic amplifiers (both inverting and non-inverting) typically have a complex frequency response. The same holds true for electrical filters which are typically used in conjunction with electronic amplifiers[59]. Ideal in-band phase/amplitude response for an amplifier/filter is flat. Chebyshev type filters typically have a flat phase response at the cost of a rounded amplitude response. This flat phase response is ideal for reducing electronics-based interferogram phase errors. Conversely, Butterworth and Bessel type electronic filters have a flat amplitude response but a nonlinear phase response. Electronic filter and amplifier behavior is well understood[66, 59] and resulting phase errors can be minimized.

3.5.2 Linear phase errors - ϕ_{Lin}

Linear phase errors arise from incorrect sampling of the interferogram ZPD location. The interferogram OPD shift property is useful in explaining linear phase error and is illustrated in table B.1, where the variable z_o is used to express the point of stationary phase (ideally ZPD). If there is an error in the location of ZPD, or ZPD has not been sampled, then there will be a linear phase in the spectrum. A symmetric, continuous interferogram may be sampled such that the resultant discreet interferogram will not be symmetric. Two unique sampling conditions will ensure that a discreet interferogram does not lose its symmetry. As is outlined in figure 3.2, the sampled interferogram will be symmetric if the ZPD point is sampled exactly, or if the ZPD point lies exactly between two sample points. The

former sampling condition will have no linear phase error while the latter, although still symmetric, will have linear phase error ($\phi(\sigma_{nq}) = \pi$)[1]. The latter symmetric mode is called even-extension symmetry[67] and contains the same information with one less data point as the other symmetric sampling mode. This memory savings may seem small but potentially allows significant memory/computation savings for large interferogram arrays such as those generated by imaging FTS, e.g. SPIRE[9] and SCUBA-2[27].

If the ZPD is not measured exactly on a sampled data point, then the spectral phase will have a linear variation with frequency. Connes[39, 68] discussed the effect of an error in the choice of the ZPD point on the instrumental line shape. Connes' considers only linear phase error due to ZPD missampling. The linear form of the phase is related to the point of stationary phase as follows:

$$\phi_{Lin}(\sigma) = 2\pi z_o \sigma. \tag{3.19}$$

If ϕ_{Lin} varies linearly with wavenumber, then the interferogram is symmetric about the point where $z = z_o$ which is known as the point of stationary phase.

Unless an accurate fiducial marker is used to determine ZPD, such as that produced by an interferogram of a broadband optical source, a linear phase error will generally be present in all measured interferograms and should be removed in order to minimize spectral errors. The extent of this error depends on the translation stage sampling interval, Δz. A finer sampling interval will allow the interferogram to be sampled closer to ZPD and thus reduce the magnitude of the linear phase error. Figure 3.3 illustrates the sloped phase resulting from a linear sampling shift in the interferogram. Correcting an interferogram for

[1] σ_{nq} is the Nyquist frequency

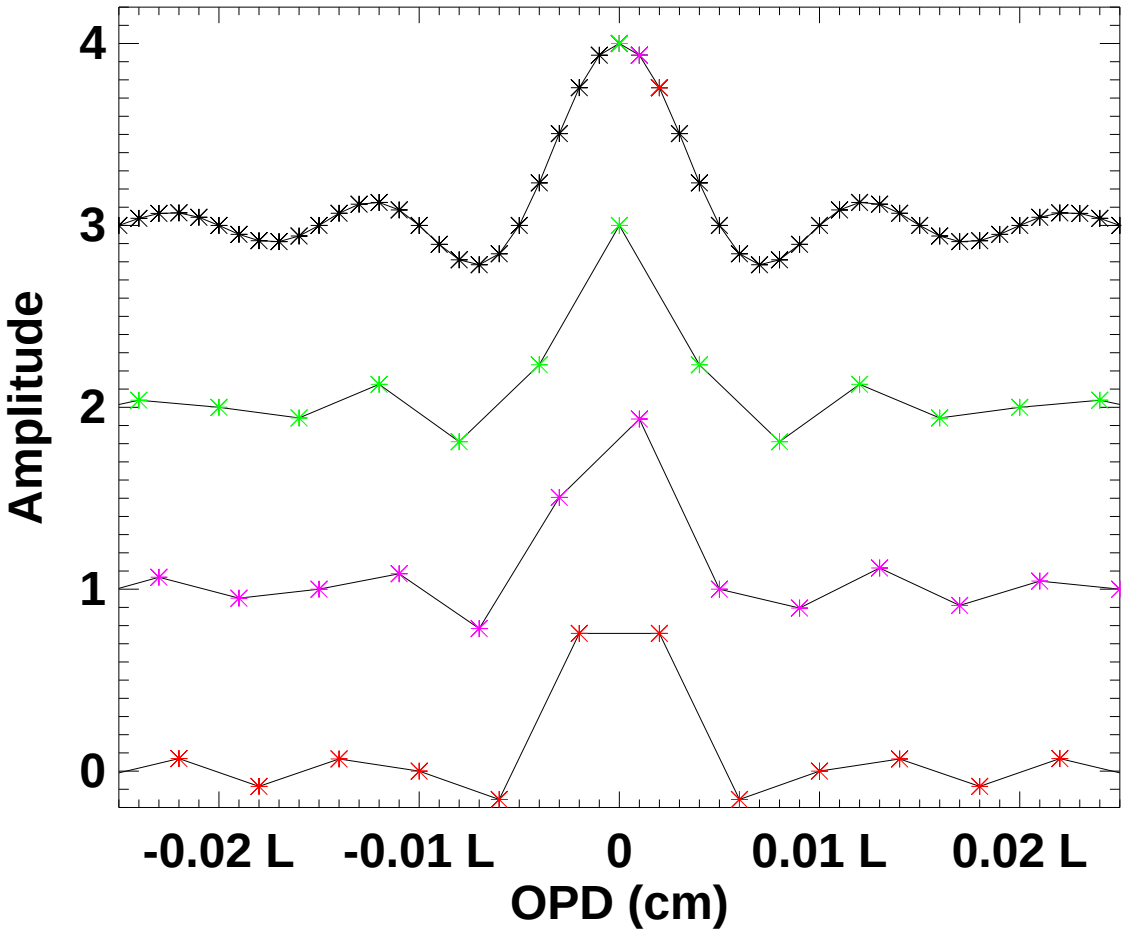

Figure 3.2: Linear shifts of the uniform sampling of an interferogram. The top function shows the original interferogram prior to sub-sampling (4x). The function immediately below (green) shows a symmetric sampling scheme including ZPD. Below that (purple) is an asymmetric sampling of the originally symmetric interferogram. The bottom (red) shows the even-extension symmetric sampling (ZPD is exactly between two sample points). The graphs have been offset for clarity.

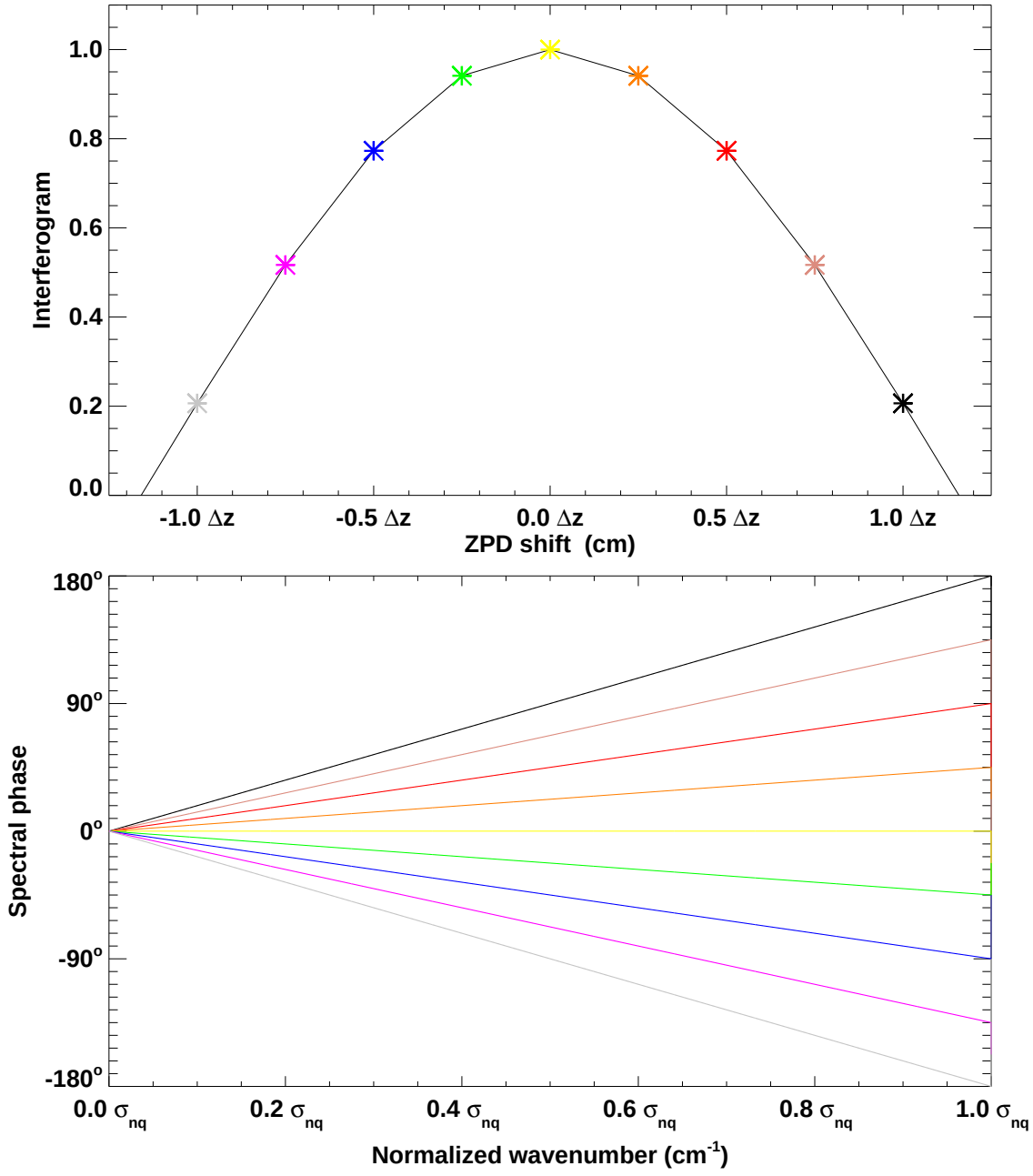

Figure 3.3: The resultant linear phase error due to ZPD sampling shift. In each case the interferogram is sampled uniformly, however the location of the data point closest to ZPD is shifted, resulting in a linear phase with slope proportional to the corresponding ZPD shift. A shift of zero results in a slope of zero, while a shift of one sample point results in a phase shift of 180^o at σ_{nq}.

linear phase error is generally straightforward and leaves minimal residual linear phase in the spectrum[38].

3.5.3 Non-linear phase errors - ϕ_{NL}

Several factors may contribute towards nonlinear phase in FTS spectra[30]. Dispersion in the beamsplitter substrate often contributes nonlinear phase. In a normal dispersive medium, higher frequencies (shorter wavelengths) appear delayed in time or trail the lower frequencies (longer wavelengths)[69]. This results in a chirped interferogram as shown in figure 3.4. By use of a phase compensating plate in the appropriate arm of the interferometer (figure 3.5) it is possible to minimize the $\phi_{NL}(\sigma)$ component introduced by the beamsplitter.

Dispersion can be described empirically by the Cauchy equation[30]:

$$n(\lambda) = C_1 + C_2\lambda^{-2} + C_3\lambda^{-4} + \cdots + C_m\lambda^{-2(m-1)}, \tag{3.20}$$

where $n(\lambda)$ represents the index of refraction of the dispersive medium, and the C_m terms are empirical constants. Typically, only the low order terms are included. Since the index of refraction may also be expressed as a function of σ, the beamsplitter will respond differently to different frequencies, potentially causing chirping in the interferogram. An example of nonlinear phase due to beamsplitter dispersion for the TFTS beamsplitter is shown in figure 3.6.

Dispersion compensator plates can be used to minimize the nonlinear phase. Figure 3.5 illustrates the use of an optical compensating plate in a classical Michelson interfer-

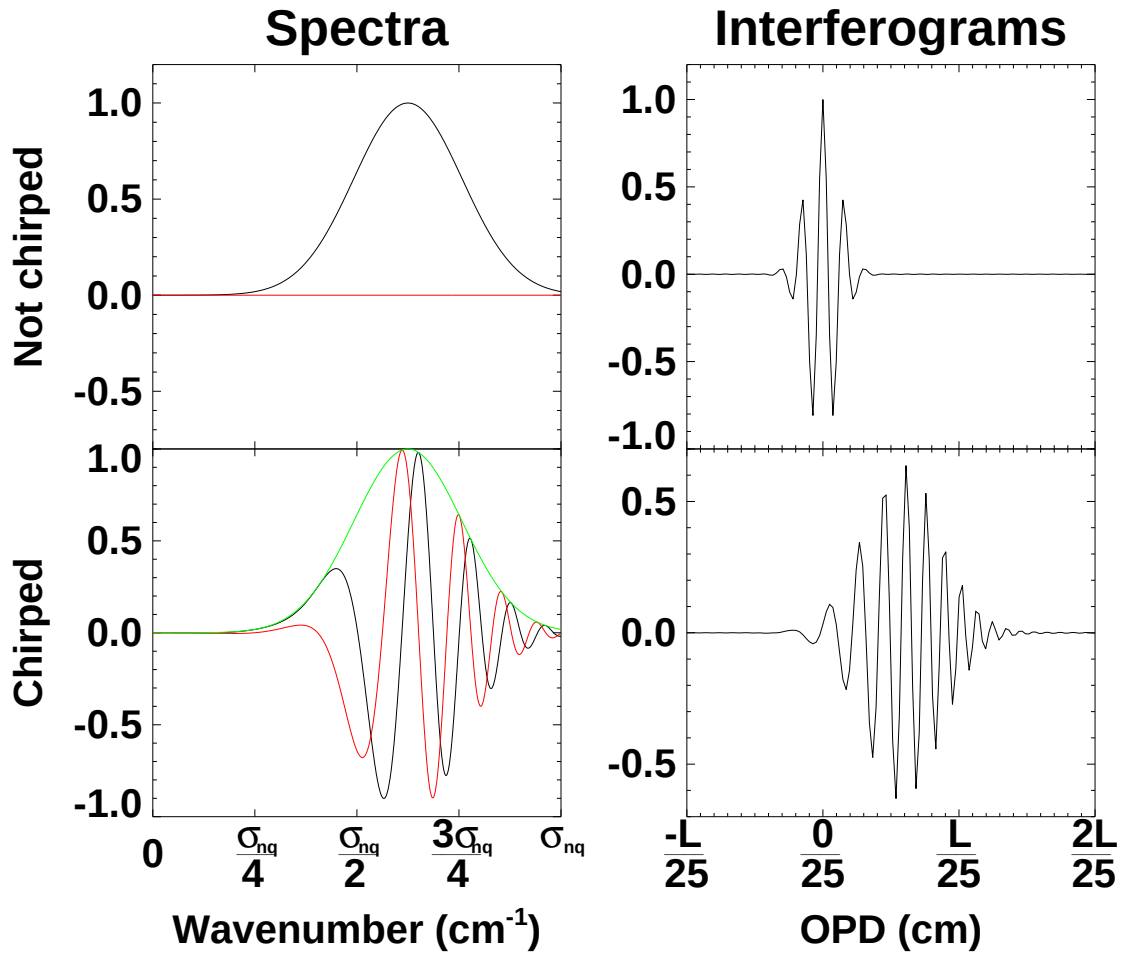

Figure 3.4: The resultant chirping from a non-linear spectral phase error. The top row shows the original non-chirped spectrum/interferogram and the bottom row shows the chirped case. The left column shows the spectra, with the real component in black, the imaginary component in red, and the absolute value shown in green (chirped case only). The right column shows the interferograms. The chirped phase has both a linear and quadratic component. The chirped interferogram has no point of stationary phase (equation 3.19). For both interferograms the location of ZPD is 0 cm. L represents the maximum OPD.

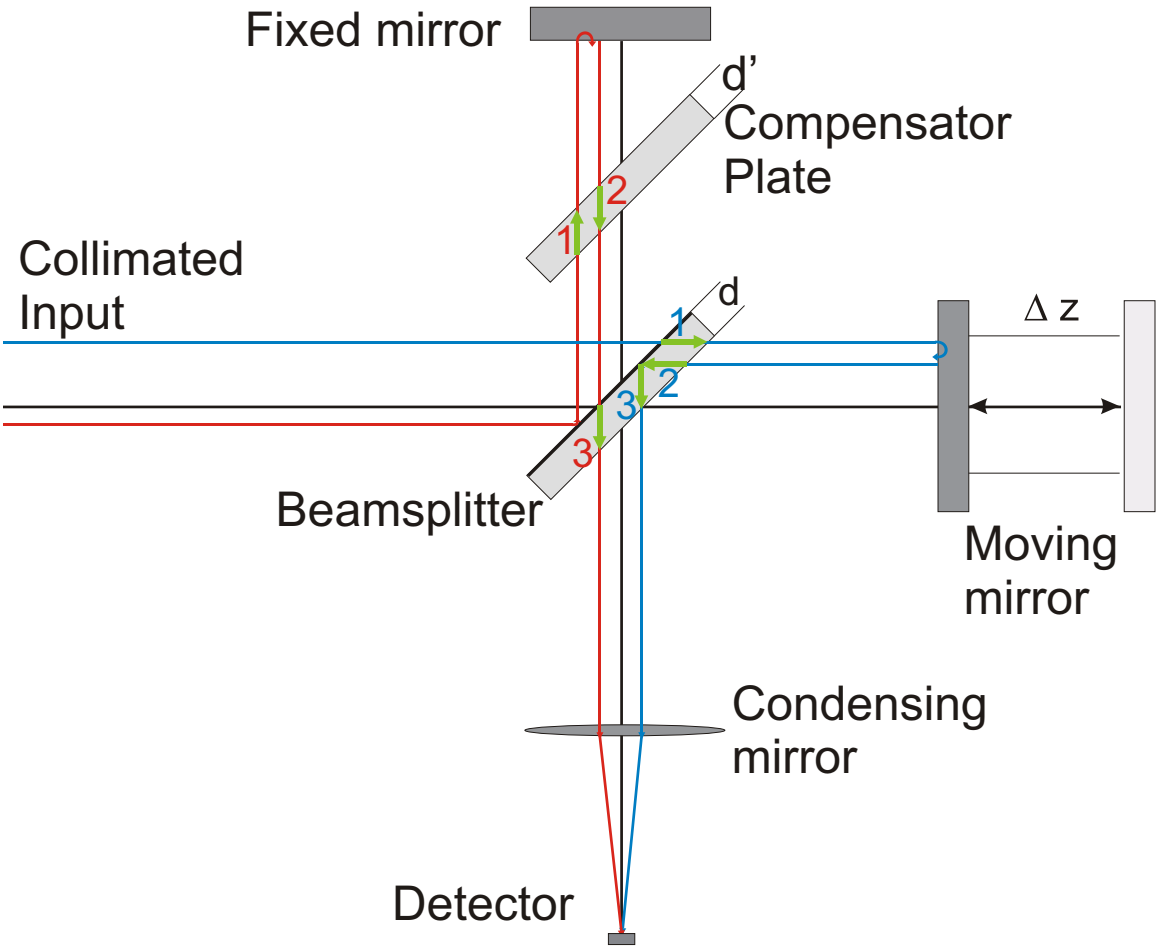

Figure 3.5: A compensator plate may be used in the fixed beam path of a Michelson interferometer in order to correct OPD errors resulting from the difference between the fixed and moving mirror paths of an interferometer. Without the compensator plate, the red path would only pass through the beamsplitter once, while the blue path passes through the beamsplitter three times. The beamsplitter is reflective on the upper left side, and the substrate thickness is labeled on the figure as d. The thickness of the compensator plate is labeled as d'. The difference between d and d' is referred to as η in equation 3.21. The non-reflective side of the beamsplitter and both sides of the compensator may be coated with an anti-reflection coating to reduce undesired reflections. Phase error will result from compensator mismatch.

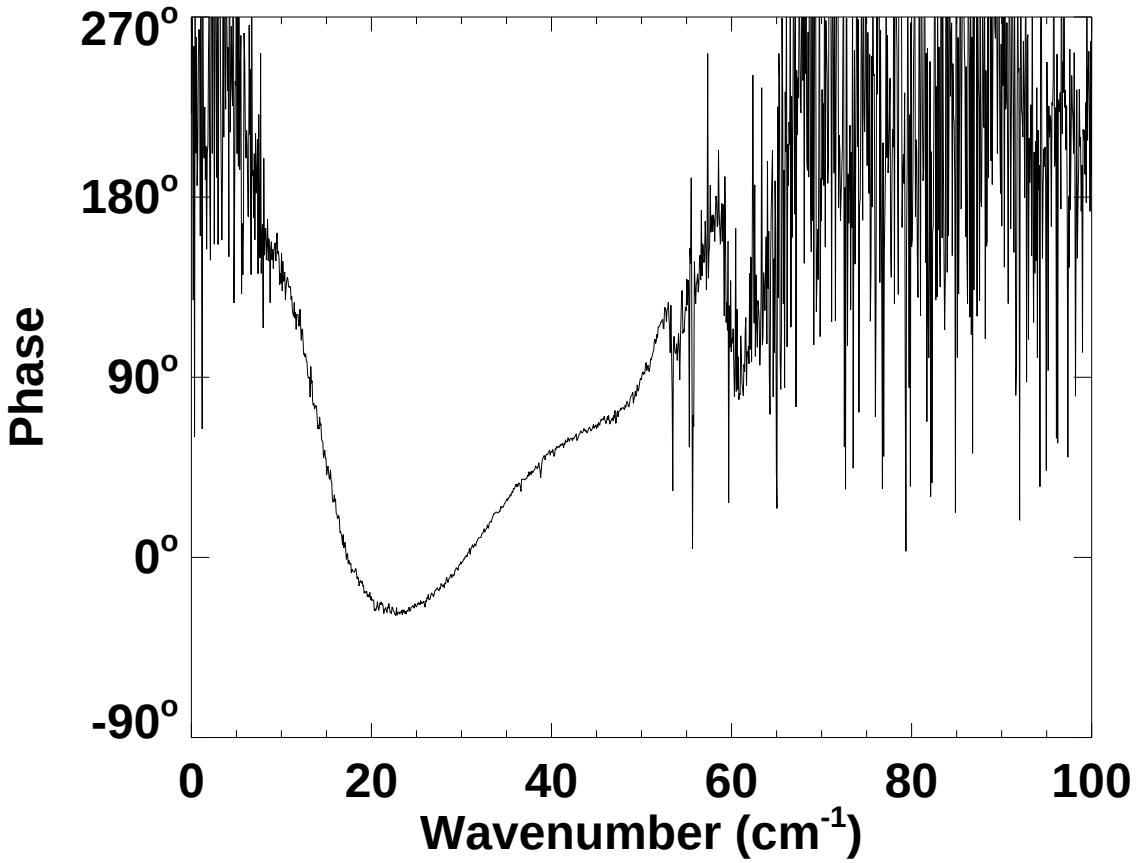

Figure 3.6: A measure of the $\phi_{NL}(\sigma)$ dispersive phase of the TFTS beamsplitter. The phase was determined by averaging several linear phase corrected interferograms of a 1300 K Blackbody source measured with the SPIRE TFTS (chapter 6). The phase as shown is the result of two data sets from different detectors (both used with the TFTS) being merged together to cover a window including the entire SPIRE band. Below 7 cm^{-1} and above 55 cm^{-1} the phase is undetermined because of low S/N.

ometer. Sheahen indicates that optical compensation errors can result in a constant phase offset at best, and often a frequency dependant phase as well[70]. Optical compensation is also done at the cost of optical efficiency and throughput[37, p. 125]. Learner[64] discusses nonlinear phase as the result of an optical mismatch when a compensator plate is used. In this case, the phase takes the form:

$$\phi(\sigma) = 2\pi\sigma[n(\sigma) - 1]\eta, \tag{3.21}$$

where $n(\sigma)$ is the refractive index of the material, and η is the mismatch in thickness (cm_{opd}). For constant index of refraction, this turns into a linear phase error, but for a dispersive medium this remains nonlinear, provided that $\eta \neq 0$. FTS mirror misalignment may also cause nonlinear phase errors. Kunz and Goorvitch[71] describe how the combined effect of a converging beam of light and a translation stage mirror misalignment in a Michelson interferometer produce interferogram asymmetries. Each effect considered separately leads to a symmetric interferogram with reduced modulation intensity, however the combined effect also causes asymmetry in the interferogram. Schröder and Geick[72] discuss how an angular misalignment in the moving mirror of a Michelson interferometer may lead to interferogram asymmetry if the beamsplitter is not at the focal plane (as is usually the case), or if the source is not collimated. Usually the beam is collimated with the residual divergence as minimal as possible to satisfy the Jaquinot criterion[37] (see equation 2.46). Goorvitch[73] has also shown misalignment of the moving mirror in a Michelson interferometer to cause a nonlinear phase error:

$$\phi_{NL}(\sigma) = -\arctan(\frac{\pi D\alpha\sigma}{\sqrt{2}(f/)})^2, \tag{3.22}$$

where D is the distance from the fixed mirror to the focus, α is the mirror misalignment angle (radians), and $f/$ is the f number of the radiation traversing the FTS instrument. For $(\frac{\pi D\alpha\sigma}{\sqrt{2}(f/)})^2 < 1$, as is also a requirement to minimize interferogram power loss[71] due to a mirror misalignment in an FTS instrument with converging light, the nonlinear phase relation simplifies to become quadratic:

$$\phi_{\mathrm{NL}}(\sigma) = -(\frac{\pi D\alpha\sigma}{\sqrt{2}(f/)})^2. \tag{3.23}$$

For the SPIRE TFTS (chapter 6) the values of D and $f/$ are 66.3 cm and 2.33, respectively. For example, using the above equation it can be shown that the angular misalignment on the TFTS mirror must be kept within $0.005^o, 0.003^o, 0.003^o, 0.004^o$, and 0.002^o for the PLW, PMW, PSW, SLW, and SSW bands, respectively to have residual phase no greater than 1^o. Mirror alignment becomes more critical for higher frequencies as one would expect for any nonlinear function. Figure 3.7 illustrates the theoretical non-linear phase resulting from a varying TFTS mirror misalignment. As discussed earlier, electronics and filters may also introduce asymmetries into an interferogram, and thus introduce a non-zero phase component into the spectrum. Also, a symmetric interferogram may be recorded asymmetrically due to the frequency dependance of the response function of the detector and the electronic system[65].

Non-linear phase errors may create the illusion of spectral features where there are none[70]. Failure to correct for the nonlinear phase terms leads to line position shift as well as an asymmetric ILS[74, 64]. $\phi_{NL}(\sigma)$ is significantly more difficult to correct for than ϕ_{DC} and ϕ_{Lin}. It is important to minimize sources of $\phi_{NL}(\sigma)$ where possible, and to be aware of the residual $\phi_{NL}(\sigma)$ where it is not possible to remove. The SPIRE FTS is expected to

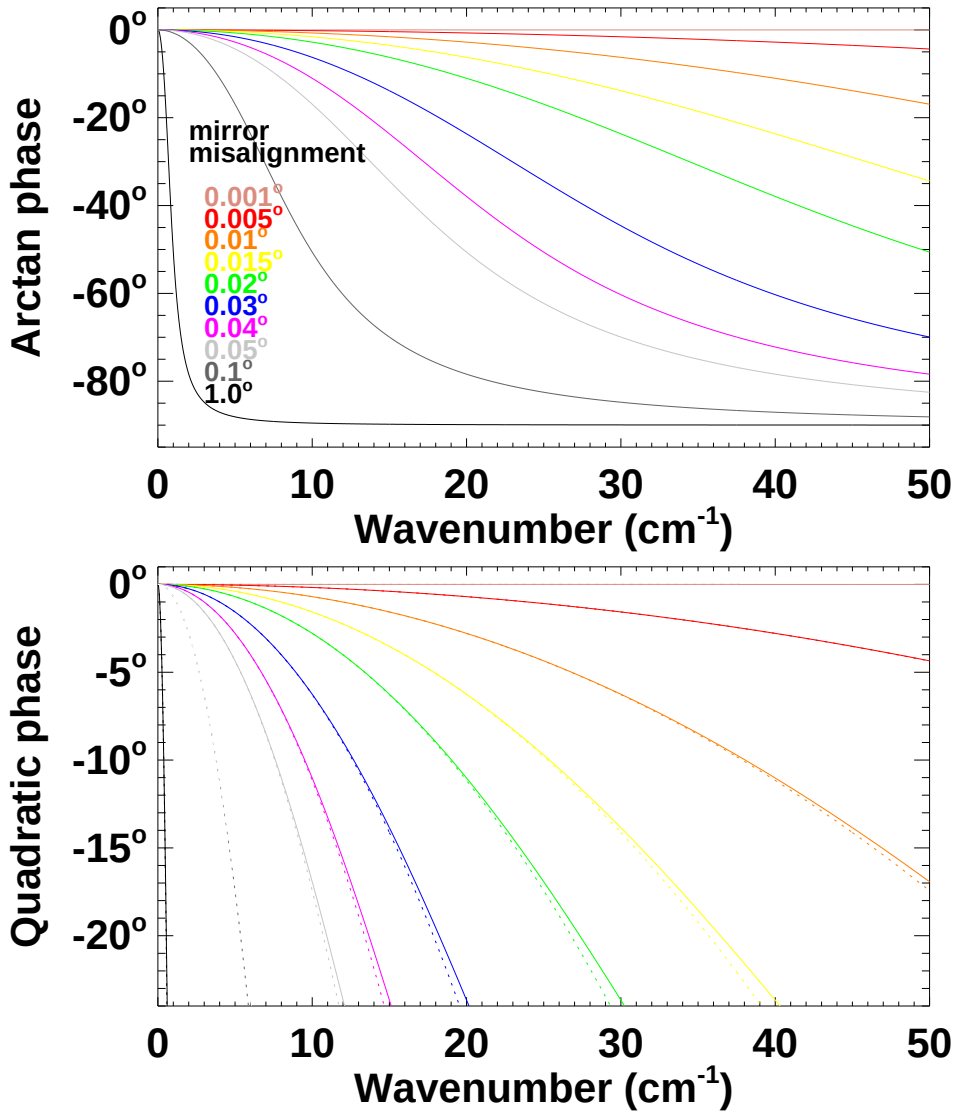

Figure 3.7: The effect of varying mirror misalignment on $\phi_{NL}(\sigma)$ for the SPIRE TFTS (equations 3.22 and 3.23). The upper plot shows the calculations using equation 3.22 without the simplifying assumption. The lower plot shows the curves from the upper plot (solid) in addition to the quadratic phase curves (broken) resulting from the power loss minimization restriction $((\frac{\pi D\alpha\sigma}{\sqrt{2}(f/)})^2 < 1)$.

have nonlinear phase[2] (figure 3.6) which will require phase correction prior to quantitative spectral analysis. However, the TFTS nonlinear phase is systematic and therefore remains constant for the instrument (see section 4.5). Calibration measurements of the nonlinear phase allows the residual nonlinear phase of the TFTS to be minimized in post-processing.

3.5.4 Random phase errors - ϕ_R

An interferogram ($I(z)$) consists of two key measurements, optical signal (I) and OPD (z). The optical signal can be affected by both optical and electrical noise while the optical path measurement can be affected by mechanical vibrations and electrical noise. Noise is discussed in detail in section 2.10.2. Interferogram noise will propagate into the spectrum, which will in turn introduce noise into the phase. Phase uncertainty is related to spectral uncertainty by the inverse of the spectral amplitude ($\delta\phi(\sigma) = \frac{\delta B(\sigma)}{|B(\sigma)|}$, see appendix D). Therefore, phase uncertainty is greatest in regions of low spectral amplitude.

An ideal FTS will be designed such that all noise levels are reduced to the point where photon noise dominates. Random noise should affect the real and imaginary domains of the spectrum equally. Therefore, phase correction has the potential of affecting the spectral noise due to the redistribution of the spectrum between the real and imaginary domains. Random noise levels are reduced through improving interferometer stage metrology and optical signal S/N. Slowly varying phase information is typically within the centreburst[38] (i.e. ZPD) region of the interferogram where S/N is the highest. The random noise contribution to phase, $\phi_R(\sigma)$, can never be completely removed but can be minimized through FTS design and data processing techniques (see chapter 5).

[2]According to TFTS verification measurements (section 6.5)

3.6 Phase correction methods

Phase correction is the technique of correcting asymmetric interferograms[38]. In principle, to correct the phase, the phase distorted spectrum ($B(\sigma)e^{i\phi(\sigma)}$) must be multiplied by the reciprocal of the phase ($e^{-i\phi(\sigma)}$):

$$B(\sigma) = [B(\sigma)e^{i\phi(\sigma)}]e^{-i\phi(\sigma)}, \tag{3.24}$$

however this is more complicated in practice as every spectral data point only has corresponding phase information if the interferogram used to generate the spectrum is double-sided. Since phase is expected to be slowly varying, phase correction methods have been developed to extract low resolution phase information from the double-sided portion of the interferogram to correct the higher resolution spectrum obtained from the one-sided portion of the interferogram.

The essential result of any phase correction procedure is to restore the spectral energy from the imaginary domain back to the real, leaving only the undesired imaginary noise behind. In the spectral domain, this rotation of energy to the real domain from the imaginary is accomplished with a multiplication by the reciprocal phase function (equation 3.24). In the interferogram domain, this corresponds to a convolution (table B.1) by the appropriate function known as the phase correction function (PCF) (equation 3.31). This section will discuss both the multiplicative (Mertz[54]) and the convolution (Forman[46, 61, 75]) phase correction methods.

3.6.1 The Mertz Method

In Mertz phase correction[54] the initial step is the determination of the double-sided phase (equation 2.39). The spectrum from the single-sided interferogram is of a higher resolution than that of the phase information provided by the double-sided interferogram. A combination of zero filling and linear interpolation is used to determine the phase at the required resolution[76]. Apodization of the double-sided interferogram is recommended, and in his original paper, Mertz suggested that a triangular type of apodization[77] (figure E.1) be used on the double sided interferogram although this is now regarded as far from optimal[78]. The Mertz method found favour through its elegant simplicity decades ago when computer capabilities were significantly less than they are today and multiplication was much preferred to convolution[60].

The single-sided interferogram needs to be appropriately weighted to ensure that each point of optical retardation is equally accounted for. Multiplying an apodizing function with an interferogram is equivalent to convolving the corresponding spectrum with the Fourier transform of the apodizing function (more on apodizing in section 4.8). The Fourier transform of the apodizing function is known as the ILS[38].

Unequal weighting of interferogram points results in deviations in the ILS from the ideal sinc profile (see section 2.10.4). Ideally all of the points that are doubly accounted for would be weighted equally, and the weighting of the remaining points would be twice that of the doubly accounted points. This is not practical, however, as the weighting function would then have discontinuities at $\pm L_{DS}$. To address this discontinuity problem a linear weighting with value of 0 beginning at $-L_{DS}$ and ending with a value of 1 at $+L_{DS}$ within

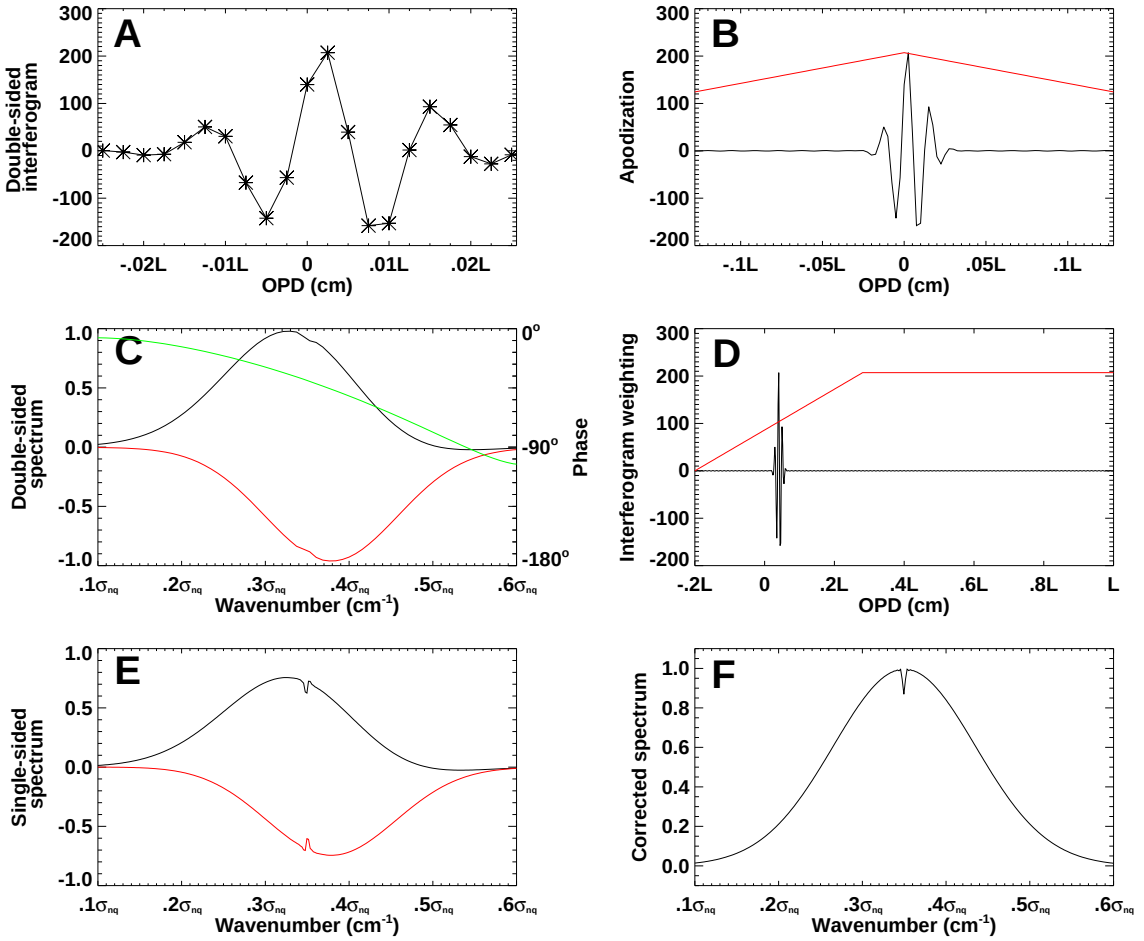

Figure 3.8: Mertz phase correction involves a narrow double-sided interferogram (A) , suitably apodized (B), to obtain a low resolution spectrum (real - black, imaginary - red) and phase (green) (C). The phase is interpolated and used to generate a multiplicative correction function. The full interferogram is weighted (D) to obtain the uncorrected high resolution spectrum (E). The real component of the complex multiplication of $e^{-i\phi(\sigma)}$ and E result in the corrected spectrum (F). In all spectral plots, black is the real component, and red is the imaginary.

the double-sided window is used instead of the flat amplitude of $\frac{1}{2}$ (see figures 3.9 & 3.10). This also ensures that each point receives the appropriate weighting without having an abrupt discontinuity at $+L_{DS}$.

The linear weighting scheme is based on the assumption of a symmetric interferogram. Phase correction is fundamentally necessary because interferograms are not symmetric and therefore this assumption is problematic. Chirped interferograms are not symmetric and thus the linear weighting scheme devised to overcome the discontinuity problem is not the best solution. Other methods to have appropriate weighting, avoid function/derivative discontinuities, and to equally weight an asymmetric double-sided interferogram use curved (e.g. cosinusoidal) sections between the flat regions as is shown in figure 3.9. Examples of various Mertz envelope weighting functions, $Env_{Mertz}(z)$, with their corresponding complex $ILS(\sigma)$ functions are shown in Figures 3.9 & 3.10.

3.6.2 The complex line shape of the Mertz method

As shown in figures 3.9 & 3.10, the Fourier transform of $Env_{Mertz}(z)$ can be expressed in terms of real and imaginary components:

$$ILS_{Mertz}(\sigma) = ILS_{real}(\sigma) + iILS_{imaginary}(\sigma), \tag{3.25}$$

where $ILS_{real}(\sigma)$ is symmetric and $ILS_{imaginary}(\sigma)$ is antisymmetric. $Env_{Mertz}(z)$ multiplied with the interferogram is equivalent to convolving $ILS_{Mertz}(\sigma)$ with the spectrum as follows (see section 4.8):

$$Env_{Mertz}(z) \times I(z) \Leftrightarrow [ILS_{real}(\sigma) + iILS_{imaginary}(\sigma)] * B(\sigma). \tag{3.26}$$

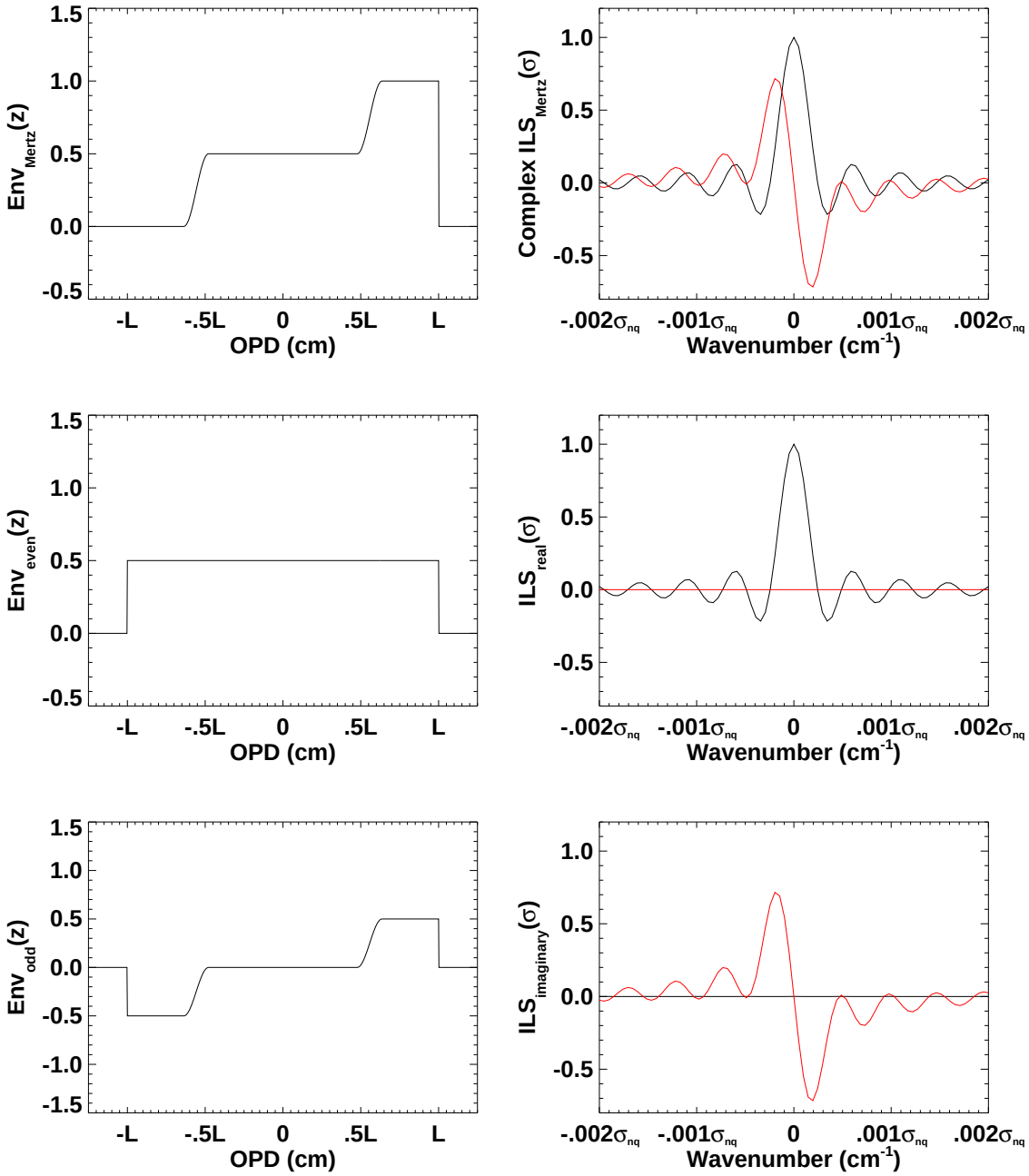

Figure 3.9: A typical weighting function used in the Mertz method of phase correction. The central region is doubly accounted for and as such each point is weighted by 0.5. $Env_{Mertz}(z)$ can be broken up into an even ($Env_{even}(z)$) and an odd ($Env_{odd}(z)$) component as is shown. The ILS of the even component is exactly a sinc function and the ILS of the odd portion is entirely imaginary. The transition between weighting levels is done with a sinusoidal function to ensure no discontinuities in both the function and its derivative. The real components of the spectra are shown in black and the imaginary components are shown in red.

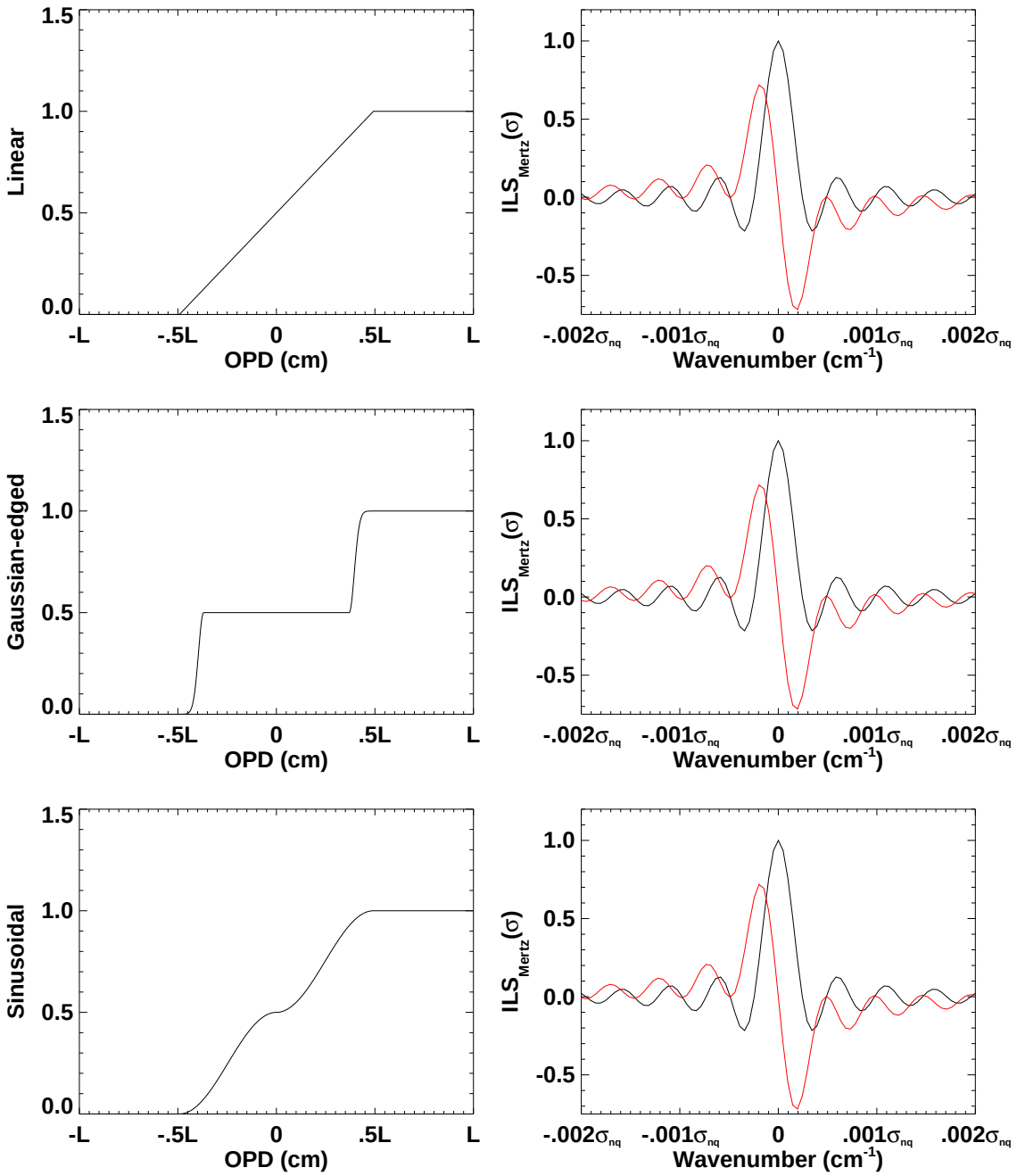

Figure 3.10: Other potential weighting functions for the Mertz method. First is shown the linear function proposed by Mertz, second is a function with Gaussian transition curves, and third is shown wide sinusoidal curves in the double-sided portion of the interferogram. The even portion of all of the weighting functions results in a real valued sinc spectral ILS. The real components of the spectra are shown in black and the imaginary components are shown in red.

In this equation $\Leftrightarrow$ represents the Fourier transform pair (see appendix B) and convolution is denoted by $*$ (see appendix C). Since an ideal interferogram has a wholly real spectrum; the real part of the convolution, $ILS_{real}(\sigma) * B(\sigma)$, gives the required spectrum, and the imaginary part can be discarded. For even a small residual phase error in the spectrum, $\phi_{residual}(\sigma)$ (expressed in radians), the imaginary part can no longer be completely ignored. The spectrum, $B(\sigma)$, which only has a real component, is observed[3] to be complex valued due to the residual phase (ignoring the ILS convolution for now):

$$B_{obs}(\sigma) = B(\sigma)e^{i\phi_{residual}(\sigma)}, \tag{3.27}$$

and using the small angle approximation (equation 3.15) can be expressed as:

$$\begin{aligned} B_{obs}(\sigma) &= B(\sigma)e^{i\phi_{residual}(\sigma)} \\ &= B(\sigma)cos(\phi_{residual}(\sigma)) + iB(\sigma)sin(\phi_{residual}(\sigma)) \\ &\approx B(\sigma) + i\phi_{residual}(\sigma)B(\sigma). \end{aligned} \tag{3.28}$$

Therefore, $B(\sigma)$ is recovered by taking the real portion of $B_{obs}(\sigma)$, however equation 3.28 neglected the ILS convolution that also affects the observed spectrum. Equation 3.29 does take the ILS convolution into account. The combination of residual phase and an imaginary portion to the ILS results in the real portion of $B_{obs}(\sigma)$ being different from the expected $B(\sigma) * ILS_{real}(\sigma)$. Since the ILS width should be fairly narrow, $\phi_{residual}(\sigma)$ should be relatively constant over the instrument profile. This allows the real part of the Mertz

[3]The subscript $_{obs}$ is used to differentiate the observed spectrum, $B_{obs}(\sigma)$, from the actual spectrum, $B(\sigma)$.

spectrum to be expressed as:

$$\begin{aligned} Re[B_{obs}(\sigma)] &= B(\sigma) * ILS_{real}(\sigma) - [\phi_{residual}(\sigma)B(\sigma)] * ILS_{imaginary}(\sigma) \\ &\approx B(\sigma) * [ILS_{real}(\sigma) - \phi_{residual}(\sigma)ILS_{imaginary}(\sigma)] \\ &\neq B(\sigma) * ILS_{real}(\sigma). \end{aligned} \tag{3.29}$$

The difference between the expected and observed real spectrum is

$$[\phi_{residual}(\sigma)B(\sigma)] * ILS_{imaginary}(\sigma).$$

It is important to note that within this additional term, $ILS_{imaginary}(\sigma)$ is of odd symmetry so the effective ILS is distorted. The added term involving the asymmetric instrument function displaces and distorts all the observed lines by an amount proportional to the residual phase error[64]. Thus the ILS no longer has the ideal sinc profile, but has an added asymmetric contribution.

The above expressions show asymmetric ILS even with residual phase assumed to be small enough to allow the small angle approximation (equation 3.15) and to be slowly varying. If $\phi_{residual}(\sigma)$ is not small or slowly varying, then the simplifying assumptions are no longer valid and the resulting Mertz ILS is even more complicated and distorted from the ideal[76, 79, 80].

3.6.3 The Forman Method

In this method, also known as the symmetrization-convolution method[61, 76], the short double-sided portion of the interferogram is used to calculate the phase spectrum at low resolution (equation 2.39). The resulting phase spectrum is then used to generate a

phase correction function (PCF) given by:

$$PCF(z) = \int_{-\infty}^{+\infty} e^{-i\phi(\sigma)} e^{+2\pi\sigma z} d\sigma. \tag{3.30}$$

Convolution of the PCF with the original interferogram results in a symmetric interferogram:

$$I_{symmetric}(z) = I_{asymmetric}(z) * PCF(z). \tag{3.31}$$

The fundamental phase determination used in the Forman method is similar to the Mertz method, however, the two methods now proceed along different paths. The Forman method utilizes the equivalence of the multiplication/convolution Fourier transform pair (see table B.1). Rather than multiply the high resolution spectrum by the reciprocal of the phase, $e^{-i\phi(\sigma)}$, the original interferogram is convolved with the PCF. Forman argues that prior to the calculation of the PCF, mathematical bandpass filtering can be added into the data processing at no extra processing or information cost[61]. The PCF may also be apodized in order to minimize the introduction of spectral artifacts, which are caused by discontinuities at the boundaries of the PCF being convolved through the interferogram. Forman developed his own apodization function[61, 39] (see appendix E) for the PCF apodization.

Forman also discussed repeating the convolution more than once to further improve the spectral correction. Theoretically, however, if the phase correction convolution function was determined correctly the first time, one convolution should be sufficient to phase correct the interferogram (see section 4.2).

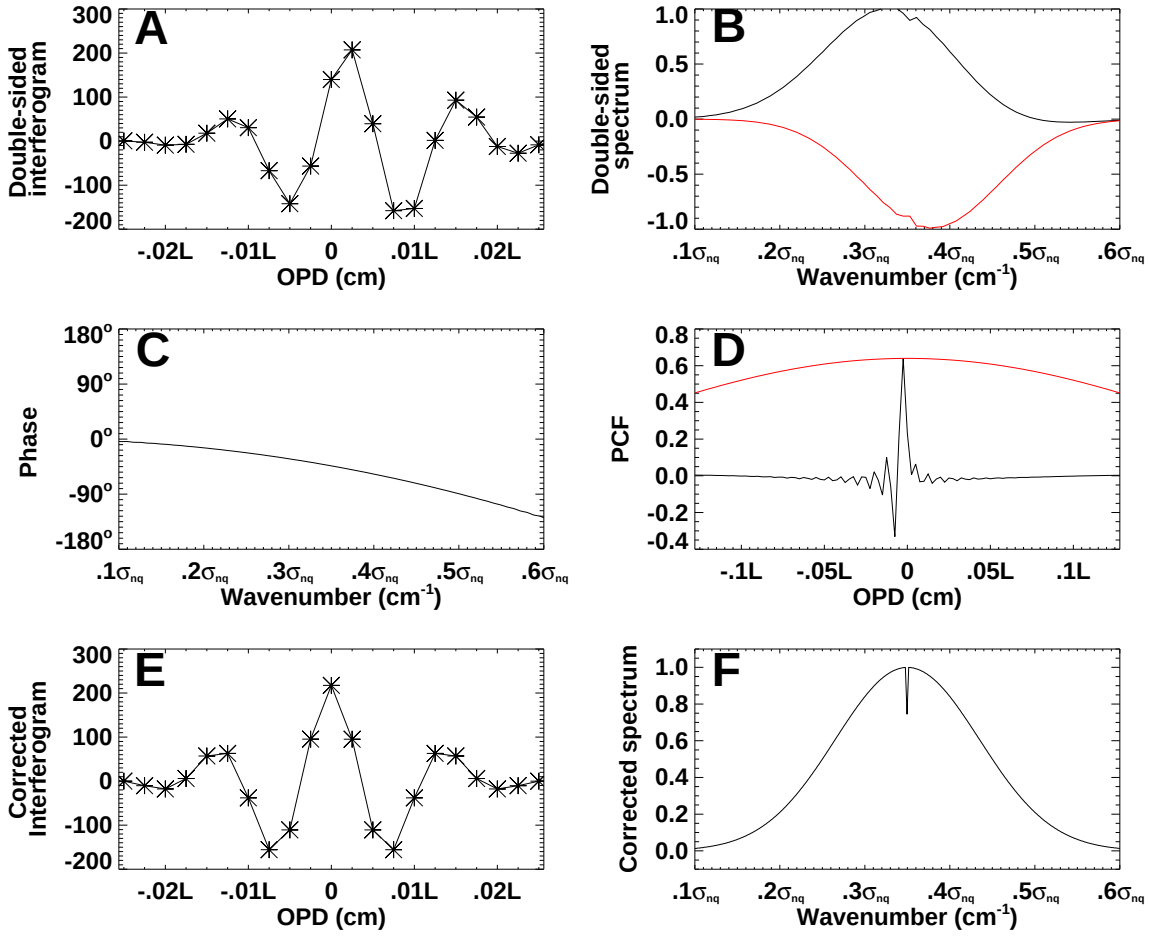

Figure 3.11: The Forman phase correction method involves a narrow double-sided interferogram (A), used to obtain low resolution amplitude (B) and phase (C) spectra. The phase correction function (D) is generated from the phase (equation 2.39) and convolved with the original single-sided interferogram to generate the phase corrected interferogram (E). D also shows the PCF apodization function (red) which Forman developed (equation E-4). The corrected high resolution spectrum (F) shows a broad Gaussian continuum with an unresolved absorption line. In all spectral plots, black and red show the real and imaginary components, respectively.

3.6.4 Phase correction of emission line spectra

Phase correction of emission line spectra is similar to continuum and absorption spectra phase correction, but is complicated by the fact that the phase uncertainty is inversely proportional to spectral amplitude[64]. Therefore phase information is only present in a spectrum where there is non-zero amplitude, which is more prevalent with a continuum present. There are two main limitations to phase determination in emission spectroscopy. First is the limited S/N, second is the availability of suitable reference lines. One method that is commonly used to determine the instrumental phase involves using a strong continuum source. With correction of systematic phase from instrument calibration measurements, the only additional correction required on each individual interferogram is linear, which is fairly straightforward with even a relatively low number of emission lines. SPIRE will not have phase determination issues due to lack of continuum because of the prevalence of broad spectral emission in the sub-mm Infrared (IR) band. Phase correction of emission line spectra becomes an issue for higher frequencies such as ultra violet (UV) spectroscopy where continuum emission is not typically present[81].

Two related problems occur in the phase correction of emission spectra that are not usually significant for absorption spectra. The first is that reliable phase information is only present within strong emission lines. The second problem is that there are mechanisms that introduce false phase data such as ghosting effects. As long as the phase determination of an emission spectrum is done properly, the remainder of the phase correction is similar to absorption/continuum phase correction methods.

3.6.5 Other approaches to phase correction

There are other methods of phase correction which have found a more limited use than the Mertz and Forman based methods. For example, precise line shape error minimization is a different approach to phase correction which only requires one-sided interferograms. Other methods use different means of phase error identification. These methods will not be discussed here, but are discussed in the literature[65, 70, 74, 82, 83].

3.7 Comparison of the Mertz and Forman methods

The fundamental equivalence between the Mertz and Forman method lies in the convolution/multiplication Fourier transform pair (see appendix B and table B.1). Both phase correction methods are equivalent to the first order[84], however secondary effects vary. Both phase correction methods were introduced at a time when computer processing capabilities were far more primitive than they are today. As a result, the relative simplicity of the spectral multiplication utilized in the Mertz method gained favour over the complicated interferogram convolution found in the Forman method. As FTS instruments and data processing capabilities have advanced through the years, the advantages of the simplistic Mertz phase correction have lost ground over the versatility of the Forman phase correction method.

3.7.1 General comparisons

In order to illustrate the differences between the Mertz and Forman phase correction methods, both methods have been used to correct the same interferograms. The input

spectra are composed of a broad Gaussian emission line with an unresolved Gaussian absorption feature superimposed. Two basic types of phase error, both linear and quadratic, are introduced to distort the interferograms. All of the processing parameters were kept identical to ensure a valid comparison. The spectral output of each method as well as the difference from the input spectrum is shown in figure 3.12.

Phase Error type		Forman		Mertz	
		Linear	Quadratic	Linear	Quadratic
Continuum	Amplitude	0.41 %	0.42 %	1.24 %	0.95 %
	Line centre	0.0016 %	0.0012 %	0.0015 %	-0.0599 %
	Line width	-0.12 %	-0.12 %	-2.54 %	-2.53 %
Unresolved	Amplitude	24.7 %	24.7 %	61.7 %	61.6 %
	Line centre	-0.027 %	-0.027 %	-0.027 %	-0.027 %
	Line width	2.19 %	2.19 %	22.39 %	22.37 %

Table 3.1: Comparison of the spectral feature errors from the Mertz and Forman methods of phase correction with linear and quadratic phase error. Errors are represented as percentages of the model parameters for the zero-phase spectrum. The errors on the amplitude of the unresolved absorption line are significantly larger than any of the other parameters. This is primarily due to the nature of the unresolved line and the fact that the spectrum is only discretely sampled. The Forman method preserves the lineshape significantly better than the Mertz method as is shown in figure 3.13.

To quantitatively evaluate the phase correction methods, an Interactive Data Language (IDL)[3] procedure was written to fit the spectrum to a theoretical one containing a broad Gaussian continuum and an unresolved (sinc) absorption line centered at the same frequency. In this analysis the line amplitude, centre, and width for both the Gaussian and unresolved lines were free parameters. The minimization of χ^2 in this six-dimensional space was used to determine the parameters for the best model fit. The phase corrected spectra as well as the modeled fit spectra for the Mertz and Forman methods with linear and quadratic phase error are shown in figure 3.13. The resulting errors in amplitude, line

centre, and line width are shown in table 3.1.

Both the linear and the chirped (quadratic phase) interferograms are corrected better by the Forman method than by the Mertz method. The point of stationary phase (z_o), about which the interferogram symmetry is expected to lie, is shifted for an interferogram with linear phase and does not exist for a chirped interferogram. The unequal weighting of the double-sided interferogram in the Mertz method (figure 3.10) weights the positive OPD region of the interferogram with more confidence than the negative OPD region. This will introduce artifacts into the Mertz spectrum (and ILS) because of the lack of symmetry of an interferogram with phase errors. This is evidenced by the fact that Mertz line centre error is comparable to Forman line centre error, however other spectral errors (with a stronger connection to the ILS) are significantly larger for the Mertz correction than for the Forman correction (table 3.1).

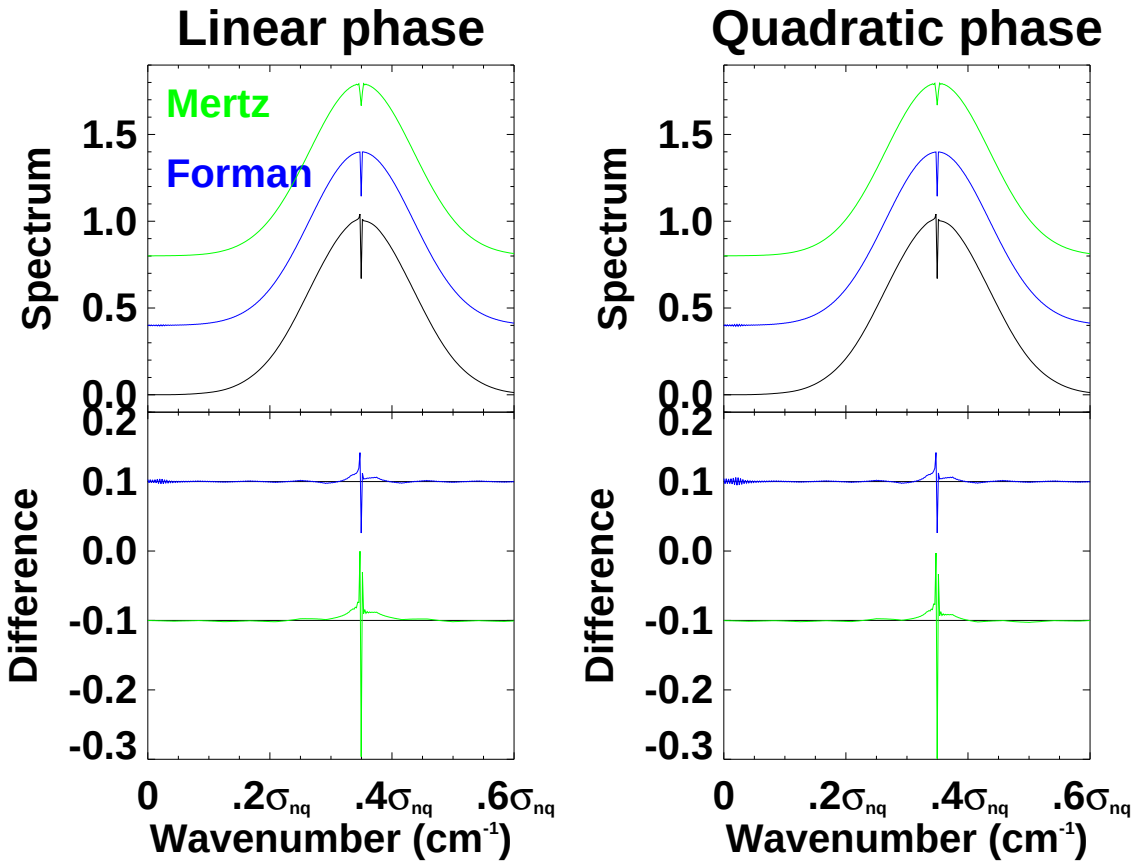

Figure 3.12: Spectra resulting from the Mertz and Forman phase correction methods on data with linear and quadratic phase. The zero-phase spectrum is shown in black, with the Forman spectra shown in blue and the Mertz spectra shown in green. Below each spectral plot is a plot showing the difference from the phase corrected spectrum and the zero phase spectrum. The Forman difference plots are shown in green while the Mertz difference plots are shown in blue. The graphs have been offset for clarity.

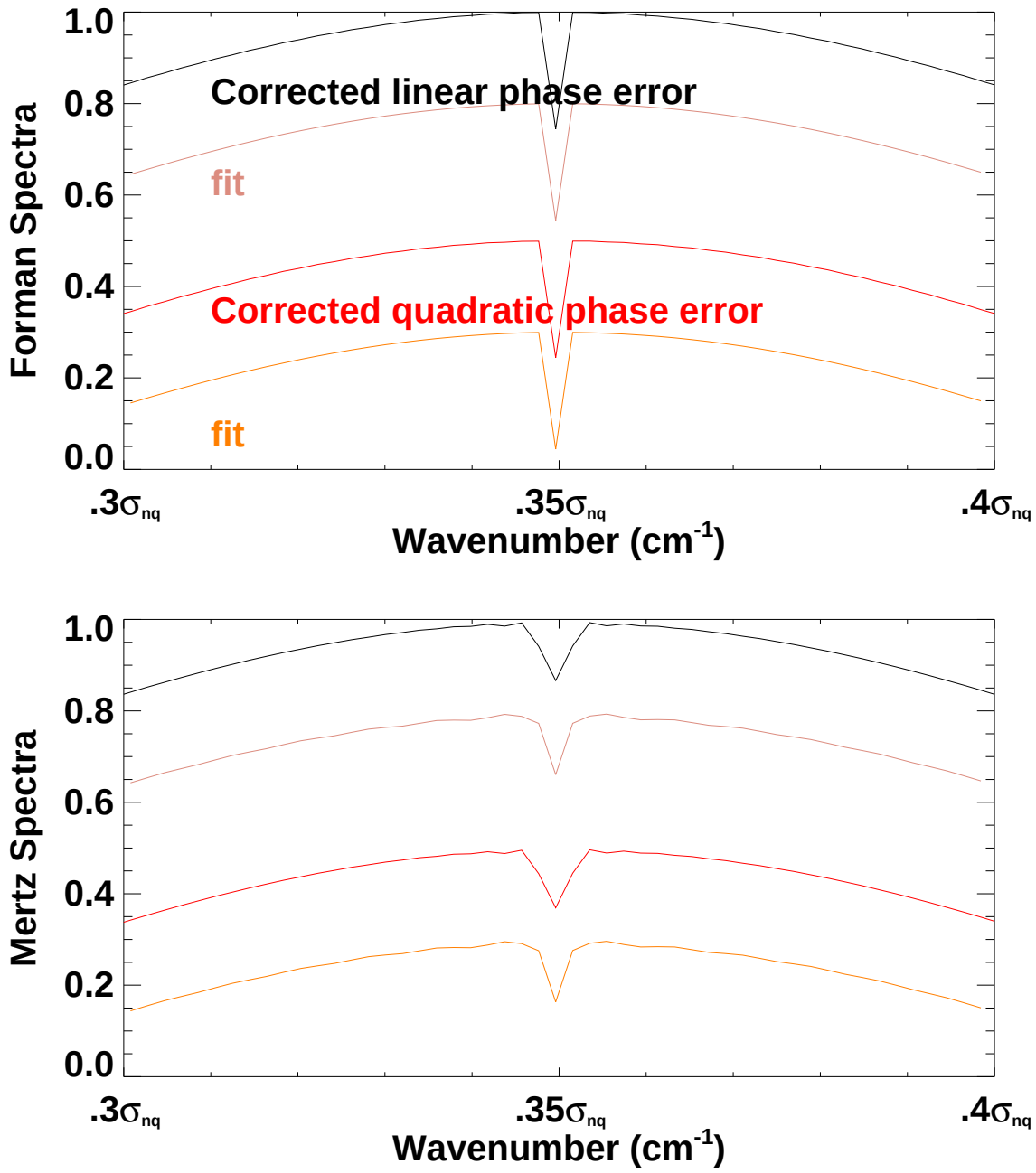

Figure 3.13: Output spectrum from the Mertz and Forman methods compared to the least squares fit. From top to bottom (in colours black, brown, red, orange), the curves shown are spectrum (corrected for linear phase error), fit (of the spectrum immediately above), spectrum (corrected for quadratic phase error), and fit (of the spectrum immediately above). The Forman results are shown in the top figure while the Mertz results are shown in the bottom figure. Note the reduced amplitude of the unresolved absorption line in all the Mertz spectra. The data illustrated here is the same as is illustrated in figure 3.12.

3.7.2 Comparisons for SPIRE instrument verification

The effect of both phase correction methods on the modeled spectra for SPIRE ground testing is also important. Details of the SPIRE ground testing and CQM model verification will be discussed elsewhere (chapter 7), however, a simple spectrum including a blackbody radiation source, atmospheric transmission, beamsplitter phase, optical filter profile, and mirror efficiency has been generated to assist in the preparation of data processing software[15]. In order to evaluate the performance of both methods of phase correction, output spectra are generated and compared to a zero-phase spectrum of the same model data. The spectra and differences are shown in figure 3.14. Application of the phase correction techniques discussed in this chapter applied to the optimization of SPIRE data processing is found in chapter 5.

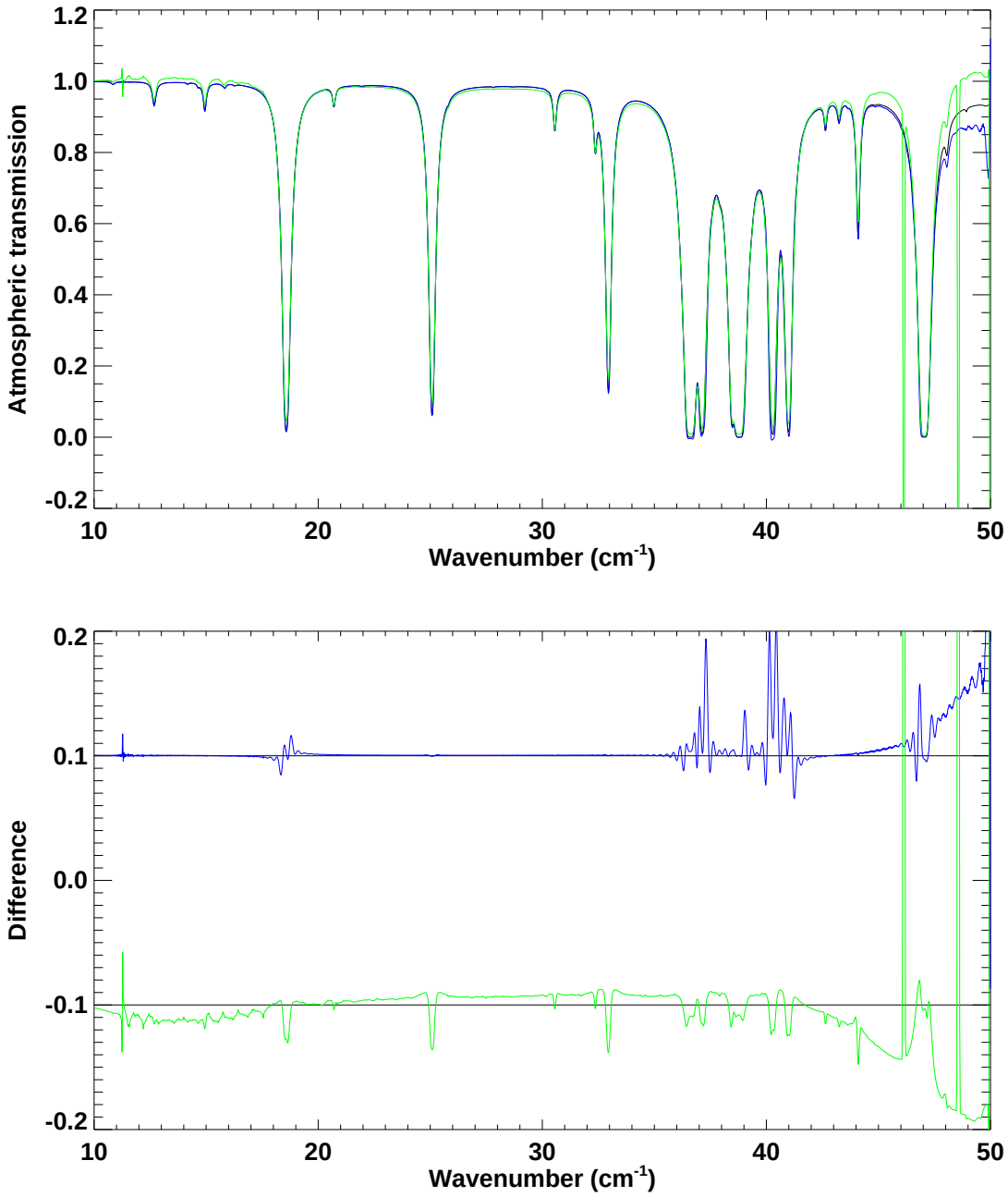

Figure 3.14: A model atmospheric transmission spectrum for the SPIRE ground test facility at RAL. The atmospheric beampath length is 5m, with temperature 290 K and 1013 mbar pressure. Double-sided and single-sided resolution are at 0.07 and 0.014 cm^{-1} respectively, comparable to the capabilities of the SPIRE TFTS (chapter 6). The Forman and Mertz methods are shown in blue and green, respectively. The differences (below) are offset for clarity. The in-band RMS error of the Mertz method is an order of magnitude larger than that of the Forman method (0.12 vs. 0.02).

3.8 Conclusions

Phase errors can be systematic, variable, and random. Whenever possible, systematic phase can be minimized and calibrated at the instrument level. Nonlinear phase errors are typically both systematic and difficult to correct for and thus should be minimized, with residual nonlinear phase recorded with calibration measurements. The most common variable phase error is linear, which is easily corrected.

The Forman phase correction method has been shown to perform better than the Mertz method, as is illustrated in section 3.7. Chase discovered that for a comparable number of points the residual errors were less for the Forman method than for the Mertz method[76]. There are situations when the Mertz method will suffice, however, the quality of the resultant spectrum will be greater if the Forman method of phase correction is used. An enhanced version of the Forman method is discussed in chapter 4. Several sources in the literature cite the advantages of the Forman method over the Mertz method.[61, 62, 39, 76, 79, 84] For these reasons, a Forman based method (see chapter 4) has been selected to correct the phase errors in the SPIRE/CQM verification test campaign.

Bibliography

[1] M. K. Tahic and D. A. Naylor. Apodization Functions for Fourier Transform Spectroscopy. In *Fourier transform spectroscopy topical meeting*. Optical Society of America, Feb 2005.

[2] J. W. Cooley and J. W. Tukey. An algorithm for the machine calculation of complex fourier series. *Math. Comput.*, 19:297, 1965.

[3] Interactive Data Language, Research Systems Inc., 2004.

[4] Göran L. Pilbratt. Herschel Mission: status and observing opportunities. In *Optical, Infrared, and Millimeter Space Telescopes, Proc. SPIE*, volume 5487, pages 401 – 412, Jun 2004.

[5] M. F. Kessler, J. A. Steinz, M. E. Anderegg, J. Clavel, G. Drechsel, P. Estaria, J. Faelker, J. R. Riedinger, A. Robson, B. G. Taylor, and S. Ximénez de Ferrán. The infrared space observatory (iso) mission. *Astronomy and Astrophysics*, 315:L27 – L31, 1996.

[6] Göran L. Pilbratt. The ESA FIRST cornerstone mission. In *UV, Optical, and IR*

Space Telescopes and Instruments, Proc. SPIE, volume 4013, pages 142–151, Mar 2000. SPIE symposium, 29-31 March 2000.

[7] http://www.astro.utu.fi/tuorla/new/mirror.shtml.

[8] http://herschel.jpl.nasa.gov/lagrange.shtml.

[9] Matthew J. Griffin, Bruce M. Swinyard, and L. Vigroux. The Herschel - SPIRE instrument. In *Optical, Infrared, and Millimeter Space Telescopes, Proc. SPIE*, volume 5487, pages 413 – 424, Jun 2004.

[10] Douglas Griffin, Matt Griffin, and Bruce Swinyard. Spire design description. Technical Report SPIRE-RAL-PRJ-000620, Rutherford Appleton Laboratory, May 2003.

[11] Bruce M. Swinyard, P. A. R. Ade, M. J. Griffin, K. Dohlen, J. Baluteau, D. Pouliquen, D. Ferand, P. Dargent, G. Michel, J. Martignac, L. Rodriguez, D. Jennings, M. Caldwell, A. Richards, P. Hamilton, and David A. Naylor. The first-spire spectrometer: A novel imaging fts for the sub-millimetre. *SPIE Proceedings: UV, Optical, and IR Space Telescopes and Instruments*, 4013:196–207, 2000.

[12] P. A. R. Ade, P. A. Hamilton, and David A. Naylor. An absolute dual beam emission spectrometer. In *FTS Topical Meeting*, Santa Barbara, California, June 1999. Optical Society of America.

[13] Tanya Lim, Bruce Swinyard, A. A. Aramburu, J. Bock, M. Ferlet, Doug Griffin, Matt J. Griffin, Peter Hargrave, Ken King, Sarah Leeks, David Naylor, Samuel Ronayette, Eric Sawyer, Bernhard Schulz, Sunil Sider, Locke Spencer, Dave Smith, and

Adam Woodcraft. First Results from Herschel - SPIRE performance tests. In *Optical, Infrared, and Millimeter Space Telescopes, Proc. SPIE*, volume 5487, pages 460 – 468, Jun 2004.

[14] Kjetil Dohlen, Alain Origne, and Marc Ferlet. Optical alignment verification of the Herschel - SPIRE instrument. In *Optical, Infrared, and Millimeter Space Telescopes, Proc. SPIE*, volume 5487, pages 448 – 459, Jun 2004.

[15] Locke D. Spencer, David A. Naylor, Bruce M. Swinyard, Asier A. Aramburu, Trevor R. Fulton, Tanya L. Lim, Samuel D. Ronayette, and Ian S. Schofield. A Fourier Transform Spectrometer for Ground Testing of the Herschel/SPIRE Instrument. In *Astronomical Telescopes and Instrumentation*, volume 5487, pages 501 – 512, Jun 2004.

[16] John Lindner, David A. Naylor, and Bruce M. Swinyard. Simulation of the Performance of ESA's Herschel - SPIRE Imaging Fourier Transform Spectrometer. In *Optical, Infrared, and Millimeter Space Telescopes, Proc. SPIE*, volume 5487, pages 469 – 480, Jun 2004.

[17] Bruce Sibthorpe, Adam Woodcraft, Matthew Griffin, and S. Lloyd Watkin. A software simulator for the Herschel - SPIRE imaging photometer. In *Optical, Infrared, and Millimeter Space Telescopes, Proc. SPIE*, volume 5487, pages 491 – 500, Jun 2004.

[18] Matthew Griffin, Bruce Swinyard, and Laurent Vigroux. SPIRE - Herschel's Submillimetre Camera and Spectrometer. In *IR Space Telescopes and Instruments, Proc. SPIE*, volume 4850, pages 686–697, Mar 2003.

[19] Bruce Swinyard, Kjetil Dohlen, Didier Ferand, Jean Paul Baluteau, Dominique Pouliquen, Pascal Dargent, Guy Michel, Jerome Martignac, Peter Ade, Peter Hargrave, Matthew Griffin, Donald Jennings, and Martin Caldwell. The Imaging FTS for Herscel SPIRE. In *IR Space Telescopes and Instruments, Proc. SPIE*, volume 4850, pages 698–709, Mar 2003.

[20] Goutam Chattopadhyay, Jason Glenn, James J. Bock, Brooks Rownd, Martin Caldwell, and Matthew J. Griffin. Feed Horn Coupled Bolometer Arrays for SPIRE: Design, Simulations, and Measurements. *IEEE Transactions on Microwave Theory and Techniques*, 51(10):2139–2146, Oct 2003.

[21] Patrick A. Collins, Peter A. R. Ade, M. Caldwell, M. Ferlet, M. J. Griffin, Pete C. Hargrave, M. R. Harman, Dave L. Smith, and Bruce M. Swinyard. A Ground Calibration Facility for Herschel - SPIRE. In *IR Space Telescopes and Instruments, Proc. SPIE*, volume 4850, Mar 2003.

[22] Matthew Griffin, Bruce Swinyard, and Laurent Vigroux. The SPIRE instrument for FIRST. In *UV, Optical, and IR Space Telescopes and Instruments, Proc. SPIE*, volume 4013, pages 184–195, Mar 2000. SPIE symposium, 29-31 March 2000.

[23] Göran L. Pilbratt. The FIRST ESA Cornerstone Mission. In *UV, Optical, and IR Space Telescopes and Instruments, Proc. SPIE*, volume 3356, pages 452–461, Mar 1998. SPIE symposium, 25-28 March 1998 in Kona, Hawaii.

[24] Matthew Griffin, Laurent Vigroux, Bruce Swinyard, and Colin Cunningham. SPIRE - a bolometer instrument for FIRST. In *Advanced Technology MMW, Radio, and*

Terahertz Telescopes, Proc. SPIE, volume 3357, pages 404–413, Mar 1998. SPIE symposium, 20-28 March 1998 in Kona, Hawaii.

[25] D.A. Naylor, T.R. Fulton, P.W. Davis, I.M. Chapman, B.G. Gom, Locke D. Spencer, J.V. Lindner, N.E. Nelson-Fitzpatrick, M.K. Tahic, and G.R. Davis. Data processing pipeline for a time-sampled imaging fourier transform spectrometer. In *Proc. SPIE Imaging Spectrometry*, page X5546, August 2004.

[26] Locke D. Spencer and D. A. Naylor. Optimization of FTS Phase Correction Parameters. In *Fourier transform spectroscopy topical meeting*. Optical Society of America, Feb 2005.

[27] Brad G. Gom and David A. Naylor. An update on the imaging Fourier transform spectrometer for SCUBA-2. In *Astronomical Telescopes and Instrumentation*, volume 5498. SPIE, Jun 2004.

[28] Ivor Grattan-Guinness. *Joseph Fourier, 1768-1830*. Cambridge: MIT Press, 1972. a survey of his life and work, based on a critical edition of his monograph on the propagation of heat, presented to the Institut de France in 1807.

[29] John Herivel. *Joseph Fourier. The man and the Physicist*. Oxford University Press, 1975.

[30] Eugene Hecht. *Optics*. Addison Wesley, fourth edition, 2002.

[31] B. P. Lathi. *Signal Processing & Linear Systems*. Berkeley-Cambridge Press, Carmichael, 1998.

[32] Albert A. Michelson. *Light Waves and Their Uses*. University of Chicago Press, Chicago, Illinois, 1902.

[33] Albert A. Michelson. Measurement of Jupiter's Satellites by Interference. *Publications of the Astronomical Society of the Pacific*, 3:274–278, September 1891.

[34] Albert A. Michelson. Visibility of interference-fringes in the focus of a telescope. *Philosophical Magazine*, 31:256–259, june 1891.

[35] Fourier transform spectroscopy. *Applied Optics*, 6(4):692, April 1967.

[36] Albert A. Michelson. On the application of interference methods to spectroscopic measurements. *Philosophical Magazine*, 34:280–+, 1892.

[37] R. J. Bell. *Introductory Fourier Transform Spectroscopy*. Academic Press, New York, 1972.

[38] Sumner P. Davis, Mark C. Abrams, and James W. Brault. *Fourier Transform Spectroscopy*. Academic Press, first edition, 2001.

[39] P. R. Griffiths and J. A. Haseth. *Fourier Transform Infrared Spectrometry*. John Wiley and Sons, New York, 1986.

[40] Albert A. Michelson. Determination of Periodicities by the Harmonic Analyzer with an Application to the Sun-Spot Cycle. *Astrophysical Journal*, 38:268–275, October 1913.

[41] A. A. Michelson. Radiation in a Magnetic Field. *Astrophysics Journal*, 7:131–139, February 1898.

[42] H. Rubens and R. W. Wood. Focal isolation of long heat-waves. *Philosophical Magazine*, 21:249–261, 1911.

[43] P. Fellgett. A propos de la theorie du spectrometre interferentiel multiplex. *Journal of Physics Radium*, 19:187, 1958.

[44] P. Jacquinot. New developements in interference spectroscopy. *Rep. Prog. Phys.*, 23:267–312, 1960.

[45] J. Connes, P. Connes, and J. P. Maillard. *Atlas des spectres dans le proche infrarouge de Venus, Mars, Jupiter et Saturn.* Paris: Centre National de la Recherche Scientifique, 1969.

[46] Michael L. Forman. Fast Fourier-Transform Technique and it's Application to Fourier Spectroscopy. *Journal of the Optical Society of America*, 56(7):978, july 1966.

[47] Peter Gustav Lejeune Dirichlet, Richard Dedekind, and John Stillwell. *Lectures on Number Theory.* American Mathematical Society, 1999. translated from original title "Vorlesungen über Zahlentheorie" (1863) compiled and published shortly after Dirichlet's death in 1859.

[48] Eric W. Weisstein. Dirichlet Fourier Series Conditions. From MathWorld–A Wolfram Web Resource. http://mathworld.wolfram.com/ DirichletFourierSeriesConditions.html.

[49] J. S. Walker. *Fourier Analysis.* Oxford University Press, 1988.

[50] E. O. Brigham. *The Fast Fourier Transform.* Prentice-Hall Inc., 1974.

[51] Marc-Antoine Parseval. Mémoire sur les séries et sur l'intégration complète d'une équation aux differences partielle linéaires du second ordre, à coefficiens constans. *Académie des Sciences*, 1806. original submission was 5 April 1799.

[52] M. Born and E. Wolf. *Principles of Optics: Electromagnetic Theory of Propagation, Interference and Diffraction of Light*. Cambridge University Press, 1980.

[53] L. Mertz. Rapid scanning fourier transform spectroscopy. *J. Phys. Coll. C2, Suppl. 3-4*, 28:88, 1967.

[54] L. Mertz. *Transformations in optics*. New York: Wiley, 1965, 1965.

[55] D. A. Naylor, B. G. Gom, P. A. R. Ade, and J. E. Davis. Design and performance of a dual polarizing detector system for broadband astronomical spectroscopy at sub-millimetre wavelengths.

[56] Charles Kittel. *Introduction to Solid State Physics*. John Wiley & Sons, Inc., seventh edition, 1996.

[57] H. Nyquist. Certain topics in telegraph transmission theory. *Transactions of the American Institute of Electrical Engineers*, 47:617 – 644, 1928.

[58] C. E. Shannon. A mathematical theory of communication. *The Bell System Technical Journal*, 27:379 – 423, 1948.

[59] Adel S. Sedra and Kenneth C. Smith. *Microelectronic Circuits*. Oxford University Press, New York, 1998.

[60] L. Mertz. Optical Fourier synthesizer. *Journal of the Optical Society of America*, 46:548–551, 1956.

[61] Michael L. Forman, W. Howard Steel, and George A. Vanasse. Correction of Asymmetric Interferograms Obtained in Fourier Spectroscopy. *Journal of the Optical Society of America*, 56(1):59–63, 1966.

[62] Janine Connes. Computing Problems in Fourier Spectroscopy. In *Aspen International Conference on Fourier Spectroscopy, 1970*, volume AFCRL-71-0019, page 83, Bedford Mass., January 1971.

[63] J. C. Sheamen, W. R. Howell, G. F. Hohnstreiter, and I. Coleman. In *Aspen International Conference on Fourier Spectroscopy*, pages AFCRL–71–0019, 1970.

[64] R. C. M. Learner, A. P. Thorne, I. Wynne-Jones, J. W. Brault, and M. C. Abrams. Phase correction of emission line Fourier transform spectra. *Optical Society of America Journal A*, 12:2165–2171, October 1995.

[65] Thomas P. Sheahen and T. O. McCaney. Phase Discrepencies in Asymmetric Interferograms and Application to Nonlinearities in Fourier Spectroscopy. *Journal of the Optical Society of America*, 65(7):825–828, 1975.

[66] W. H. Press, S. A. Teukolsky, W. T. Vetterling, and B. P. Flannery. *Numerical Recipes in C: The Art of Scientific Computing*. Cambridge University Press, 1992.

[67] D. A. Naylor and T. A. Clark. A mid-infrared astronomical Fourier transform spectrometer. In *Instrumentation in astronomy VI; Proceedings of the Meeting, Tucson,*

AZ, Mar. 4-8, 1986. Part 2 (A87-36376 15-35). Bellingham, WA, Society of Photo-Optical Instrumentation Engineers, 1986, p. 482-490. NSERC-supported research., pages 482–490, 1986.

[68] J. Connes. *Rev. Opt.*, 40:45, 116, 171, 233, 1961. English translation as document AD 409869, Clearinghouse for Federal Scientific and Technical Information, Cameron Station, VA.

[69] Joseph T. Verdeyen. *Laser Electronics*. Prentice Hall, New Jersey, third edition, 1995.

[70] Thomas P. Sheahen. Importance of proper phase analysis in using Fourier transforms. *American Journal of Physics*, 44(1):22–25, 1976.

[71] Louis W. Kunz and David Goorvitch. Combined effects of a converging beam of light and mirror misalignment in michelson interferometry. *Applied Optics*, 13:1077–1079, 1974.

[72] B. Shcröder and R. Geick. The Problem of Nonlinear Phase Errors Introduced by Misalignment of a Michelson Interferometer. *Infrared Physics*, 18:595–605, 1978.

[73] David Goorvitch. Phase correction for a michelson interferometer with misaligned mirrors. *Applied Optics*, 14(6):1387–1390, 1975.

[74] David G. Johnson, Wesley A. Traub, and Kenneth W. Jucks. Phase determination from mostly one-sided interferograms. *Applied Optics*, 35(16):2955–2959, june 1996.

[75] W. Howard Steel and Michael L. Forman. Example of Errors Occurring in Fourier

Spectroscopy Due to Hilbert-Transform Effects. *Journal of the Optical Society of America*, 56:982, 1966.

[76] D. B. Chase. Phase Correction in FT-IR. *Applied Spectroscopy*, 36(3):240–244, 1982.

[77] L. Mertz. Auxiliary Computation for Fourier Spectrometry. *Infrared Physics*, 7:17–23, 1967.

[78] J. W. Brault. High Precision Fourier Transform Spectrometry: The Critical Role of Phase Corrections. *Mikrochimica Acta*, 3:215–227, 1987.

[79] R. B. Sanderson and E. E. Bell. Multiplicative Correction of Phase Errors in Fourier Spectroscopy. *Applied Optics*, 12(2):266–270, 1973.

[80] H. Sakai and G. A. Vanasse. Direct Determination of the Transfer Function of an Infrared Spectrometer. *Journal of the Optical Society of America*, 56(1):131, 1966.

[81] J. C. Pickering, A. P. Thorne, and R. Perez. Oscillator Strengths of Transitions in Ti II in the Visible and Ultraviolet regions. *The Astrophysical Journal Supplement Series*, 132:403–409, February 2001.

[82] R. R. Ernst and W. A. Anderson. Application of fourier transform spectroscopy to magnetic resonance. *Rev. Sci. Instrum.*, 37, 1966.

[83] Edward G. Codding and Gary Horlick. Apodization and Phase Information in Fourier Transform Spectroscopy. *Applied Spectroscopy*, 27(2):85–92, 1973.

[84] H. Sakai, G. A. Vanassse, and M. L. Forman. Spectral recovery in fourier spectroscopy. *Journal of the Optical Society of America*, 58(1):84 – 90, january 1968.

[85] C. Zhu and P. R. Griffiths. Extending the range of beer's law in ft-ir spectrometry. part 2: Theoretical study of continuous apodization functions. *Applied Spectroscopy*, 52:1409 – 1413, 1998.

[86] F. J. Harris. On the use of windows for harmonic analysis with the discrete fourier transform. In *Proceedings of the IEEE*, volume 66, pages 51–83, 1978.

[87] R. H. Norton and R. Beer. Errata. *Journal of the Optical Society of America*, 67:419, 1977.

[88] R. H. Norton and R. Beer. New apodizing functions for fourier spectrometry. *Journal of the Optical Society of America*, 66:259 – 264, 1976.

[89] A. S. Filler. Apodization and interpolation in fourier-transform spectroscopy. *Journal of the Optical Society of America*, 54:762 – 767, 1964.

[90] Margaret K. Tahic. Fourier transform spectroscopy of the orion molecular cloud. Master's thesis, University of Lethbridge, Lethbridge, Alberta, Canada, June 2005.

[91] John R. Taylor. *An Introduction to Error Analysis: The Study of Uncertainties in Physical Measurements*. University Science Books, second edition, 1997.

[92] J. A. Nelder and R. Mead. A simplex method for function minimization.

[93] M. J. D. Powell. A method for minimizing a sum of squares of non-linear functions without calculating derivatives.

[94] 2003. http://www.aerotech.com/products/accessories/mx.html.

[95] http://www.heidenhain.com/Products/ExposedLinear/lip.htm.

[96] Frederic Pinsard. Herschel/SPIRE Detector Control Unit Design Document. Technical Report SPIRE-SAP-PRJ-001243, Rutherford Appleton Laboratories, Feb 2003.

[97] Ian Chapman. The Atmosphere Above Mauna Kea at Mid-Infrared Wavelengths. Master's thesis, University of Lethbridge, Lethbridge, Canada, Dec 2002.

[98] Trevor R. Fulton. Deriving the beamsplitter phase from the data, 2005. Personal communication.

[99] J. C. Pearson, H. M. Pickett, B. J. Drouin, P. Chin, and E. A. Cohen. Microwave, Millimeter, Submillimeter and Far Infrared Spectral Databases. In *NASA Laboratory Astrophysics Workshop*, pages 145–148, November 2002. http://spec.jpl.nasa.gov/.

[100] I. G. Nolt, J. V. Radostitz, G. Dilonardo, K. M. Evenson, D. A. Jennings, K. R. Leopold, M. D. Vanek, L. R. Zink, A. Hinz, and K. V. Chance. Accurate rotational constants of CO, HCl, and HF: Spectral standards for the 0.3 to 6 THz (10 to 200 cm^{-1}) region. *Journal of Molecular Spectroscopy*, 125:274–287, October 1987.

[101] C. H. Townes and A. L. Schawlow. *Microwave Spectroscopy.* McGraw-Hill Book Company, 1955.

[102] Walter Gordy and Robert L. Cook. *Microwave Molecular Spectra.* Techniques of Chemistry. John Wiley & Sons, second edition, 1984.

[103] David J. Griffiths. *Introduction to Quantum Mechanics.* Prentice Hall, New Jersey, 1995.

[104] R. Shankar. *Principles of Quantum Mechanics*. Plenum Publishers, New York, second edition, 1994.

[105] Robin. R. Phillips. *Radiative Transfer Modelling of Star Formation Regions*. PhD thesis, University of Kent at Canterbury, April 1999.

[106] H. Blancher, G. Bachet, and R. Coulon. Frequency shifts of some pure rotational lines in polar mixtures in the far Infrared range. Experiments and theoretical predictions. *The Journal of Chemical Physics*, 85:2498–2501, September 1986.

[107] Jet Propulsion Laboratory, California Institute of Technology, CA, USA.

[108] Laboratoire d'Astronomie Spatiale, Marseille, France.

[109] Douglas Griffin, Matt Griffin, and Bruce Swinyard. Spire design description document. Technical Report SPIRE-RAL-PRJ-000620, Rutherford Appleton Laboratory, 2002.

[110] Trevor R. Fulton. Glitch simulation, 2004. Personal communication.

[111] M. Inguscio, G. Moruzzi, K. M. Evenson, and D. A. Jennings. A review of frequency measurements of optically pumped lasers from 0.1 to 8 THz. *Journal of Applied Physics*, 60:161–194, December 1986.

[112] O. I. Baskakov and J. Demaison. Spectroscopic Study of the v_6=1 and v_8=1 Vibrational States of Formic Acid, HCOOH: New Assignments of Laser Transitions. *Journal of Molecular Spectroscopy*, 211:262–272, February 2002.

[113] Marcel J. E. Golay. Theoretical consideration in heat and infra-red detection, with

particular reference to the pneumatic detector. *Review of Scientific Instruments*, 18(5):347–356, May 1947.

[114] LabVIEW, www.ni.com, National Instruments Inc.

[115] Arianespace Inc. Ariane 5 technical manual. http://www.arianespace.com/.

[116] B. Rownd, J. J. Bock, G. Chattopadhyay, J. Glenn, and M. J. Griffin. Design and performance of feedhorn-coupled bolometer arrays for SPIRE: Design, Simulation, and Measurements. In *Millimeter and Submillimeter Detectors for Astronomy. Edited by Phillips, Thomas G.; Zmuidzinas, Jonas. Proceedings of the SPIE*, volume 4855, pages 510–519, February 2003.

[117] Anthony D. Turner, James J. Bock, Jeffrey W. Beeman, Jason Glenn, Peter C. Hargrave, Voktor V. Hristov, Hien T. Nguyen, Faiz Rahman, Srinivasan Sethuraman, and Adam L. Woodcraft. Silicon nitride micromesh bolometer array for submillimeter astrophysics. *Applied Optics*, 40:4921–31, 2001.

[118] Roger R. Hildebrand. Focal plane optics in far-infrared and submillimeter astronomy. *Optical Engineering*, 25:323 – 330, 1986.

[119] D. A. Harper, R. H. Hildebrand, R. Stiening, and R. Winston. Heat trap: an optimized far infrared field optics system. *Applied Optics*, 15:53 – 60, 1976.

[120] R. H. Hildebrand and R. Winston. Throughput of diffraction-limited field optics systems for infrared and millimetric telescopes. *Applied Optics*, 21:1844 – 1846, 1982.

[121] Roland Winston. Light collection within the framework of geometrical optics. *Journal of the Optical Society of America*, 60:245 – 247, 1970.

[122] Frank J. Low. Low-temperature germanium bolometer. *Journal of the Optical Society of America*, 51:1300 – 1304, 1961.

[123] E. E. Haller. Physics and design of advanced bolometers and photoconductors. *Infrared Physics*, 25:257 – 266, 1985.

[124] Ian. M. Chapman and D. A. Naylor. Development of a Freely-Distributed, Customizable Atmospheric Radiative Transfer Model. In *Fourier transform spectroscopy topical meeting*. Optical Society of America, Feb 2005.

[125] J. W. S. Rayleigh. *Phil. Mag.*, 49, 1900.

[126] J. H. Jeans. *Phil. Mag.*, 10, 1905.

[127] J. C. G. Lesurf. *Millimetre-wave Optics, Devices and Systems*. Adam Hilger, New York, 1990.

[128] L.S. Rothman, D. Jacquemart, A. Barbe, D. Chris Benner, M. Birk, L.R. Brown, M.R. Carleer, C. Chackerian Jr., K. Chance, L.H. Coudert, V. Dana, V.M. Devi, J.-M. Flaud, R.R. Gamache, A. Goldman, J.-M. Hartmann, K.W. Jucks, A.G. Maki, J.-Y. Mandin, S.T. Massie, J. Orphal, A. Perrin, C.P. Rinsland, M.A.H. Smith, J. Tennyson, R.N. Tolchenov, R.A. Toth, J. Vander Auwera, P. Varanasi, and G. Wagner. The hitran 2004 molecular spectroscopic database. *Journal of Quantitative Spectroscopy & Radiative Transfer*, 96:139 – 204, 2005.

[129] Centre spatial de liège. www.csl.ulg.ac.be/Download/PDF/SpaceEnvironmentalTest.pdf.

[130] Spire canada. http://research.uleth.ca/spire/.

[131] The infrared astronomical satellite. http://irsa.ipac.caltech.edu/IRASdocs/iras.html.

[132] David B. Gallagher, William R. Irace, and Michael W. Werner. The development and mission of the space infrared telescope facility (sirtf). In *Optical, Infrared, and Millimeter Space Telescopes, Proc. SPIE*, volume 5487, pages 13 – 25, Jun 2004.

[133] Hiroshi Murakami. ASTRO-F Infrared Sky Survey Mission. In *Optical, Infrared, and Millimeter Space Telescopes, Proc. SPIE*, volume 5487, pages 330 – 337, Jun 2004.

[134] European Space Agency. Herschel science centre home page. http://www.rssd.esa.int/herschel/.

[135] G. Rybicki and A. P. Lightman. *Radiative Processes in Astrophysics*. Wiley-Interscience, New York, 1979. "The Planck Spectrum", pp.3-4 and 20-23.

[136] Eric E. Weisstein. Rayleigh-jeans law. From ScienceWorld–A Wolfram Web Resource. http://scienceworld.wolfram.com/ physics/ Rayleigh-JeansLaw.html.

Appendix C

Preliminary design of FTS-2: an imaging Fourier transform spectrometer for SCUBA-2

David A. Naylor*[a], Brad G. Gom[a], Baoshe Zhang[a]
[a]Dept. of Physics, University of Lethbridge, 4401 University Drive, Lethbridge, Alberta, Canada T1K 3M4

ABSTRACT

We present the preliminary design of FTS-2, an imaging Fourier transform spectrometer (IFTS) for use with SCUBA-2, the second generation, wide-field, submillimetre camera currently under development for the James Clerk Maxwell Telescope (JCMT). This system, which is planned for operation at the start of 2007, will provide simultaneous broadband spectral imaging across both the 850 and 450 μm bands with variable resolution ranging from resolving powers of R ~10 to 5000. The spectrometer uses a folded Mach-Zehnder configuration and novel intensity beam dividers. The mechanical and optical design of FTS-2 as of the Critical Design Review stage of the project are discussed, along with the interfaces with SCUBA-2 and the JCMT.

Keywords: Fourier, Spectrometer, SCUBA-2, Submillimetre, JCMT

1. INTRODUCTION

One of the major unsolved problems of modern astrophysics is a detailed understanding of the processes underlying star formation. Since star formation is intimately linked with planetary formation, this problem has fundamental significance not only for our immediate galactic environment, but also in the study of the early universe. Despite significant progress in the past two decades[1,2], several aspects of star formation remain poorly understood, including:

- What are the physical conditions at the onset of, and what initiates protostellar collapse in a molecular cloud?
- What is the efficiency and time scale of star formation?
- What determines the distribution of stellar masses at birth (the initial mass function)?

It is now well established that stars form from the collapse of dense cloud cores in the interstellar medium, but remain cocooned in their natal envelopes of gas and dust. The optical opacity of this material is so great that these cores can only be studied at far-infrared and submillimetre wavelengths where the dust emission is optically thin. A number of space and ground-based astronomical instruments, many of them discussed in these proceedings, are currently under development to address these questions.

Building on the highly successful SCUBA camera[3], which operated on the James Clerk Maxwell Telescope (JCMT) between 1997 and 2005, a new, large format, submillimetre camera, SCUBA-2, is currently under development for use at the JCMT[4]. SCUBA-2 features two dc-coupled, monolithic TES filled arrays with a total of ~10,000 bolometers, unlike previous detectors which have used much smaller arrays of discrete bolometers. With its larger format and increased sensitivity, SCUBA-2 promises a factor of 1000 increase in mapping speed compared to its predecessor.

While SCUBA-2 will provide unprecedented morphological information on the structure of submillimetre astronomical sources, their composition and physical conditions can only be determined through imaging spectral measurements. A Fourier Transform Spectrometer (FTS) has been selected as the optimal instrument for medium resolution spectroscopy when used in conjunction with SCUBA-2. This choice was based on the well known advantages of Fourier spectroscopy, including:

*naylor@uleth.ca; phone 1 403 329-2426; fax 1 403 329-2057; www.uleth.ca/phy/naylor/

- Simultaneous broadband, readily adjustable intermediate resolution measurements across both the 850 and 450 µm SCUBA-2 bands
- The best instrumental line shape function of any spectrometer
- Intrinsic wavelength calibration and relatively easy intensity calibration

FTS-2 will be primarily a galactic spectrometer (e.g. spectral index mapping of molecular clouds), but will also provide useful information on bright nearby galaxies and planetary atmospheres. FTS-2 thus fills a niche between the two band SCUBA-2 continuum images and the higher spectral resolution, but limited-sized images produced by the JCMT heterodyne facility instrument HARP-B.

Since the layout of the JCMT - SCUBA-2 feed optics was well advanced prior to the decision to include an intermediate resolution spectrometer, the mechanical, optical, and software design of FTS-2 was significantly more challenging. Previous papers have discussed the conceptual design of FTS-2.[5,7] In this paper we review the current PDR level design of the FTS-2 instrument emphasizing the optical, mechanical and software design, as the project enters the CDR phase.

2. OPTICAL DESIGN

FTS-2 intercepts the SCUBA-2 optical beam near an intermediate image plane directly outside the telescope elevation bearing opening (see Fig. 1). The optical design problem is essentially to reproduce the original image and pupil after the beam for each port has passed through the interferometer, while maintaining unity image magnification, in order to allow the instrument to be used with the existing SCUBA-2 feed optics. Within the interferometer, there are additional design constraints that the beams at the rooftop mirrors must be collimated, there must be pupils located at the rooftop mirrors (at the ZPD location) for symmetry, and there must also be pupils near the beamsplitters in order to minimize the beamsplitter diameters.

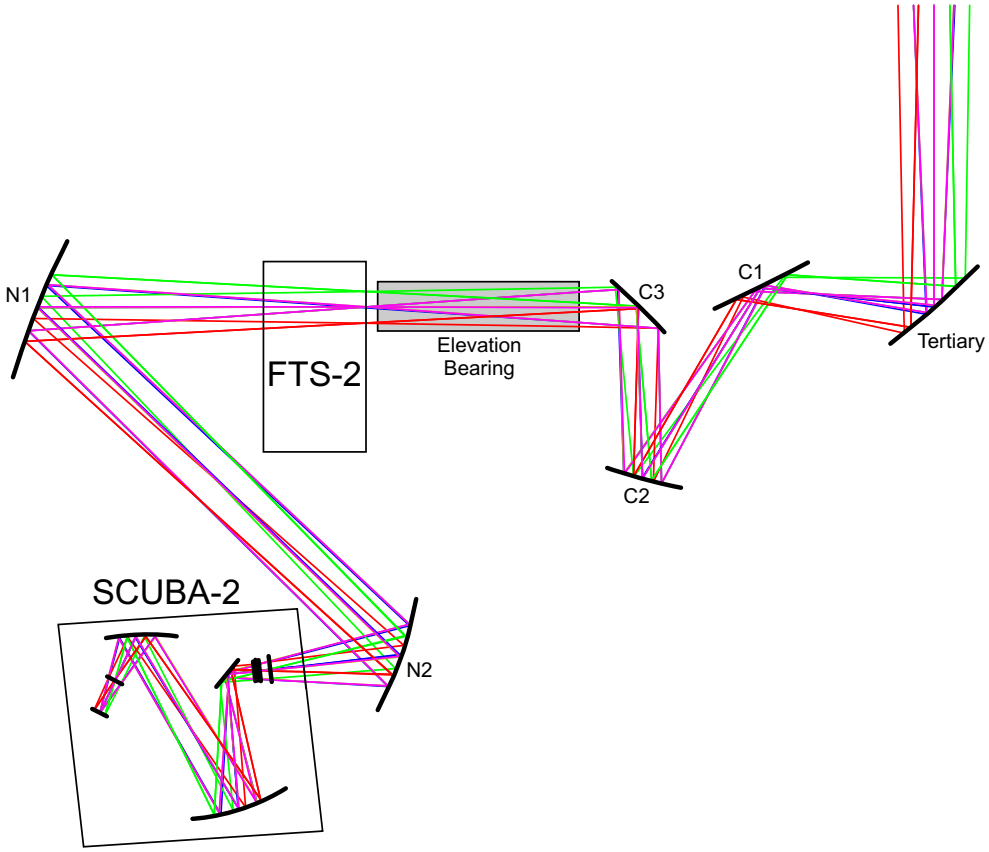

Fig. 1. FTS-2 location within the JCMT SCUBA-2 feed optics.

FTS-2 uses a dual-input, dual-output Mach-Zehnder interferometer configuration[6] which allows 2 ports to be placed on the sky for atmospheric cancellation. A linear schematic of the FTS-2 optics for one port of the interferometer is shown in Fig. 2. A pickoff mirror intercepts one quadrant of the SCUBA-2 FOV near an intermediate image plane outside the telescope elevation bearing. Mirror FM2_1 folds the beam downwards and creates an image after the first beamsplitter (BS), minimizing the beamsplitter diameter. Mirror FM1_3 folds the beam at the breadboard level and forms a pupil image at the apex of the moving rooftop mirrors (RT) when the interferometer is at ZPD. After reflection from the RT mirrors, fold mirrors FM1_4 and FM2_2 return the beam to the elevation bearing level and reproduce the input pupil and image at the required positions before the return mirror feeds the beam back to the SCUBA-2 feed optics at N1.

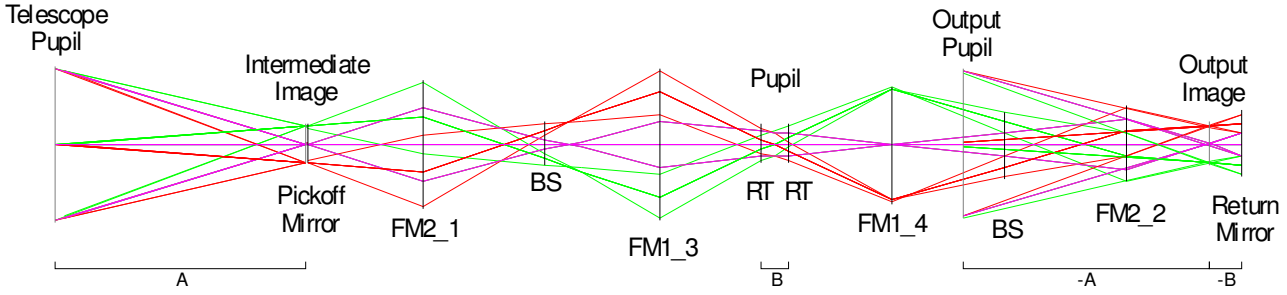

Fig. 2. Simplified optical schematic of FTS-2 for one port (not to scale). Beam diameters at the beamsplitters (BS) are kept as small as possible. The sizes and positions of the telescope pupil and image at the telescope elevation bearing are reproduced at the output of the FTS, taking into account the thickness of the system (B).

Since the JCMT optical and structural framework designs are already fixed, the FTS-2 optical and mechanical designs are highly interdependent and tightly constrained. In order to fit the optics in the available space, the interferometer design is folded vertically[7] as shown in Fig. 3.

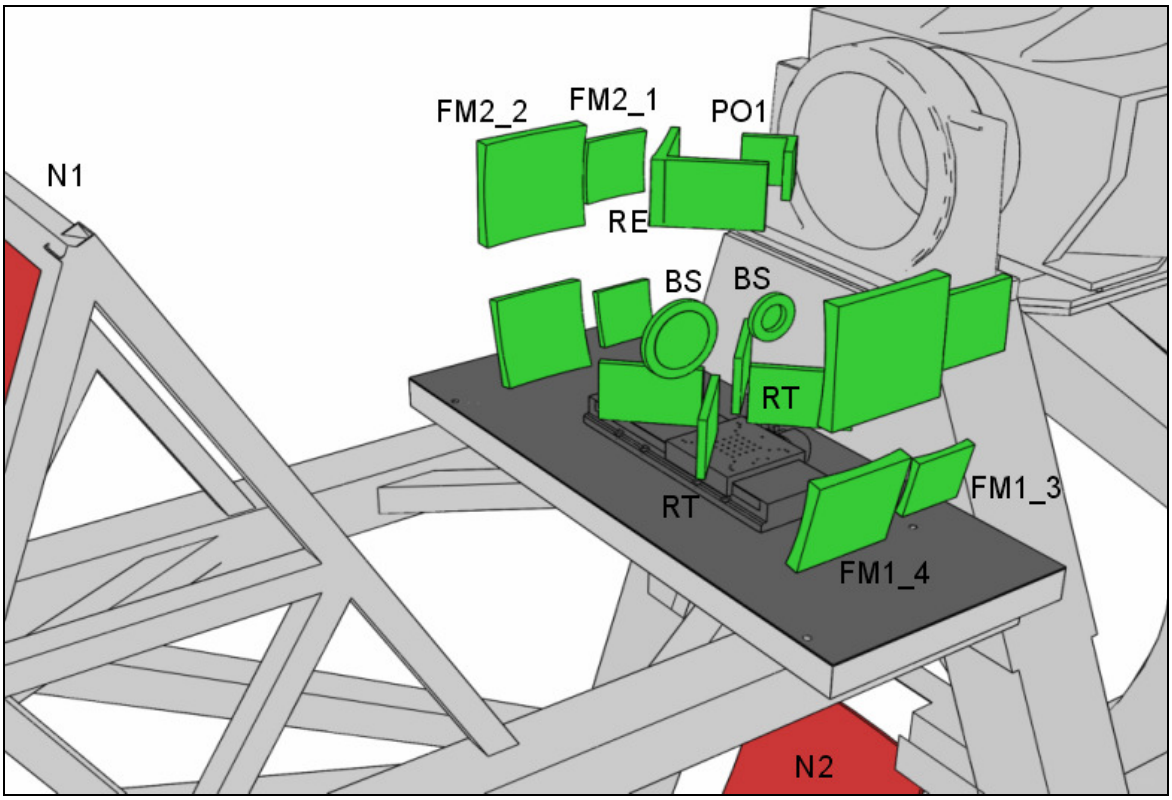

Fig. 3. Folded optical layout of FTS-2 at the mounting location on the SCUBA-2 N1 mirror support framework. The FTS-2 mechanical framework is hidden for clarity.

It is impossible with the existing SCUBA-2 feed optics to achieve the spectral resolution design goal over the entire SCUBA-2 field of view and optimizing the resulting tradeoff between FOV and spectral resolution within the constraints imposed by the fixed space envelope has proven to be a challenge.

Optimization of the optical design was done in Zemax taking into account the physical constraints of the available space envelope. With the constraints mentioned above and the limited mounting space, the maximum FOV is ultimately limited by the maximum practical mirror diameters (roughly 400 mm diameter) to approximately 5 arcmin^2.

3. MECHANICAL DESIGN

Mounting the 16 FTS-2 mirrors in a compact folded configuration without creating any mechanical or optical interference with the existing JCMT and SCUBA-2 systems was a major challenge in the mechanical design. Not all the optical components could be mounted directly to the optical breadboard, so a framework design was adopted to support the upper optics as well as allow the pickoff and return mirrors to be retracted from the SCUBA-2 beam when not in use. A Newport damped optical breadboard forms the base of the system and provides isolation from telescope vibration, as well as a flat mounting surface for all of the FTS-2 hardware. The breadboard will be supported by seven adjustable feet when mounted on the JCMT N1 support framework.

3.1 Mechanical framework

A tubular 6061-T6 aluminum framework will support all of the FTS-2 hardware which is not on the breadboard level, including the beamsplitters, upper fixed mirrors, pickoff and return mirrors, and the retraction assembly. The framework will be bolted to the optical breadboard and protective covers will be fitted to the outside to prevent damage and dust accumulation. The asymmetrical design of the framework avoids interference with the SCUBA-2 beam and the JCMT primary mirror backing structure while maintaining high rigidity. The framework sub-assemblies will be welded separately and then bolted together, in order to facilitate shipping of the instrument. Since the framework will measure roughly 2 m x 0.6 m x 1.3 m, it will be disassembled into several sections which can be packaged flat for shipping to the JCMT. The framework is shown in Fig. 4.

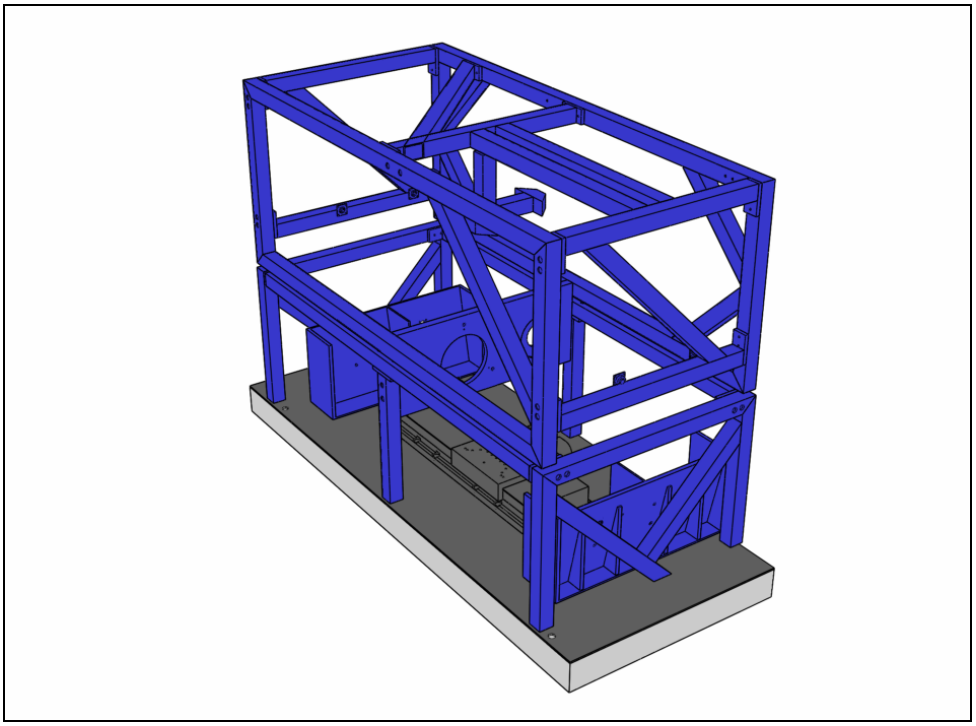

Fig. 4. FTS-2 mechanical framework mounted on the optical breadboard. Optics are hidden for clarity.

3.2 Mirror mounts

Maximizing the FTS-2 field of view requires mirrors with diameters up to 400mm within the interferometer. The mass for each of these mirrors is expected to be in the range of three to six kilograms. The mirror mounting features must be compact due to the proximity of the mirrors to each other, particularly the pickoff and return mirrors and the rooftop mirrors. As there are no suitable commercially available mirror mounts, the FTS-2 mirror mounts were custom designed.

The mirror mount design incorporates a spherical roller bearing for a pivot. A roller bearing was chosen over a plain spherical bearing for the reduced friction, which allows for smoother adjustment. The spherical bearing is fastened into a bracket plate, with the centre of the mirror hanging from a bolt passing through the bearing. If required, a third axis of adjustment (translation) can be obtained by inserting shims in between the bolt and the mirror. The bracket plate also houses the two adjusters necessary for the elevation and azimuth adjustment of the mirror, and a tensile spring which ensures the stiffness of the assembly and forces the mirror to return to its position following a shock.

To prevent the adjuster tips from scarring the aluminum mirror, two steel inserts are integrated into the mirror. The elevation insert has a V-groove to prevent rotation of the mirror about the axis of the spherical bearing. The elevation adjuster was chosen for this function as the moment induced by the mirror's weight acts on it and thus it will provide more stability. The machining of the bracket plate is minimal, making this design a very cost-effective solution. Fig. 5 depicts an assembled mirror mount featuring two Zaber Technologies[8] NA11-16B motorized adjusters and a compression spring assembly.

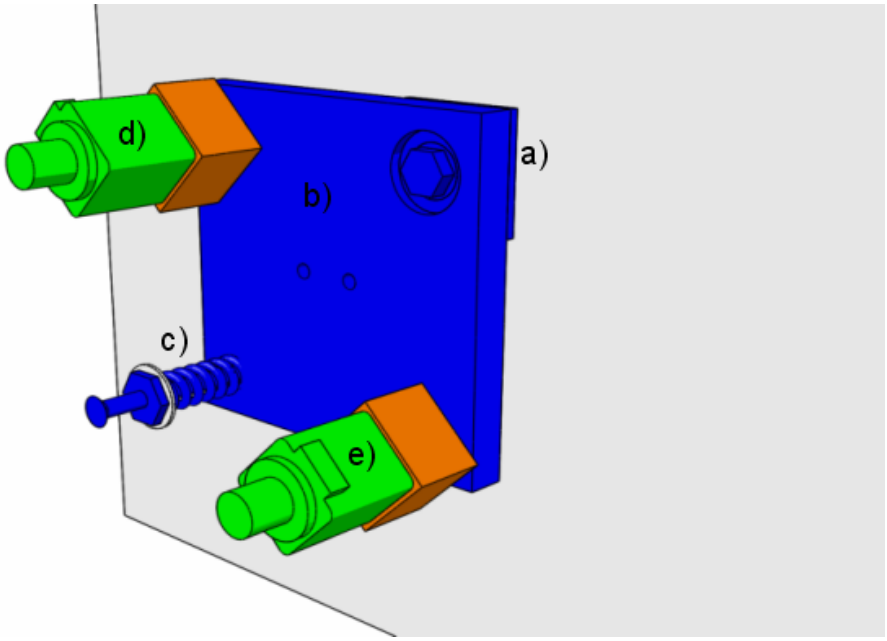

Fig. 5. Spherical bearing mirror mount, showing a) spherical bearing, b) bracket plate, c) tensioning spring, d) and e) motorized adjusters.

The spherical bearings allow an 8° range of adjustment in each axis. The static and dynamic loading are well below the ratings for the bearings, rendering the bearings maintenance free. Testing in the lab using a small telescope[9] has demonstrated the resolution to be on the order of 0.1 arc seconds per actuator microstep. The adjustment remains very smooth and predictable at the arc second level, and the mirror returns to its desired position when subjected to normal handling shock. This design could be easily adapted to other applications requiring large mirrors.

3.3 Linear translation stage

The FTS-2 rooftop mirrors are displaced by an Aerotech ALS5000 series linear motor translation stage[10] with 450 mm of travel. The brushless, non-contact linear servo motor features zero backlash and the stage metrology is based on a non-contact Heidenhain linear encoder. The stage has integral limit transducers to prevent driving the moving platform beyond the end of travel. Accelerations of 30 m/s^2 and velocities of 2 m/s can be achieved with a maximum permissible load of 135 kg, easily accommodating the motion profiles for the FTS-2 rooftop mirror masses.

3.4 Rooftop mirror assembly

The rooftop mirrors sit atop the Aerotech translation stage moving platform, which moves to provide varying optical path difference between the interferometer beams. Each rooftop mirror sub-assembly supports one mirror from each side of the interferometer. This allows one set of mirrors to be removed for alignment of the remaining interferometer mirrors and then reinstalled with very little disturbance to their alignment.

3.5 Retraction mechanism

It is necessary for the FTS-2 pickoff and return mirrors to be retracted from the SCUBA-2 beam when FTS-2 is not in operation. These mirrors also require remote actuators for periodic adjustment of the alignment to the SCUBA-2 beam. The pickoff mirror retraction assembly consists of a rail and carriage system, a ball screw, and a Zaber Technologies stepper motor. The ball screw and stepper motor combination will allow the mirrors to be positioned in the beam with a resolution of 0.1 µm. The rail will be bolted to the FTS-2 framework at a spacing of 60 mm to minimize deflection and produce superior repeatability. The Zaber motor will be driven in a step-back fashion to compensate for backlash such that it will always approach its destination from the same direction.

4. OBSERVING MODES

Atmospheric emission is the dominant source of radiant loading at submillimetre wavelengths. Moreover, variations in atmospheric emission are particularly problematic for an FTS where, upon Fourier transformation, they introduce spectral features into the resulting spectrum. By utilizing the second input port of the Mach-Zehnder FTS to view an adjacent background sky position, variations in atmospheric emission can, to first order, be cancelled by the subtractive properties of the FTS. Moreover, this cancellation results in a dramatic reduction in the dynamic range required in the resulting interferogram. Also, the dual output ports of the FTS provide complementary data which can further reject common mode noise present in the often hostile telescope environment, resulting in a factor of $\sqrt{2}$ increase in S/N. Proper selection of a background location is crucial to the success of this technique; the location of the second input port must be carefully considered in the observation planning.

Using dual input ports, the moving mirror may be scanned continuously (Rapid-Scan or RS) or stepped discretely (Step-and-Integrate or SI). With RS, the resulting interferograms will not be sampled uniformly in optical retardation since the SCUBA-2 data acquisition system is independent of the FTS-2 scanning mechanism. This will necessitate the use of a non-uniform FFT or an interpolation process in the processing pipeline. Algorithms to cope with this problem have already been developed for the SPIRE spectrometer[11] by members of our group.

We are also investigating the potential use of the step-and-integrate operating mode to improve observational efficiency and atmospheric noise rejection. In this mode, the optical path difference in the interferometer is incremented in discrete steps and data is read out only when the mirrors are stationary, thereby ensuring that the interferogram is sampled on a uniform position grid. This mode could in principle be used with the single-port mode in conjunction with the SCUBA-2 DREAM mode[12], however, the baseline plan is to use the Rapid Scan dual-port atmospheric cancellation technique.

4.1 Undersampling

Since the SCUBA-2 filters will have extremely high out-of-band rejection, the interferograms may be sampled sparsely and the resulting aliasing of the spectra can be easily removed. This will allow high resolution spectra to be obtained in shorter scan times, which will reduce the effects of sky rotation and atmospheric noise. By proper selection of the optical path sampling interval, both the 450 and 850 µm bands can be aliased simultaneously without any loss of information within the bands.

Normal Nyquist sampling requires that the interferograms be sampled every 0.02 cm of OPD, but this interval can be increased to 0.1 cm through the use of undersampling, which translates to a factor of 5 increase in acquisition speed. We have tested this technique with the U of L FTS[13] using both the normal rapid-scan and the step-and-integrate modes[7].

4.2 Resolution

The FTS-2 instrument has a continuously variable resolution ranging from $\Delta\nu \sim 0.5$ to 0.006 cm^{-1}. (The translation stage will allow slightly better resolution if some vignetting of the outer pixels can be tolerated.) While the FTS-2 resolution can be adjusted arbitrarily over the full range, the baseline plan is to provide only two resolution modes. The maximum resolution will be used for spectral line studies, while a lower resolution of ~0.1 cm^{-1} will be used for Spectral Energy

Distribution (SED) measurements[7]. With the fixed detector frame rate, higher resolution comes at the expense of longer acquisition times.

4.3 Baseline Observing Modes

FTS-2 observations can be classified as either SED measurements or spectral line studies. SED measurements only require a few spectral bins across a filter bandpass in order to characterize the continuum curvature, and can be accomplished with low resolution (~0.1 cm^{-1}) scans. On the other hand, spectral line studies require the maximum possible resolution. By grouping all observations into these two resolution categories, the processing and observation planning can be simplified.

In the low-resolution SED mode, scans can be double-sided without seriously affecting observing efficiency. With fully double-sided scans, the phase correction processing step is simplified greatly. The baseline plan is to implement the SED mode using the dual-port configuration to provide atmospheric correction. The nominal operating mode will be RS; the aliased SI mode combined with DREAM will be investigated during commissioning.

In the high-resolution spectral line mode, scans must be single sided to maximize the use of the linear stage travel and minimize the scan acquisition time. A short double-sided scan will provide phase information for the phase correction algorithm. The dual-port configuration will be used to provide atmospheric correction.

For dual-band operation, the acquisition time is limited by the 25 cm^{-1} Nyquist frequency for the 450 μm band. If only the 850 μm band is needed, then the acquisition time (and cube size) is reduced due to the lower 15 cm^{-1} Nyquist frequency. A summary of the acquisition times and interferogram lengths is given in Table 1.

Table 1. Scan parameters for the SED and Spectral Line modes.

	SED		Spectral Line	
	Dual Band	850 μm	Dual Band	850 μm
Resolution	~0.1 cm^{-1}		~0.006 cm^{-1}	
Scan type	Double-sided		Single-sided	
Phase correction	Simple		Full	
Scan mode	RS (SI)		RS	
Total Travel (cm OPD)	6+6		100+6	
Velocity (cm/s OPD)	4	6.6	4	6.6
Scan time (s)	3	1.8	26.5	15.9
Frames	605	363	5300	3180

4.4 Mapping

Mapping with FTS-2 will be complicated by vignetting effects and calibration issues with off-axis pixels. While correction of these effects should be possible after commissioning tests, mapping of extended regions will require post-processing of the spectral data by the observer.

5. SOFTWARE

As an ancillary instrument, FTS-2 must be delivered with control and data reduction software which interfaces with the existing SCUBA-2 and JCMT systems. Data reduction code based on the SPIRE system[11] has been developed for FTS-2, and custom control software has been written to control the translation stage and actuators.

5.1 Data reduction pipeline

Data reduction for SCUBA-2 and its ancillary instruments FTS-2 and POL-2 will be automated by the use of a data reduction pipeline. The main SCUBA-2 pipeline[14] is written in object-oriented Perl. The pipeline parses ‘recipes’ and calls appropriate ‘primitive’ functions in various algorithm ‘engines’. Since the implementation of the algorithm engines is independent of the pipeline itself, the FTS-2 algorithm engine can be written in Java to exploit existing SPIRE code.

The Java FTS-2 data reduction algorithm engine consists of two major parts: an interface layer and a core layer. The interface layer provides a message interface for the SCUBA-2 data reduction pipeline to invoke the functions of the core layer. Both DRAMA[15] and SOAP messaging interfaces are supported. The core layer is made up of five independent modules: I/O, Interpolation, Phase Correction, FFT, and the Quick Look (QL) display system.

The FTS-2 algorithm engine uses a multi-tier structure (see Fig. 6) consisting of three separate modules (referred to as 'actions' for DRAMA, or 'operations' for SOAP):

- set_parameters - set the data reduction parameters
- data_reduction - perform the core numerical computation of FTS-2 data reduction
- exit - stop FTS-2 Engine and exit

From the perspective of the Pipeline, each action or operation has a corresponding primitive.

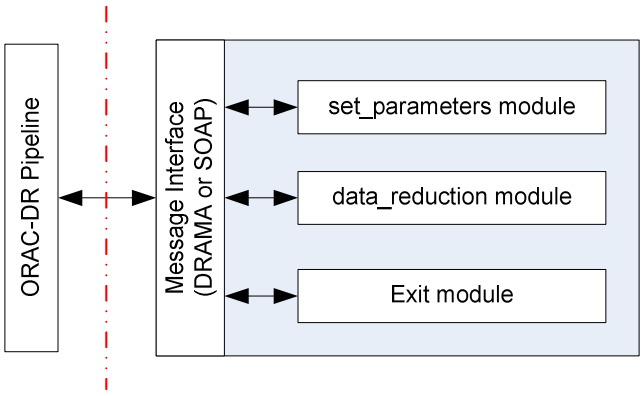

Fig. 6. FTS-2 algorithm engine messaging overview.

The SCUBA-2 DR pipeline calls the appropriate algorithm engine for the current instrument when the pipeline detects a new data file either from the Data Acquisition System (on-line mode) or from the data archive (off-line mode). After the algorithm engine completes the relevant tasks or exits, the SCUBA-2 data reduction pipeline regains control of the data flow. Fig. 7 shows a schematic of the FTS-2 data reduction module, which reduces raw interferogram data from the SCUBA-2 pipeline into spectral data files as well as reduced data for the SCUBA-2 Quick Look display system.

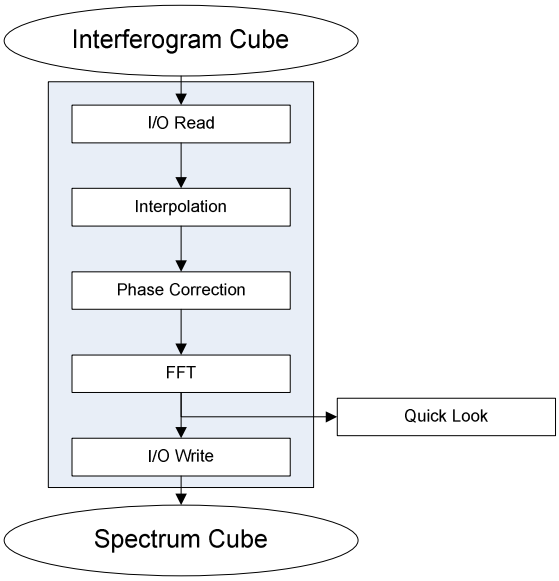

Fig. 7. FTS-2 data reduction engine modules.

In order to separate the core numeric processing from both the data access layer and the message processing layer, the FTS-2 data reduction module is implemented as a Java class: ca.uol.aig.fts.drpipeline.DRPipeline. This class integrates I/O, Interpolation, Phase Correction, FFT and Quick Look into a pipeline to fully process FTS-2 interferogram data.

The FTS-2 engine I/O function of is implemented by Java class ca.uol.aig.fts.io.NDFIO, the interpolation function is implemented in the Java class ca.uol.aig.fts.fitting.CubicSpline, the phase correction function is implemented in the Java class ca.uol.aig.fts.phasecorrection.PhaseCorrection, and FFT processing is implemented in the classes RealDoubleFFT, RealDoubleFFT_Even, and RealDoubleFFT_Odd of the Java package ca.uol.aig.fftpack.

The FTS-2 engine uses four external Java libraries: a Java version of FFTPack[17], Jama[18], StarJava[19], and a Java version of DRAMA. The Java version of FFTPack has been translated from the original FORTRAN code by the FTS-2 group. FFTPack is a well-known package of FORTRAN subprograms for the fast Fourier transform of periodic and other symmetric sequences, including complex, real, sine, cosine, and quarter-wave transforms. JAMA is a basic linear algebra package for Java developed by NIST. Two other required Java libraries are StarJava and DJAVA (Java version of DRAMA).

5.2 Control systems

Coordination and synchronization of the JCMT instruments, Observatory Control System[20] (OCS) and Data Acquisition System are performed by the JCMT Real Time Sequencer[21] (RTS). The FTS-2 RTS client will receive commands from the OCS and synchronizes their execution with the RTS master clock. In this way, the motion of the FTS mechanisms can be controlled by the automated OCS and the interferometer optical path difference can be read out synchronously with the 200 Hz SCUBA-2 frames. The JCMT uses a generalized software interface for all RTS compliant instruments, which significantly simplifies the control software development for the FTS-2 system. The FTS-2 RTS client software will use the RTAI[22] real-time Linux operating system.

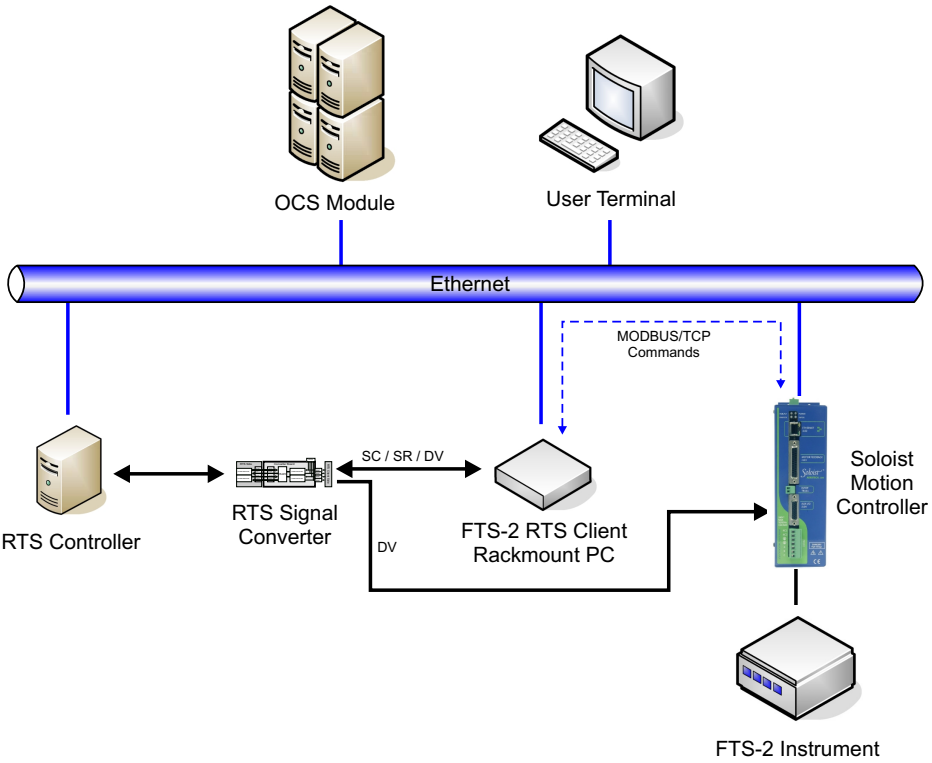

Fig. 8. Schematic of the FTS-2 control system interfaces with the JCMT OCS and RTS systems.

5.3 Data rate

Data rates for the FTS-2 instrument will not exceed those for normal SCUBA-2 observations. In the RS mode, frames will be stored at 200 Hz before being reduced by the pipeline. Depending on the spectral range in the stored spectral cubes, the maximum reduced data volume before averaging will range from 0.25 to 0.5 times the raw data volume.

5.4 Processing speed

The FTS-2 engine was benchmarked on a Linux Fedora platform with a 2.8Ghz P4 CPU and 1 GB RAM. The benchmarks do not include any time that the ORAC-DR pipeline would take to call the algorithm engine. The phase correction function (PCF) decays very quickly at frequencies far from DC. Larger PCF lengths produce more accurate results, but require more computation time. Usually, in order to reduce the calculation time, the PCF is kept as short as possible. In the case of FTS-2, the PCF size never needs to be larger than 160 points. Benchmark results for the worst-case scenario (160 point PCF) are given in Table 2, showing that real-time processing should be possible in all observing modes.

Table 2. Processing benchmarks

Scan Mode	Interferogram Length (points)			Benchmarks (s)				Total Time (s)	
	Short Wing	Long Wing	Total	I/O(R/W)	Interpolation	Phase Correction	FFT	Acquisition	Processing
SED 850 Band	180	180	360	0.19/0.11	0.17	0.88	0.045	1.80	1.40
SED Dual Band	300	300	600	0.21/0.15	0.28	1.26	0.057	3.00	1.96
Spectral Line 850 Band	180	3000	3180	0.27/1.04	0.85	6.48	0.406	15.90	9.05
Spectral Line Dual Band	300	5000	5300	0.36/1.75	1.39	10.54	0.670	26.50	14.71

6. CONCLUSION

The FTS-2 project completed the PDR stage in July 2005 and the CDR is scheduled for June 2006. Delivery of the instrument to the JCMT will occur in mid 2007, and commissioning will occur after the SCUBA-2 commissioning phase is complete.

7. ACKNOWLEDGEMENTS

On behalf of the Canadian SCUBA-2 consortium, the authors acknowledge the support of a CFI international access award for Canadian participation in the SCUBA-2 project. Thanks also go to Side by Side Optical Engineering (http://www.sidebysideoptics.com/) for their effort in the optical design.

REFERENCES

1. P. Andre, D. Ward-Thompson and M. Barsony, "From Prestellar Cores to Protostars: the Initial Conditions of Star Formation," *Protostars and Planets IV*, U. Arizona Press, 59 (2000).
2. F. Shu, Z. Li and A. Allen, "Does Magnetic Levitation or Suspension Define the Masses of Forming Stars?", *Ap. J.* 601, 930-951 (2004).
3. W. S. Holland, E. I. Robson, W. K. Gear, C. R. Cunningham, J. F. Lightfoot, T. Jenness, R. J. Ivison, J. A. Stevens, P. A. R. Ade, M. J. Griffin, W. D. Duncan, J. A. Murphy and D. A. Naylor, "SCUBA: a common-user submillimetre camera operating on the James Clerk Maxwell Telescope," *Mon. Not. R. Astron. Soc.* 303, 659-672 (1999).
4. W. S. Holland, W. D. Duncan, B. D. Kelley, K. D. Irwin, A. J. Walton, P. A. R. Ade and E. I. Robson, "SCUBA-2: A large format submillimetre camera on the James Clerk Maxwell Telescope," *Proc. SPIE, Millimeter and Submillimeter Detectors for Astronomy* 4855, 1-18 (2003).
5. D. A. Naylor and B. G. Gom, "SCUBA-2 imaging Fourier transform spectrometer," *Proc. SPIE, Imaging Spectrometry IX* 5159, 91-101 (2004).
6. P. A. R. Ade, P. A. Hamilton and D. A. Naylor, "An Absolute Dual Beam Emission Spectrometer," *Optical Society of America, FTS topical meeting* poster FWE3, Santa Barbara, California, (1999).
7. B. G. Gom and D. A. Naylor, "An update on the imaging Fourier transform spectrometer for SCUBA-2," *Proc. SPIE, Astronomical Telescopes and Instrumentation* 5498 (2004).
8. Zaber Technologies Inc., http://ww.zaber.com/
9. D. A. Naylor and A. A. Schultz, "A Simple Technique for Accurately Measuring the Dihedral Angle of a Roof-Top Morror" *Optics and Photonics News* 11, issue 11, (2000).
10. Aertotech Inc., http://www.aerotech.com/
11. D. A. Naylor, T. R. Fulton, P. W. Davis, I. M. Chapman, B. G. Gom, L. D. Spencer, J. V. Lindner, N. E. Nelson-Fitzpatrick, M. K. Tahic and G. R. Davis, "Data processing pipeline for a time-sampled imaging Fourier transform spectrometer," *Proc. SPIE, Imaging Spectrometry X* 5546, (2004).
12. R. S. Le Poole and H. W. van Someren Greve, "DREAM, the Dutch REal-time Acquisition Mode for SCUBA", http://www.strw.leidenuniv.nl/~lepoole/ (1998).
13. D. A. Naylor, B. G. Gom, I. S. Schofield, G. J. Tompkins and G. R. Davis, "Mach-Zehnder Fourier transform spectrometer for astronomical spectroscopy at submillimeter wavelengths," *Proc. SPIE, Millimeter and Submillimeter Detectors for Astronomy* 4855, 540-551 (2003).
14. T. Jenness, F. Economou, D. Scott, D. Kelly and W. S. Holland, "Preliminary Design of the SCUBA-2 Data Reduction Pipeline," *ADASS XIII*, (2004).
15. T. J. Farrell, K. Shortridge and J. A. Bailey, "DRAMA: An Environment for Instrumentation Software," *Bulletin of the AAS*, 25(2), (1993).
16. A. G. Gibb, D. Scott, T. Jenness, F. Economou, B. D. Kelly and W. S. Holland, "Design of the SCUBA-2 Quick Look Display and Data Reduction Pipeline," *ASP, Astronomical Data Analysis Software and Systems XIV*, 347, 585 (2005).
17. Paul N. Swarztrauber, http://www.netlib.org/fftpack/
18. J. Hicklin, C. Moler, P. Webb, R. Boisvert et al., http://math.nist.gov/javanumerics/jama/
19. Star Java, http://www.starlink.ac.uk/java/java.htm
20. N. P. Rees, F. Economou, T. Jenness, R. D. Kackley, C. A. Walther, W. R. Dent, M. Folger, X. Gao, D. Kelly, J. F. Lightfoot, I. Pain, G. Hovey and R. O. Redman, "JCMT observatory control system," *Proc. SPIE, Advanced Telescope and Instrumentation Control Software II* 4848, (2002).
21. B. D. Kelly, http://www.roe.ac.uk/ukatc/projects/scubatwo/documents/software/sc2-sof-s200-026.pdf
22. http://www.rtai.org/

Appendix D

Suggested readings on Fourier transform spectroscopy

Introductory Textbooks:

Eugene Hecht. Optics. Addison Wesley, fourth edition, (2002).

P. R. Griffths and J. A. Haseth. Fourier Transform Infrared Spectrometry. John Wiley and Sons, New York, (1986).

J. F. James, A students guide to Fourier transforms, Cambridge University Press (2002).

Advanced Textbooks:

R. J. Bell. Infrared Fourier Transform Spectroscopy. Academic Press, New York, (1972).

Sumner P. Davis, Mark C. Abrams, and James W. Brault. Fourier Transform Spectroscopy. Academic Press, first edition, (2001).

J. E. Chamberlain. The Principles of Interferometric Spectroscopy. John Wiley and Sons: Chichester, England (1979). Edited by G. W. Chantry and N. W. B. Stone.

E. O. Brigham. The Fast Fourier Transform. Prentice-Hall Inc., (1974).

M. Born and E. Wolf. Principles of Optics, Cambridge University Press, (1980).

L. Mertz. Transformations in optics. New York: Wiley, (1965).

D. C. Champeney. Fourier Transforms and their Physical Applications. Academic Press: St. Louis, MO (1973).

R. M. Bracewell. Fourier Transforms and Its Applications. McGraw-Hill Book Co: New York, NY (1965).

Historical Papers:

Albert A. Michelson. On the application of interference methods to spectroscopic measurements. Philosophical Magazine, 34:280, (1892).

H. Rubens and R. W. Wood. Focal isolation of long heat-waves. Philosophical Magazine, 21:249–261, (1911).

H. Nyquist. Certain topics in telegraph transmission theory. Transactions of the American Institute of Electrical Engineers, 47:617 – 644, (1928).

P. Fellgett. A propos de la theorie du spectrometre interferentiel multiplex. Journal of Physics Radium, 19:187, (1958).

P. Jacquinot. New developements in interference spectroscopy. Rep. Prog. Phys., 23:267–312, (1960).

J Connes, Recherches sur la spectroscopie par transformation de Fourier, PhD Thesis Laboraotry Aime Cotton, Bellevue, France, (1960).

J. W. Cooley and J. W. Tukey. An algorithm for the machine calculation of complex fourier series. Math. Comput., 19:297, (1965).

Michael L. Forman. Fast Fourier-Transform Technique and it's Application to Fourier Spectroscopy. Journal of the Optical Society of America, 56(7):978, (1966).

M. L. Forman, W. Steel, and G. A. Vanasse. "Correction of Asymmetric Interferograms Obtained in Fourier Spectroscopy." Journal of the Optical Society of America, 56(1):59–64 (1966).

L. Mertz. Rapid scanning fourier transform spectroscopy. J. Phys. Coll. C2, Suppl. 3-4, 28:88, (1967).

R. H. Norton and R. Beer. New apodizing functions for fourier spectrometry. Journal of the Optical Society of America, 66:259 – 264, (1976).

F. J. Harris. On the use of windows for harmonic analysis with the discrete fourier transform. In Proceedings of the IEEE, volume 66, pages 51–83, (1978).